UNIVERSITY OF CALIFORNIA
Santa Barbara

Investigations with Optical Tweezers: Construction, Identification, and Control

A Dissertation submitted in partial satisfaction of the
requirements for the degree Doctor of Philosophy
in Mechanical Engineering

by

Aruna Ranaweera

Committee in Charge:

Professor Bassam Bamieh, Chair
Professor Bradley E. Paden
Professor Carl D. Meinhart
Professor Kimberly L. Turner
Doctor Ratneshwar Lal

September 2004

The dissertation of Aruna Ranaweera is approved.

Bradley E. Paden

Carl D. Meinhart

Kimberly L. Turner

Ratneshwar Lal

Bassam Bamieh, Committee Chair

September 2004

Investigations with Optical Tweezers

Acknowledgements

I dedicate this dissertation to the memory of my late advisor, Professor Mohammed Dahleh, whose intelligence, charisma, and vision convinced me to pursue a doctorate at UCSB. I am grateful to him for entrusting me with this and other projects and for being an inspirational advisor and teacher. Although many people know Mohammed for his impressive academic and professional achievements, I will remember him best as an intelligent and witty conversationalist; he was full of funny (often hilarious) stories and anecdotes. I miss him very much.

I am grateful to Professor Bassam Bamieh for providing financial support (after Mohammed's untimely death), which enabled me to continue my doctoral work and attend several national conferences. I also thank Bassam for encouraging me to study RLS identification and LQG control and for providing freedom to explore my academic interests.

I thank the members of my PhD Committee–Professor Brad Paden, Professor Carl Meinhart, Professor Kim Turner, and Doctor Ratnesh Lal–for their time, encouragement and advice. I have used their laboratory equipment and consulted with them, their students, and post-docs. In particular, I thank Carl for purchasing supplies for my project and for providing access to micro-fluidic parts; I thank Ratnesh for providing both information pertaining to biology and various supplies from his Neuroscience Research group in the Department of Biology; I thank Brad for providing access to his laboratory space and equipment; and I thank Kim for providing access to the equipment and supplies in her MEMS laboratory.

I am grateful to Professor Karl Åström for showing great enthusiasm and interest about my work and progress; I thank him for introducing me to many areas of control engineering, in particular, stochastic control theory. The mean passage time results in this dissertation are a direct result of the class project I completed for his graduate stochastic control course. Karl is a truly inspirational scholar, teacher and person. I thank him for being a great role model for me; I have benefited immensely from his positive influence.

I thank Professor Andrew Teel for sharing his expertise on nonlinear control design. The nonlinear controllers developed in this dissertation are a direct result of the class project I completed for his graduate nonlinear control design course. I thank Andy for being approachable and for helping me in a very thorough and efficient manner.

I would also like to acknowledge other faculty members at UCSB who taught courses that were relevant to my PhD research: Professor Petar Kokotovic (system identification), Professor Ian Rhodes (Kalman filtering), Professor Roy Smith (robust control), Professor Thomas Mitchell (advanced dynamics), and Professor Andrew Cleland (optics). I also thank Professor Carlos Levi and Professor Bob McMeeking for being very supportive of my academic and professional goals. I am grateful to Professors Mustafa Khammash and Kim Turner for including me in their summer workshop on system identification.

I thank Professor Steve Quake and Doctor Chris Meiners from Caltech for giving Patricia Swift and me a detailed tour of their optical tweezer system. I also thank Professor Steven Gross from UC Irvine for providing useful tips for aligning the laser beam used for trapping. I am grateful to Professor Jim Spudich at Stanford for granting permission to re-print one of his

figures in my dissertation.

I thank Patricia Swift for tirelessly working on this project while we were both completing our masters degrees. She provided an invaluable archive of published papers and also designed the first photodetector circuit. I also thank Deborah Detch for selecting and purchasing beads for trapping. I am grateful to Doctor Derek Trethaway for providing assistance assembling the imaging system.

I also thank the Engineering Technical Staff in the Mechanical Engineering department at UCSB: Dave Bothman, Verne Parmenter, Kirk Fields, and Jeff Kirby. They not only provided me with practical advice, but also shared their equipment and facilities; often, they were the first people I consulted regarding technical issues. I also thank the computer support staff–Simon Ibsen, Doug Siggins, and Tam Pham–for keeping all four of my PC's running and for maintaining a secure and efficient network. I am also grateful to the staff in the machine shop–Nelson Bednersh, Andrew Weinberg, and Rodney Orr–for providing assistance and equipment whenever I needed to make or modify mechanical parts. I thank Doctor Rajinder Bhatia and Doctor Arjan Quist for providing biological supplies such as PBS and I thank Rajashree Bhaskaran for introducing me to *LabVIEW*.

I also thank my friends in the graduate control research group at UCSB. In particular, I thank my office partners–Mihailo Jovanovic, Symeon Grivopoulos and Matthias Schibli–for their good nature and friendship. I also thank Mihailo for helping me with many technical issues and also for impressing me (and many others) with his unbeatable work-ethic. I am grateful to Symeon for bringing a relaxed attitude to our laboratory and to Matthias for expanding my beach volleyball skills. I thank Maria Napoli for being super-nice and for helping with theoretical concepts, Andrew Daniele for sharing laboratory expertise, Paul Cronin for his hospitality and for keeping me up-to-date on practical trends, Niklas Karlsson for helping with *MATLAB* code, Vasu Salapaka for his encouragement, Makan Fardad for helping with digital documentation, and Anthony DiCarlo for motivating me to start writing my dissertation. I also thank Sophie, Barkus, Mike, Umesh, Lasse, Ove, Neb, Zoran, Hana, Neda, Dragan, Gwen, George, Thomas, Tom, Yang Lu, JC, Margherita, Laura, Annie, Marion, Aaron, Craig, Doca, Jaime, Dom, Erkut and others for their friendship and assistance. I have enjoyed the company of many good people at UCSB, but there are too many to name here.

I thank my many students at UCSB for appreciating and encouraging my efforts as a TA; I enjoyed teaching them very much. I am humbled that the graduating seniors in the classes of 2000 and 2002 considered me worthy of a teaching assistant award. I also thank Matt Sanford and Mark Farrelly's ASME student chapter in 1998-99 for helping me adjust to life at UCSB.

I also thank the staff in the ME Office–Chris Gregory, Lauren Gleason, Linda James, Janet Fisher, Christi Lung, Grant Brakesman, Julie Dunson, Karen Cisneros, June Finney, Josie Castagnola, Liana Decierdo, Janelle Papa, Nola Niklin, and others–for helping me with all of my administrative needs in a cheerful and friendly manner. I am grateful to the staff in the ECE Budget Office–Lynnette McCoy, Alex Locke, and Josie Castagnola–for purchasing and budgeting most of the equipment for this project.

I thank Professor Fred Leckie for recruiting me to UCSB and for being a great friend for me and my family. Fred's positive influence convinced me to attend UCSB for graduate school; he is one of the nicest and most perceptive people I know. I will miss spending time with him and his wonderful family; In particular, I will miss watching international rugby matches on TV with him and Sean.

I thank my many local friends for making me feel welcome during my stay in Santa Barbara and Goleta. In particular, I thank the afternoon volleyball regulars at East Beach, the Santa Barbara Grunions and UCSB rugby teams, and my friends from the UCSB Recreation Center. I am grateful to Cara O'Callaghan and Mike Hagler for their friendship and hospitality; I will miss our lunch meetings at the UCen pasta place. I also thank Mary Johnson and the PT staff for keeping me healthy.

I thank my aunt Lakshmie and uncle Ranmuthu in Ventura for providing me with a home-away-from-home. They always made me feel welcome with their delicious Sri Lankan food and merry company. Their unconditional support and encouragement is much appreciated.

Last but not least, I thank my family in Sri Lanka and New York for their encouragement and support. In particular, I thank my parents for purchasing my Toshiba laptop which dramatically increased my work efficiency; they have always strongly supported my academic efforts. I am grateful to my father (known as 'Muni' in Santa Barbara) for introducing me to UCSB while he was here on a research appointment with Fred Leckie. As always, I thank my brother Isuru and sister Dilanthi for providing encouragement and much-needed comic relief.

CURRICULUM VITAE OF ARUNA RANAWEERA

September 10, 2004

Education

Ph.D. in Mechanical Engineering, University of California, Santa Barbara, September 2004.

M.S. in Mechanical Engineering, University of California, Santa Barbara, June 2000.

B.S.E. in Mechanical and Aerospace Engineering (Honors), Princeton University, June 1998.

Fields of Study

Dynamic Systems, Control, and Robotics

Mechatronics, System Identification, Stochastic Control, Nonlinear Control

Management Practice

Professional Awards and Honors

Best Presentation Award, *Information Storage and MEMS* Session, American Control Conference, Boston, MA, June 2004.

Best Presentation Award, *Micro/Nanosystems* Session, American Control Conference, Denver, CO, June 2003.

Outstanding Teaching Assistant Award, Department of Mechanical and Environmental Engineering, UCSB, 2002.

Outstanding Teaching Assistant Award, Department of Mechanical and Environmental Engineering, UCSB, 2000.

Dean's Fellowship, College of Engineering, UCSB, 1999 and 2000.

Departmental Honors, Department of Mechanical and Aerospace Engineering, Princeton University, 1998.

Professional Employment

Graduate Researcher, UCSB, Department of Mechanical and Environmental Engineering.

- Optical Tweezers, *Construction, Identification, and Control*, 2000-2004.
- Atomic Force Microscopy, *Construction and Calibration*, 1999.

Laboratory Developer, UCSB, Department of Mechanical and Environmental Engineering.

- ME 6 *Basic Electrical and Electronic Circuits*, Winter 2003.
- ME 104 *Sensors, Actuators, and Computer Interfacing*, Fall 2001, Fall 2002.
- ME 106A *Advanced Dynamics and Control Laboratory*, Spring 2003.

Teaching Assistant, UCSB, Department of Mechanical and Environmental Engineering.

- ME 17 *Mathematics in Engineering*, Spring 2001.
- ME 125AI *Digital Control*, Winter 2002.
- ME 153 *Design of Engineering Systems*, Winter 1999, Winter 2001.
- ME 163A *Engineering Mechanics: Dynamics*, Fall 1998, Fall 2000.
- ME 163B *Engineering Mechanics: Vibrations*, Winter 2000.
- ME 186 *Manufacturing and Materials*, Spring 1999.

Experimentalist, UCSB, Materials Department.

- Ceramic Composites, *Characterization*, Summer 1997.

Publications

1. A. Ranaweera and B. Bamieh, "Calibration of the Characteristic Frequency of an Optical Tweezer using an Adaptive Normalized Gradient Approach" in *Proceedings of the 2003 American Control Conference*, (Denver, CO), pp. 3738-3743, IEEE, June 2003.
2. A. Ranaweera, A. R. Teel, and B. Bamieh, "Nonlinear Stabilization of a Spherical Particle Trapped in an Optical Tweezer" in *Proceedings of the 42nd IEEE Conference on Decision and Control*, (Maui, HI), pp. 3431-3436, December 2003.
3. A. Ranaweera and B. Bamieh, "Calibration of the Characteristic Frequency of an Optical Tweezer using a Recursive Least Squares Approach" in *Proceedings of the 2004 American Control Conference*, (Boston, MA), pp. 1836-1841, American Automatic Control Council, June 2004.
4. A. Ranaweera, "Investigations with Optical Tweezers: Construction, Identification, and Control", PhD Dissertation, Department of Mechanical and Environmental Engineering, University of California, Santa Barbara, CA, September 2004.
5. A. Ranaweera, K. J. Astrom, and B. Bamieh, "Lateral Mean Exit Time of a Spherical Particle Trapped in an Optical Tweezer" to appear in *Proceedings of the 43rd IEEE Conference on Decision and Control*, (Paradise Island, Bahamas), December 2004.
6. A. Ranaweera, B. Bamieh, and V. Parmenter, "Sensors, Actuators, and Computer Interfacing Laboratory Course at the University of California at Santa Barbara" submitted to *Mechatronics Journal*, 2004.
7. A. Ranaweera and B. Bamieh, "Identification and Control of Optical Tweezers" to be submitted to *International Journal of Robust and Nonlinear Control*, 2004. (Tentative title).
8. A. Ranaweera and B. Bamieh, "On the Use of Mean Passage Times to Calibrate Stiffness and Drag in Optical Tweezer Experiments" to be submitted to *Applied Optics*, 2004. (Tentative title).

Abstract

"Investigations with Optical Tweezers: Construction, Identification, and Control"
by Aruna Ranaweera

In this dissertation, I provide an introduction to optical tweezers, including information about dynamics, construction, identification, and control. The main purpose is to analyze the properties of an optical tweezer from a control engineering point of view. The optical tweezer is widely used by biophysicists to study the mechanical properties of individual biological molecules.

Inertial and noninertial equations of motion are developed for both a linear trapping force and a cubic trapping force. By representing the noninertial dynamics of a trapped particle as a stochastic differential equation, probability distributions are discussed and first mean exit times are computed numerically. Experimentally measured mean passage times for a 9.6-micron diameter polystyrene bead within the linear trapping region show close agreement with theoretical calculations.

A recursive least squares method is applied to a trapped 9.6-micron diameter bead to study the possibility of obtaining faster calibrations of characteristic frequency. In spite of the asymmetry in the lateral optical trapping force, experimental calibration results for a sufficiently large square wave input are consistent with the average of off-line calibration results, within 7%. However, slight misalignments in the position detection system can significantly degrade the convergence rate and consistency of the on-line parameter estimates.

I also discuss and compare the application of PI control, LQG control, and nonlinear control to reduce fluctuations in particle position due to thermal noise. Assuming a cubic trapping force, I use computer simulations to demonstrate that the nonlinear controller can reduce position variance by a factor of 65 for a 1-micron diameter polystyrene bead under typical trapping conditions.

Guidelines for constructing and enhancing a research-grade optical tweezer system are also included.

Contents

List of Symbols

Symbols[1]

a Output coefficients

b Input coefficients

A Amplitude

d Diameter, disturbance

c_0 Speed of light in vacuum

C Capacitance

C_r Crest factor

$\mathcal{D}_{\mathcal{M}}$ Domain of model set

e Tracking error, white noise (unit variance)

E Expected value

$\overline{E}$ Expected value (asymptotic ensemble average)

f Focal length, Frequency (Hz)

F Force, Maximum frequency

g Gravitational acceleration, probability density function

G Transfer function

h Sampling time

h_b Height of bead center from wall surface

H Transfer function

I Light Intensity

J Instantaneous cost function

k Time index (integer), gain

k_B Boltzmann's constant

K AOD drive command, Memory time constant

l Scalar norm

L Lens

$\mathcal{L}$ Laplace transform operator

m Mass

m_1 First mean exit time

M Magnification, Period of PRBS, Normalizing signal

n Index of refraction, Number of bits, Measurement noise

N Number of data

$\mathcal{N}$ Normal distribution

N_A Numerical aperture

p Momentum, Probability, Scalar gain

P Power, Plant

q Forward shift operator

Q Trap Efficiency Factor

r Position in the radial direction, Radius, Reference input

R Range of influence of trap (trapping radius), covariance function, Resistance

s Laplace transform index

S Power spectrum

t Time (CT), Normalized time (DT)

T Absolute temperature, Time random variable, First passage time random variable

T_1 First exit time random variable

[1] Many symbols from Chapters 8, 9, and 10 are not included.

u Control input

v Velocity

V Criterion function

x Position on x-axis

X Frequency domain representation of $x(t)$, x-position random variable

w Wiener process

w_T Trap waist (spot size)

W Linear filter

y Position on y-axis, Measured output (position)

z Position on z-axis

Z Input and output data set

α Trap stiffness (spring constant)

β Drag coefficient, weighting function

δ Resolution, Dirac delta function

Δ Change

ϵ Output prediction error (innovation)

ϕ Spectral density, regression vector

Γ Matrix Gain

κ Scalar design parameter

λ Laser wavelength, forgetting factor

η Diffraction Efficiency, Viscosity

θ Angular Position, parameter vector

θ_B Bragg angle

θ_{scan} Maximum scan angle of AOD

θ_{sep} Separation angle of AOD

ρ Density, Laser power factor

σ^2 Variance

τ Time

ω Frequency (radians)

ψ Mask function

Subscripts

0 Zeroth order, On axis, Initial

1 First-order, First

2 Second-order, Second

3 Third-order, Third

10 Decimal

a Acoustic

ac Acoustic center

ax Axial

b Bead

c Characteristic, Cutoff

CK Clock

Cov Covariance

d Disturbance

D Drag

esc Escape

e Effective

E External

f Fluid

F Maximum force, Feedback

G Gimbal-Mounted Mirror

H Horizontal

i Incident, index i, integral

l Linear

la Linear actuator

L Langevin (random thermal)

max Maximum

min Minimum

N Number of data

Ny Nyquist

o Immersion oil

OP Operating

p Proportional

PRBS Pseudo-Random Binary Sequence

r Relative, radial

$r90$ 90% Rise

rms Root mean squared

R Range of capture

s Sampling

$s5$ 5% Settling

T Trap

u Control signal (input)

v Filtered white noise disturbance

V Vertical

Var Variance

x Position on x-axis

y Position on y-axis, Output (measured)

λ Laser

μ Microscope objective (entrance aperture)

θ Angular

$*$ Actual value

Superscripts

$\wedge$ Estimate, Unit vector

$+$ Positive valued (Single-sided)

$\cdot$ First derivative

$\cdot\cdot$ Second derivative

$-$ Mean

LS Corresponding to LSE

Acronyms

AFM Atomic Force Microscope

AOD Acousto-Optic Deflector

ARX Auto-Regressive with Exogenous inputs

ARMAX Auto-Regressive Moving Average with Exogenous inputs

AS Asymptotic Stability

CCD Charge-Coupled Device

CW Continuous Wave

CT Continuous Time

DT Discrete Time

EFL Effective Focal Length

EOD Electro-Optic Deflector

FOV Field of View

GAS Global Asymptotic Stability

GMM Gimbal-Mounted Mirror

ISA Industry Standard Architecture

LQG Linear Quadratic Gaussian

LQR Linear Quadratic Regulator

LTI Linear Time Invariant

LSE Least Squares Estimator

MLE Maximum Likelihood Estimation

MSE Mean Square Error

NA Numerical Aperture

Nd:YAG Neodymium: Yttrium Aluminum Garnet

NG Normalized Gradient

NLS Normalized Least Squares

OD Optical Density

OEA Objective Entrance Aperture

OFM Optical Force Microscope

PE Persistence of Excitation

PRBS Pseudo-Random Binary Signal

KM Kinematic Mirror

PBS Phosphate-Buffered Saline

PBSC Polarizing Beam-Splitting Cube

PCI Peripheral Component Interconnect

PD Power Density

PEM Prediction Error Methods

PID Proportional Integral Derivative

PSD Position Sensing Detector

RLS Recursive Least Squares

RTSI Real-Time System Integration

SISO Single Input Single Output

TEM Transverse Electric and Magnetic

TPI Threads Per Inch

VI Virtual Instrument (*LabVIEW*)

ZOH Zero-Order Hold

List of Figures

List of Tables

Chapter 1

Introduction

The optical tweezer is a device that uses a focused laser beam to trap and manipulate individual dielectric particles in an aqueous medium. The laser beam is sent through a high numerical aperture (highly converging) microscope objective that is used for both trapping and viewing particles of interest. Known more descriptively as "single-beam gradient force optical traps", optical tweezers are also called "laser tweezers" and "single focused laser beam traps".

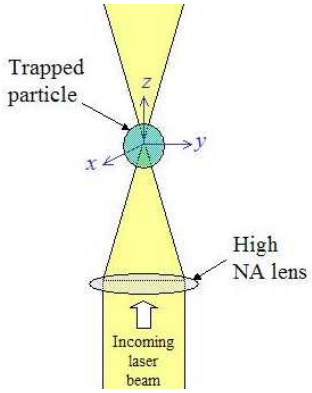

Figure 1.1: Basic optical tweezer. A single laser beam is focused to a diffraction-limited spot using a high numerical aperture microscope objective. Dielectric particles are trapped near the laser focus.

1.1 History

Although the trapping and manipulation of charged particles has been done with considerable facility for many years, the same cannot be said of neutral particles. The precursor to the optical tweezer, the optical levitator, was developed in 1970 [1]. It trapped particles by relying on the balance between upward radiation pressure and downward gravity. In that same year, Arthur Ashkin showed that micron-sized latex spheres could be trapped in water using two focused, counter-propagating laser beams. In 1978, he suggested that a strongly focused, single laser beam could be used to trap a particle even without gravity. He and his colleagues—Joseph Dziedzic, John Bjorkholm, and Steven Chu—at AT&T (Bell) Laboratories demonstrated the first working optical tweezer in 1986. Since then, optical tweezers have been used to trap dielectric particles

with diameters in the range of tens of nanometers to tens of microns [2, 3]. Ashkin and Dziedzic were awarded the 1993 Rank prize in optoelectronics for their groundbreaking work [4].

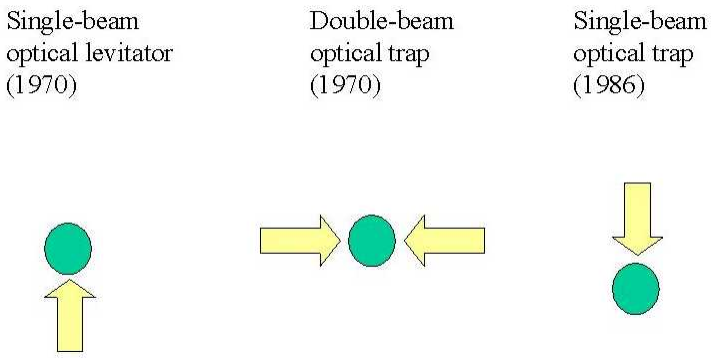

Figure 1.2: Evolution of optical tweezers.

The first commercial optical tweezer, known as "LaserTweezers®", was brought to market by Cell Robotics, Inc., of Albuquerque, New Mexico in 1992 [2]. In 2000, the basic *LaserTweezers* Workstation was priced at $56,000, not including the cost of a microscope [5]. One of its main drawbacks is that its motorized stage has a resolution of only $\sim$ 200 nm, which is insufficient for experiments that require nonometer-level resolution [6]. Arryx, Inc., of Chicago, uses optical tweezer technology in its "BioRyx® 200" system. This high-end turn-key product, which was brought to market in 2002, can be used to trap and independently steer up to 200 microscopic objects at a time [7]. The 1064 nm trapping system was priced at $377,500 in 2004; the minimum incremental motion of the traps is $\sim$ 20 nm [8].

1.2 Biophysical Applications

For small enough displacements from the center of the trap (up to, maximally, 100-300 nm) [9], the optical tweezer behaves like a Hookeian spring, characterized by a fixed trap-stiffness. Several milliwatts of laser power at the focus can generate trapping forces on the order of piconewtons, typically 1-100 pN [10]. While tiny by conventional standards, this level of force is well suited for biomolecular studies. For example, a force of 10 pN is sufficient to pull a bacterium such as *Escherichia coli* through water at ten times the speed at which it can swim [2].

According to Mehta et al., "a general goal in molecular biophysics is to characterize mechanistically the behavior of single molecules" [11]. Before the advent of optical tweezers, biophysicists did not possess a noninvasive tool capable of manipulating individual molecules. Instead, they would examine the behavior of a large clump of molecules and use various averaging techniques to infer the behavior of a single molecule. The optical tweezer has made such inference methods obsolete by enabling the direct study of individual molecules. Although biological molecules are too small to be trapped at room temperature, a molecule can be grasped once a trappable 'handle' is (biochemically) attached to that molecule as shown in Figure 1.3 [3]. Optical tweezers have been used "to trap and manipulate dielectric spheres, viruses, bacteria, living cells, organelles, colloidal gold, and even DNA. Such traps ... have measured elasticity, force, torsion, position, surface structure, and the interaction between particles" [12]. For trapped particles with a diameter of 1 μm, the range of forces that can be measured using an optical tweezer is 0.2–200 pN, which partially overlaps the 2–400 pN range in which a wide variety of cellular processes occur [13]. For studies that require larger forces, atomic force microscope (AFM) cantilevers

or glass microneedles are more suitable choices because they are stronger (less compliant) than optical tweezers [14].

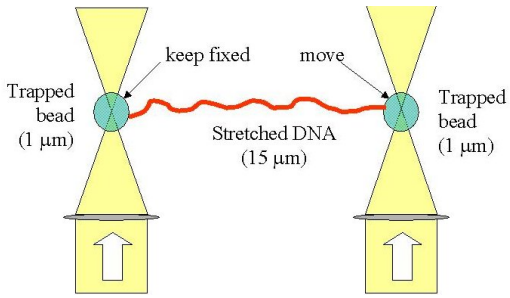

Figure 1.3: Typical biomechanics experiment. The ends of the DNA molecule are attached to polystyrene beads which are trapped and moved using optical tweezers.

Another reason for the popularity of optical tweezers in the field of cell biology is because they can be used to trap cells or organelles without damage [15]. By choosing a trapping laser with a wavelength in the near-infrared range, optical damage to biological specimens can be reduced by one or two orders of magnitude [16]. The first demonstration of successful (non-destructive) trapping of living viruses and bacteria was reported by Ashkin and Dziedzic in 1987 [17].

The following passage, excerpted from a 1996 paper by Visscher et al., summarizes why the biophysical community is excited about the development of optical tweezers:

> "Optical tweezers, when combined with ... position detectors [with nanometer resolution], offers two important advances: the ability to manipulate molecular-scale objects, by means of attached bead 'handles', and the ability to measure directly the forces and displacements on the molecular scale. Multiple traps, in particular, make possible experimental geometries not readily achieved with alternative technologies, such as scanning force microscopy (SFM) or glass microneedles. Moreover, the mechanical stiffness of an optical trap can be instantly changed, in contrast to these other approaches. Of particular importance are the noninvasive and nondestructive character of optically based measurements, as well as the unparalleled spatial and temporal control afforded by the use of light." [18]

A digital image of a 10-μm diameter polystyrene bead that was trapped using our optical tweezers is shown in Figure 1.4. The trapped bead can be seen near the center of the circular field of view (FOV) and an untrapped bead can be seen near the top of the FOV. Notice that the trapped bead is in better focus than the untrapped bead. The bright spot at the center of the trapped bead is a diffraction pattern caused by the trapping laser beam.

1.3 Organization of Dissertation

The main purpose of this dissertation is to analyze the properties of an optical tweezer from a control engineering point of view. As such, I make no attempt to investigate the fundamental physics behind optical trapping and I do not elaborate on its many applications in the field of biophysics. Instead, I have applied techniques from control theory to demonstrate new methods of analysis and practical tradeoffs in optical tweezer performance. By doing so, I hope to achieve two objectives:

1. Enhance the arsenal of tools available to users of optical tweezers, especially in biophysics and microfluidics.

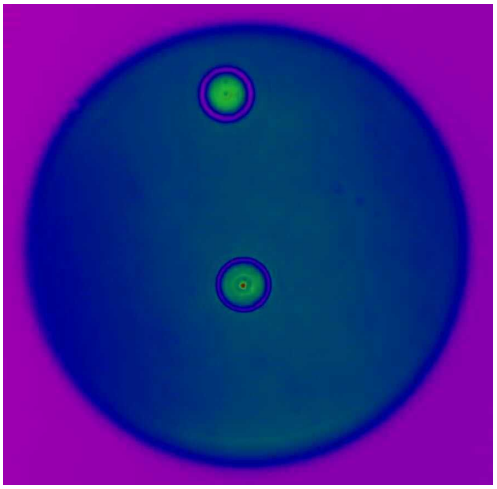

Figure 1.4: Image of a trapped 10-μm diameter polystyrene bead (center of FOV) and an untrapped bead (top of FOV).

2. Provide a framework that encourages future contributions from the control engineering community.

In accordance with the above objectives, I have written this dissertation using language and terminology that is intended for both engineers and life scientists. For the benefit of readers outside of the control community, I have occasionally included background material from control theory.

In Chapter 2, I briefly discuss the nature of optical forces acting on a small, dielectric sphere in an aqueous medium. An overview of two popular theoretical models for optical trapping–the ray optics model and the electromagnetic field model–is provided.

In Chapter 3, I describe the dynamics of a trapped particle using standard engineering terminology. After discussing different mathematical models of the optical trapping force in the lateral plane, I derive equations of motion for a trapped particle. Descriptions of the system are developed for both a cubic trapping force model and a linear force model; dynamic models are derived for both an inertial system and a non-inertial system. Parameters used to characterize the performance of optical tweezers are defined and practical factors that affect trapping strength are discussed. A microscopy requirement for consistent steering of trapped particles is also explained.

In Chapter 4, I analyze the dynamics of a trapped particle using stochastic control theory. The deterministic descriptions from Chapter 3 are converted into stochastic differential equations, which can be manipulated using the Fokker-Planck equation. Consequently, the probability distribution of a trapped particle is discussed and the mean first exit time of a trapped particle is computed numerically. Experimental results for the mean passage time within the linear region are included.

In Chapter 5, I describe construction of our research-grade optical tweezer. Practical details of the trapping system, viewing system, lateral steering system, position detection system, and computer interface are provided.

In Chapter 6, I describe procedures for calibrating the equipment used in our optical tweezer system. Information is provided for calibrating the manual micrometers, DC motors, Acousto-Optic Deflector (AOD), and position detectors.

In Chapter 7, I describe popular off-line identification methods using terminology from control theory. The equipartition method, the power spectrum method, and the step response method are discussed.

In Chapter 8, I propose the use of off-line calibration methods to achieve faster calibrations. The optical tweezer system is represented as a sampled-data system which allows the use of discrete time (DT) parameter estimation using Recursive Least Squares (RLS). This method is analyzed and simulated in some detail, including experimental results. The possibility of closed loop RLS is discussed, as is the possibility of nonlinear identification. The drawbacks of the continuous-time (CT) Normalized Gradient (NG) method are also mentioned.

In Chapter 9, I analyze linear feedback control. Theoretical expressions are derived for both PI control and LQG control. The performance, including limitations, of the linear controllers are studied using computer simulations.

In Chapter 10, I derive a nonlinear feedback control strategy that achieves Global Asymptotic Stability (GAS) of the origin. Controller performance is studied using computer simulations.

In Chapter 11, I summarize the conclusions that can be drawn from the material in this dissertation.

I have also included several appendices that provide relevant supplementary material. Appendix A describes the *LabVIEW* Virtual Instruments used for data acquisition; Appendix B provides comprehensive details of the construction procedure described in Chapter 5; Appendix C describes a nonlinear controller for stabilization of an inertial system; and Appendix D discusses future directions. A brief optical glossary is provided in Appendix E.

Chapter 2

Basic Theory

2.1 Optical Forces

For a dielectric particle trapped using an optical tweezer, the main optical forces can be divided into two categories: nonconservative absorption and scattering forces and conservative gradient forces. Absorption forces can be minimized by choosing a trapping frequency that is off-resonance [19]. Hence, only the scattering force and the gradient force are considered significant for optical tweezers[1] [21].

As its name suggests, the scattering force arises due to the direct scattering of photons, which is an incoherent interaction with light [3]. The scattering force acts in the same direction as incident light and is proportional to the intensity of incident light. The gradient force arises as a result of a coherent interaction with light in which "the laser field polarizes the atom, and the polarized atom experiences a force in the gradient of an electromagnetic field" [3]. Gradient forces occur whenever a transparent material with a refractive index greater than its surrounding medium is placed within a light gradient. The gradient force acts in the direction of increasing light intensity and is proportional to the gradient of light intensity.

If a dielectric particle is placed within the narrow waist of a sharply focused beam of light, the scattering force will have a tendency to push the particle away, while the gradient force will have a tendency to hold the particle within the waist (Figure 2.1). Stable trapping occurs when the gradient force is strong enough to overcome the scattering force. As shown in Section 3.5, a strong gradient force can be achieved by using a high numerical aperture[2] (NA) lens to focus a laser beam to a diffraction-limited spot.

2.2 Theoretical Models

Although the physics behind optical tweezers is not trivial, its behavior can be explained using two different theoretical models. For a trapped particle with diameter d much larger than the wavelength λ of the trapping laser ($d \gg \lambda$), a ray optics model shows good agreement with measured results, whereas for a particle with diameter much smaller than the trapping wavelength ($d \ll \lambda$), an electromagnetic field model provides best agreement [15]. In the intermediate size regime ($d \sim \lambda$), electromagnetic theory has yielded better results than ray optics, but neither model has been satisfactory [15, 22]. In the absence of an accurate model for the intermediate regime, the behavior of trapped particles in this regime is determined empirically.

[1] Another force, known as the optical binding force, can occur between two particles in intense light, but it will not be discussed here [20].

[2] To avoid algebraic confusion, when used in an equation, numerical aperture will be denoted as N_A instead of the more common notation, NA.

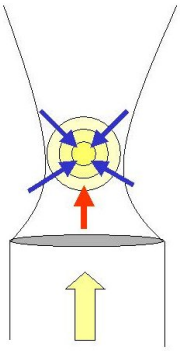

Figure 2.1: Optical forces. Gradient force is shown in blue; scattering force is shown in red.

2.2.1 Ray Optics Model

The ray optics model is valid for particles in the Mie regime in which particles are much larger than the laser wavelength (in practice, $d > 10\lambda$). According to this model, "the basic operation of optical tweezers can be explained by the momentum transfer associated with the redirection of light at a dielectric interface" [15]. When light hits a dielectric interface, part of the light will be refracted and part of it will be reflected[3]. Figure 2.2 shows a light ray with momentum $\vec{p_i}$ being incident upon a dielectric sphere with an index of refraction higher than the medium surrounding it.

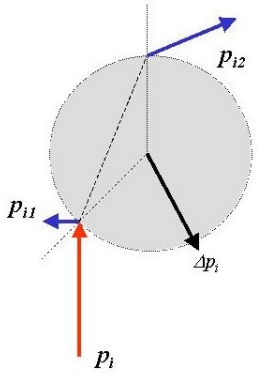

Figure 2.2: Qualitative ray optics model.

The light momentum reflected at the first interface is shown by $\vec{p_{i1}}$, while the light momentum that exits from the sphere after refraction at the second interface is shown by $\vec{p_{i2}}$. In reality, a small fraction of the light ray will be reflected back into the sphere, causing an infinite number of internal reflections, but this can be ignored during a first approximation. The net change of momentum of the single ray of light, $\Delta\vec{p_i}$, can be calculated by subtracting the momentum of the incident ray, $\vec{p_i}$, from the sum of the momenta of the exiting rays, $\vec{p_{i1}} + \vec{p_{i2}}$. By representing the light beam as a collection of light rays, the total change of light momentum $\Delta\vec{p_\lambda}$ can be

[3]Absorption effects are ignored.

calculated by summing the individual $\Delta\vec{p_i}$ components:

$$\Delta\vec{p_\lambda} = \sum_i \Delta\vec{p_i} = \sum_i (\vec{p_{i1}} + \vec{p_{i2}} - \vec{p_i}). \tag{2.1}$$

From Newton's Second Law, the resulting force $\vec{F_\lambda}$ acting on the light is given by the rate of change of light momentum.

$$\vec{F_\lambda} = \lim_{\Delta t \to 0} \frac{\Delta\vec{p_\lambda}}{\Delta t}, \tag{2.2}$$

According to Newton's Third Law, the dielectric sphere will experience an equal and opposite trapping force, $\vec{F_T}$:

$$\vec{F_T} = -\vec{F_\lambda}. \tag{2.3}$$

The above equations ignore internal reflections and polarization effects. The net effect of internal reflections is to add to the scattering force, making the trap weaker. In practice, the equilibrium position of the sphere lies slightly beyond the focal point of the beam. In fact, ray optics theory predicts that the exact equilibrium location of the trap should be approximately 3-5% of the sphere diameter beyond the laser focus [15]. For rigorous ray optics force calculations for 1-μm spheres trapped using a Gaussian laser beam, consult [23]. Arthur Ashkin's diagrams of the (restoring) trapping force show the trapping force acting on a dielectric sphere (index of refraction $n = 1.57$–1.58) as a function of the sphere's position relative to a laser beam focus [23]. Polystyrene (C_8H_8) beads are commonly used for trapping. Polystyrene has a density of 1040-1070 kg/m^3, dielectric constant of 2-2.8, electric resistivity of 10^{13}-10^{15} Ωm, heat capacity of 1200-2100 J/kg.K, thermal conductivity of 0.12-0.193 W/m.K, and visible transmission of 80-90% [24]. Since water and polystyrene have almost identical densities, the net force due to gravity can be neglected[4].

2.2.2 Electromagnetic Field Model

The electromagnetic field model, also known as the Lorentz force model, is valid for particles in the Rayleigh regime in which particles are much smaller than the laser wavelength (in practice, $d < 0.4\lambda$). It is based on "the Lorentz force exerted by the trapping light on the atoms in the trapped object" [12], but its details will not be discussed here. This model shows that the potential energy of a trapped particle is proportional to the negative of the light intensity, $-I$. Hence, the potential energy of the trapped particle will be at its minimum where the light intensity is at its maximum. Since the maximum intensity of a focused beam of light is at its focus, the trapped particle will be attracted to the focus. The trapping force is proportional to the intensity gradient ∇I.

[4]Most experiments have a short-enough time scale that gravity can be ignored.

Chapter 3

Trap Dynamics

3.1 Trap Force Model

As mentioned in Section 2.2, in the absence of an accurate theoretical model for trapped particles that are roughly the same size as the trapping laser wavelength ($d \sim \lambda$), the trapping characteristics of optical tweezers in this regime are determined empirically. Figure 3.1 shows the lateral trapping force F_T of a trapped 1-μm diameter bead for laser power of approximately 100 mW (at the focus) as obtained by Simmons et al. [10].

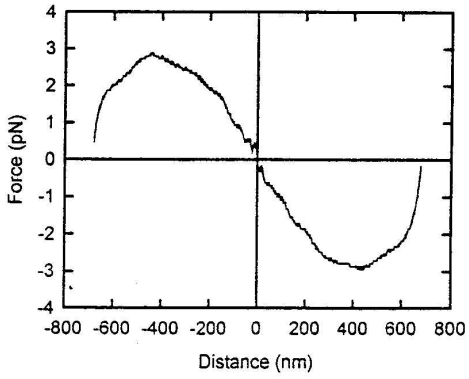

Figure 3.1: Optical trapping force model obtained by Simmons et al. for a 1-μm diameter bead for laser power of approximately 100 mW (at the focus) using a 63×, 1.25 NA microscope objective [10]. The horizontal axis shows the relative position x_r of the bead from the center of the trap. Re-printed with permission from Jim Spudich.

The relative position x_r is defined as

$$x_r := x - x_T, \tag{3.1}$$

in which x_T is the trap (laser focus) position, as shown in Figure 3.2.

Figure 3.1 shows that their trap exerts a linear restoring force for relative displacements x_r of up to 200 nm [10]. Furthermore, the restoring force reaches a peak of approximately 2.85 pN at about 450 nm and then falls off steeply up to about 675 nm [10]. The trap has no effect on beads that are more than 675 nm from the trap center. The curve confirms Ashkin's ray-optics calculations that predict that the maximum trapping force occurs at about one bead radius [23].

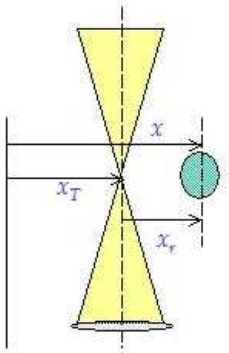

Figure 3.2: Definition of lateral position coordinates: x is particle position, x_T is trap position, and x_r is relative position.

Although the magnitude of the force shown in Figure 3.1 will vary depending on parameters such as laser power and numerical aperture (discussed in Section 3.5), the curve accurately depicts the qualitative trapping behavior of a well-aligned optical tweezer, as discussed in [23].

For relative displacements within the trapping radius (range of influence) R, the trap behaves like a third-order nonlinear restoring spring:

$$F_T = \begin{cases} \alpha_3 x_r^3 - \alpha_1 x_r & \text{for } |x_r| < R = \sqrt{\frac{\alpha_1}{\alpha_3}} \\ 0 & \text{otherwise.} \end{cases} \tag{3.2}$$

The effective trap stiffness is defined as

$$\alpha_e(x_r) := -\frac{F_T}{x_r}, \tag{3.3}$$

which, according to the cubic model (3.2), can be expressed as

$$\alpha_e = \begin{cases} \alpha_1 - \alpha_3 x_r^2 & \text{for } |x_r| < R = \sqrt{\frac{\alpha_1}{\alpha_3}} \\ 0 & \text{otherwise.} \end{cases} \tag{3.4}$$

Figure 3.3 shows a cubic trapping force model for $\alpha_3 = 22$ pN/μm^3, $\alpha_1 = 10$ pN/μm, and $R = 0.675$ μm. The maximum restoring force of 2.595 pN occurs at $|x_r| = R_F = 0.3893$ μm. The nonlinear spring constants α_1 and α_3 were obtained by fitted a cubic polynomial to the experimental curve shown in Figure 3.1. To emphasize that the trapping force model (3.2) is a restoring force that acts radially in the lateral plane, Figure 3.3 is shown as a surface plot in Figure 3.4.

Within the linear region of $|x_r| \leq R_l < R$ ($R_l = 0.2$ μm in Figure 3.1), the trap stiffness is approximately constant ($\alpha \approx 10$ pN/μm in Figure 3.1), and the trapping force is linear with respect to relative displacement:

$$F_T = \ -\alpha x_r \quad \text{for } |x_r| < R_l. \tag{3.5}$$

The linear force model (3.5) differs from the nonlinear force model (3.2) by a factor of $\frac{\alpha_3 x_r^2}{\alpha_1}$, which is equal to 8.8% at $x_r = R_l$, for the stiffness coefficients used in Figure 3.3. We define the characteristic frequency ω_c of the trapped particle as

$$\omega_c := \frac{\alpha}{\beta}, \tag{3.6}$$

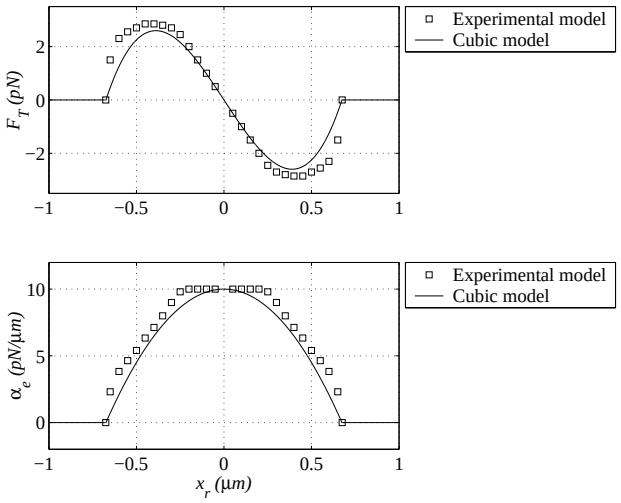

Figure 3.3: Cubic optical force model for a 1-μm diameter bead. Top figure shows trapping force; bottom figure shows effective stiffness. Experimental model is from Figure 3.1.

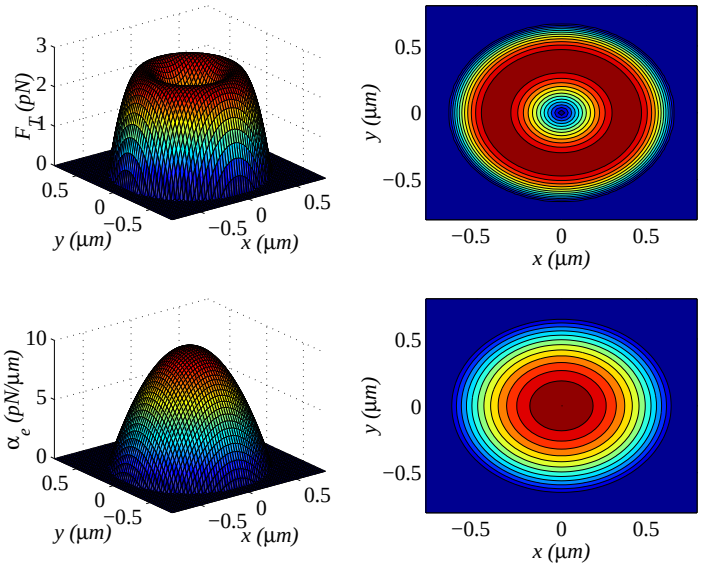

Figure 3.4: Cubic optical trapping force model in the lateral plane. Top plots show trapping force; bottom plots show effective stiffness. Restoring force is directed towards origin (i.e., towards position of trap)

where frequency is measured in radians per second.

Figure 3.5 compares the different trapping force models. From the leftmost plots, it is clear that the linear force model overestimates the experimental force model outside of the linear region. On the other hand, the cubic force model underestimates the experimental force model everywhere (except at the origin), but has a similar profile throughout the trapping radius. Hence, we can view the cubic force model as a useful, but conservative estimate of the

experimental force model. When considering motion that is restricted to the linear region, it is appropriate to use the simple linear force model, keeping in mind that the cubic model's departure from linearity is under 9% within the linear region. For motion outside of the linear force region, the cubic model can be used as a convenient approximation of the experimental force model.

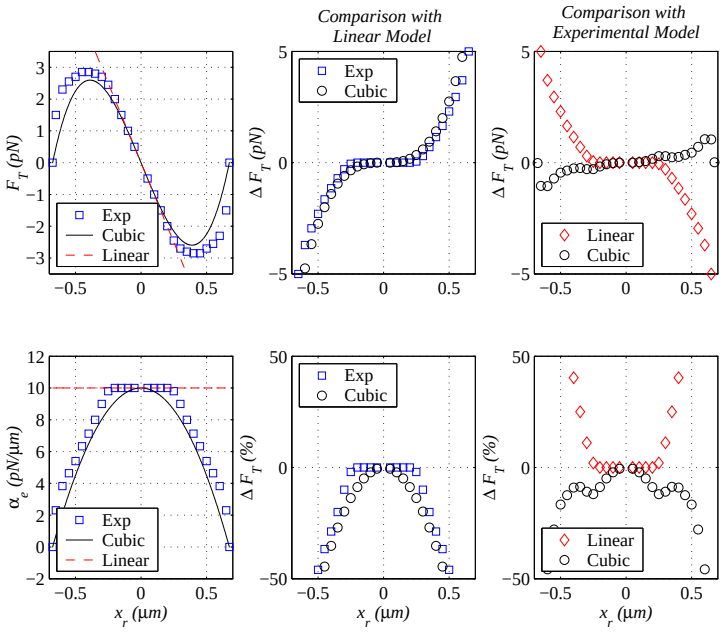

Figure 3.5: Comparison between different trapping force models. Leftmost plots show trapping force and effective trap stiffness; middle plots show deviations from the linear model; rightmost plots show deviations from the experimental model.

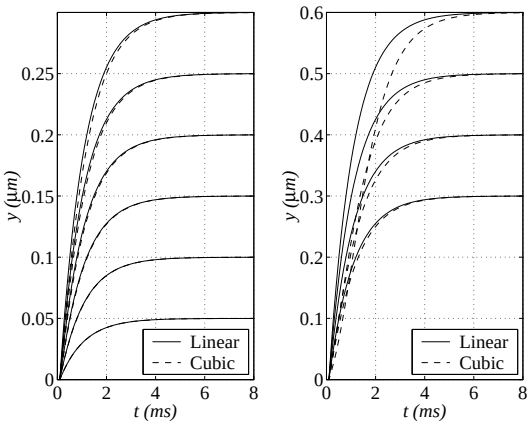

Figure 3.6: Step responses for linear and cubic models. Left plot shows response to small steps; right plot shows response to larger steps.

Figure 3.7 shows the difference between the cubic and linear step responses. For a step of

100 nm, the cubic step response lags the linear step response by, at most, about 2.3%. For a step of 200 nm, the lag is under 9%.

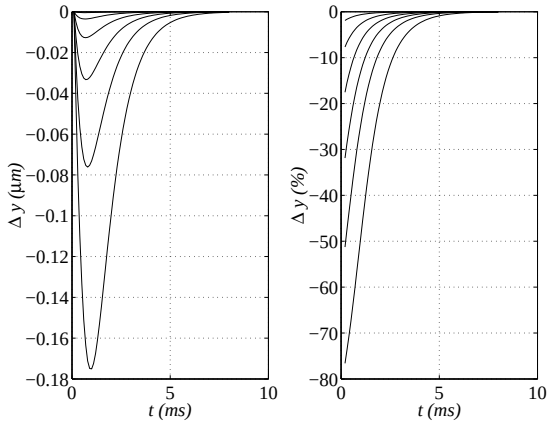

Figure 3.7: Difference between step responses for linear and cubic trapping force models. Left plots show differences; right plots show the differences as a percentage of the linear response.

3.2 Equation of Motion along a Lateral Axis

The equation of motion along the x-axis for a trapped bead of mass m and lateral position x is given by

$$m\ddot{x} = F_T(x_r) + F_D(\dot{x}) + F_L(t) + F_E(t), \tag{3.7}$$

where $F_T(\cdot)$ is the optical trapping force, $F_D(\cdot)$ is the viscous drag, $F_L(\cdot)$ is a Langevin (random thermal) force, and $F_E(\cdot)$ is an external force. The drag force can be expressed as

$$F_D = -\beta\dot{x}, \tag{3.8}$$

where $\beta > 0$ is the viscous damping factor from Stoke's equation,

$$\beta = 6\pi\eta_f r_b, \tag{3.9}$$

in which r_b is the bead radius and η_f is the fluid viscosity. For a 1-μm diameter polystyrene bead in water at 20°C (68°F),

$$\begin{aligned} m &= \rho \times \frac{4}{3}\pi r^3 \\ &= 1050\frac{\text{kg}}{\text{m}^3} \times \frac{4}{3}\pi(0.5 \times 10^{-6}\ \text{m})^3 \\ &= 5.50 \times 10^{-16}\ \text{kg} \\ &= 5.50 \times 10^{-10}\ \text{mg} \end{aligned}$$

and

$$\begin{aligned}\beta &= (6\pi \times 10^{-3}\ \frac{\text{Ns}}{\text{m}^2}) \times (0.5 \times 10^{-6}\ \text{m}) \\ &= 3\pi \times 10^{-9}\ \frac{\text{Ns}}{\text{m}} \\ &= 9.42 \times 10^{-3}\ \frac{\text{pNs}}{\mu\text{m}} \\ &\approx 0.01\ \frac{\text{pNs}}{\mu\text{m}}.\end{aligned}$$

It should be noted that the viscosity of a liquid decreases dramatically with temperature [25]. For example, at 40°C (104°F), the viscosity of water is approximately $0.6 \times 10^{-3}\ \frac{\text{Ns}}{\text{m}^2}$ [25]. The Langevin force $F_L(t)$ has an average value of zero,

$$E\{F_L(t)\} = 0,$$

and constant, single-sided power spectrum $S_L^+(f)$ (i.e., ideal white noise force) given by [26]

$$S_L^+(f) = 4\beta k_B T, \tag{3.10}$$

in which k_B is Boltzmann's constant and T is the absolute temperature [18]. At biological temperatures, $k_B T$ is approximately 4×10^{-3} pNμm [26]. Hence, for a 1-μm diameter polystyrene bead,

$$\begin{aligned}S_L^+(f) &\approx 4 \times 0.01\ \frac{\text{pNs}}{\mu\text{m}} \times (4 \times 10^{-3}\ \text{pN}\mu\text{m}) \\ &= 1.6 \times 10^{-4}\ \frac{\text{pN}^2}{\text{Hz}}.\end{aligned}$$

The nature of the external force $F_E(t)$ will depend on experimental conditions. For example, in biological experiments, the external force may arise due to the interaction between biological particles.

3.2.1 Nonlinear Trapping Region

Equations (3.2) and (3.8) can be substituted into (3.7) to obtain the equation of motion for a trapped particle in the nonlinear trapping region:

$$m\ddot{x} = \psi(x_r)(\alpha_3 x_r^3 - \alpha_1 x_r) - \beta\dot{x} + F_L(t) + F_E(t), \tag{3.11}$$

in which the mask function

$$\psi(x_r) := \begin{cases} 1 & \text{for } |x_r| < R \\ 0 & \text{otherwise.} \end{cases} \tag{3.12}$$

Nonlinear Inertial Representation

Defining the control input u as the trap position x_T,

$$u := x_T, \tag{3.13}$$

we can express (3.11) in state space form as

$$\begin{aligned}\dot{x}_1 &= x_2 \\ \dot{x}_2 &= -\frac{\beta}{m}x_2 + \frac{\psi(x_1 - u)}{m}\left[\alpha_3(x_1 - u)^3 - \alpha_1(x_1 - u)\right] + \frac{1}{m}F_L + \frac{1}{m}F_E \\ y &= x_1,\end{aligned} \tag{3.14}$$

where $x_1 := x$ and $x_2 := \dot{x}$.

Nonlinear Noninertial Representation

As trapped particle size is scaled down towards the nano-scale, surface forces tend to dominate bulk properties and forces due to a property known as the scaling effect [27]. For example, for a sphere, surface to volume ratio is inversely proportional to radius. As a consequence of the scaling effect, for a microscopic particle bound in a harmonic potential at low Reynolds' number (i.e., "small particles moving not too fast in a viscous medium"), viscous drag dominates inertia [26]. In other words, the mass m of the trapped particle is small enough that it can be ignored in practice. For example, according to (3.6) and (3.4), the effective characteristic frequency of the trap shown in Figure 3.3 is given by $(\omega_c)_e = \frac{\alpha_e}{\beta} \leq \frac{\alpha_1}{\beta} \approx 1$ krad/s. Therefore, $m\omega_c \leq 5.5 \times 10^{-7}$ $\frac{\text{pNs}}{\mu\text{m}}$, which is negligible compared to $\beta \approx 0.01$ $\frac{\text{pNs}}{\mu\text{m}}$. Hence, (3.11) can be simplified to obtain the noninertial equation of motion for a trapped particle in the nonlinear trapping region:

$$0 = \psi(x_r)(\alpha_3 x_r^3 - \alpha_1 x_r) - \beta\dot{x} + F_L(t) + F_E(t). \tag{3.15}$$

For contemporary optical tweezer systems (in which trapped particles have negligible mass), the above nonlinear noninertial representation is accurate for all practical purposes. Equation (3.15) can be expressed in state space form as:

$$\begin{aligned} \dot{x} &= \frac{\psi(x-u)}{\beta}\left[\alpha_3(x-u)^3 - \alpha_1(x-u)\right] + \frac{1}{\beta}(F_L + F_E) \\ y &= x. \end{aligned} \tag{3.16}$$

Both inertial and noninertial open loop systems can be represented by the block diagram shown in Figure 3.8, in which output measurement noise n is included for completeness. The Langevin force and the external force can be interpreted as disturbances.

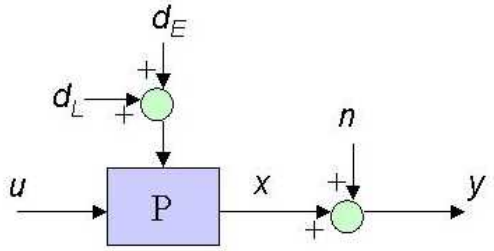

Figure 3.8: Open loop block diagram. Here $u := x_T$, $d_L := F_L$, $d_E := F_E$, and n is measurement noise.

3.2.2 Linear Trapping Region

From (3.5), (3.8), and (3.7), the equation of motion for a trapped particle in the linear trapping region is given by

$$m\ddot{x} = -\alpha x_r - \beta\dot{x} + F_L(t) + F_E(t) \quad \text{, for } |x_r| \leq R_l. \tag{3.17}$$

Linear Inertial Representation

We can express (3.17) in state space form as

$$\begin{aligned}\begin{bmatrix} \dot{x}_1 \\ \dot{x}_2 \end{bmatrix} &= \begin{bmatrix} 0 & 1 \\ -\frac{\alpha}{m} & -\frac{\beta}{m} \end{bmatrix} \begin{bmatrix} x_1 \\ x_2 \end{bmatrix} + \begin{bmatrix} 0 \\ \frac{\alpha}{m} \end{bmatrix} u + \begin{bmatrix} 0 \\ \frac{1}{m} \end{bmatrix} (F_L + F_E) \\ y &= \begin{bmatrix} 1 & 0 \end{bmatrix} \begin{bmatrix} x_1 \\ x_2 \end{bmatrix}, \end{aligned} \tag{3.18}$$

where $u := x_T$, $x_1 := x$, and $x_2 := \dot{x}$ as before. For zero initial conditions, (3.18) can also be expressed using Laplace transforms as:

$$X(s) = G_{yu}(s)U(s) + G_{yd}(s)\left[F_L(s) + F_E(s)\right], \tag{3.19}$$

where the second order transfer function from control to output is given by

$$G_{yu}(s) = \frac{\frac{\alpha}{m}}{s^2 + \frac{\beta}{m}s + \frac{\alpha}{m}}, \tag{3.20}$$

and the second order transfer function from disturbance to output is given by

$$G_{yd}(s) = \frac{\frac{1}{m}}{s^2 + \frac{\beta}{m}s + \frac{\alpha}{m}}. \tag{3.21}$$

Linear Noninertial Representation

Assuming the particle mass is negligible compared to the viscous drag, we can express (3.17) as

$$0 = -\alpha x_r - \beta\dot{x} + F_L(t) + F_E(t) \quad \text{, for } |x_r| \le R_l, \tag{3.22}$$

which can be written in state space form as

$$\begin{aligned}\dot{x} &= -\frac{\alpha}{\beta}x + \frac{\alpha}{\beta}u + \frac{1}{\beta}(F_L + F_E) \\ y &= x. \end{aligned} \tag{3.23}$$

Clearly, as before, the Langevin force and the external force can be interpreted as disturbances. For zero initial conditions, (3.23) can be expressed using Laplace transforms as:

$$X(s) = G_{yu}(s)U(s) + G_{yd}(s)\left[F_L(s) + F_E(s)\right]. \tag{3.24}$$

For the noninertial case, the first order transfer function from control to output is given by

$$G_{yu}(s) = \frac{\frac{\alpha}{\beta}}{s + \frac{\alpha}{\beta}}, \tag{3.25}$$

while the first order transfer function from disturbance to output is given by

$$G_{yd}(s) = \frac{\frac{1}{\beta}}{s + \frac{\alpha}{\beta}}. \tag{3.26}$$

For the linear case, we can specify interconnections within the plant P as shown in Figure 3.9. Clearly, Figure 3.8 is also valid for the linear case.

The Bode plot of the transfer functions (3.25) and (3.26) are shown in Figure 3.10 for $\alpha = 10$ pN/μm, $\beta = 0.01$ pNs/μm. The step responses are shown in Figure 3.11. The open loop 90% rise time $t_{r90} = 2.3$ ms and the 5% settling time $t_{s5} = 3.0$ ms. The figures clearly illustrate that the only difference between G_{yu} and G_{yd} is a gain factor of α, which is equal to 10 (20 dB) for these plots.

Substituting the characteristic frequency of the trap from (3.6), the transfer function from control to output can be re-expressed as

$$G_{yu}(s) = \frac{\omega_c}{s + \omega_c}. \tag{3.27}$$

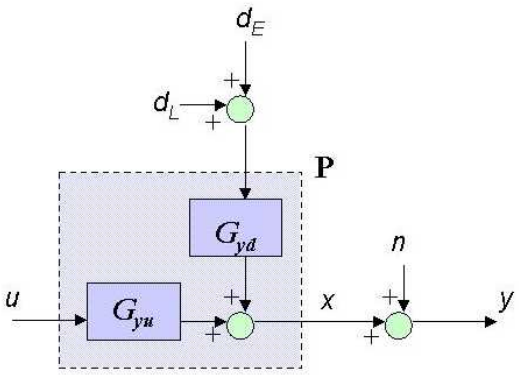

Figure 3.9: Linear plant block diagram. Here $u := x_T$, $d_L := F_L$, and $d_E := F_E$.

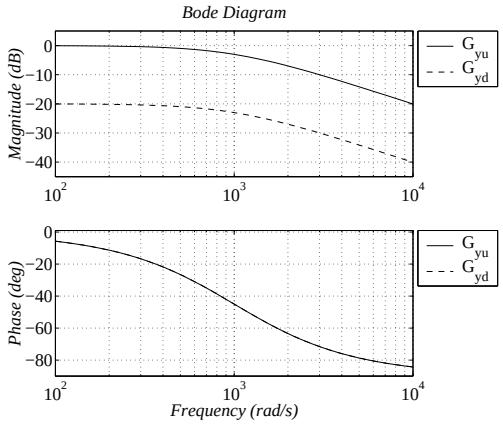

Figure 3.10: Linear plant Bode plots for $\alpha = 10$ pN/μm, $\beta = 0.01$ pNs/μm.

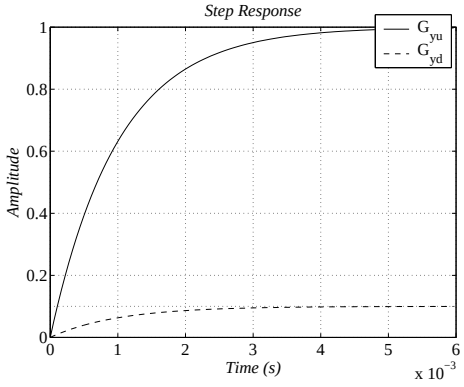

Figure 3.11: Linear plant step responses $\alpha = 10$ pN/μm, $\beta = 0.01$ pNs/μm.

3.3 Equations of Motion in the Lateral Plane

In Section 3.2, we described the equations of motion along a single lateral axis that goes through the origin. In practice, ofcourse, we are interested in motion in the entire lateral plane. To obtain an expression for two-dimensional motion, we use the fact that the trapping force F_T is symmetric about the vertical z direction, as shown in Figure 3.4. The one-dimensional optical trapping force along any radial axis through the relative origin (trap position) is given by Figure 3.3. Accordingly, we can use plane polar coordinates r and θ to describe the two-dimensional equation of motion of a trapped bead. For the purposes of this chapter, we will assume the usual relation between polar and Cartesian coordinates given by

$$r = \sqrt{x^2 + y^2} \tag{3.28}$$

$$\theta = \tan^{-1}\left(\frac{y}{x}\right) \tag{3.29}$$

with unit vectors denoted by $\hat{r}$ and $\hat{\theta}$ [28]. We define the relative radial position r_r and the relative angle θ_r according to Figure 3.12.

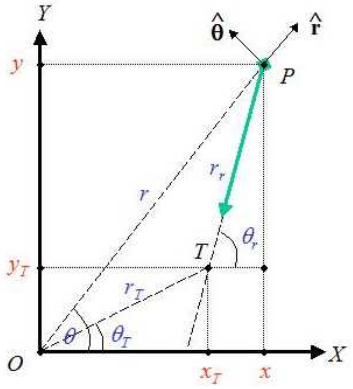

Figure 3.12: Diagram for derivation of planar equations of motion.

Note that, in general,

$$r_r \neq r - r_T$$

$$\theta_r \neq \theta - \theta_T.$$

Comparing with (3.16), the planar noninertial equations of motion can be written in Cartesian coordinates as

$$\dot{x} = \frac{\psi(r_r)}{\beta}\left[\alpha_3 r_r^3 - \alpha_1 r_r\right]\cos\theta_r + \frac{1}{\beta}(F_{Lx} + F_{Ex}) \tag{3.30}$$

$$\dot{y} = \frac{\psi(r_r)}{\beta}\left[\alpha_3 r_r^3 - \alpha_1 r_r\right]\sin\theta_r + \frac{1}{\beta}(F_{Ly} + F_{Ey}), \tag{3.31}$$

where the additional x and y subscripts on the Langevin and external forces indicate the direction of those forces. Furthermore, the planar noninertial equations of motion can be written in polar coordinates as

$$\dot{r} = \frac{\psi(r_r)}{\beta}\left[\alpha_3 r_r^3 - \alpha_1 r_r\right]\cos(\theta_r - \theta) + \frac{1}{\beta}(F_{Lr} + F_{Er}) \tag{3.32}$$

$$\dot{\theta} = \frac{\psi(r_r)}{r\beta}\left[\alpha_3 r_r^3 - \alpha_1 r_r\right]\sin(\theta_r - \theta) + \frac{1}{r\beta}(F_{L\theta} + F_{E\theta}), \tag{3.33}$$

which can be derived by considering the velocity of the particle in the $\hat{r}$ and $\hat{\theta}$ directions [1]. Note that, in the special case when the trap position is at the origin ($r_T = 0 \Rightarrow \theta_r = \theta$), we can simplify the planar equations of motion to obtain

$$\dot{x} = \frac{\psi(r)}{\beta}\left[\alpha_3 r^3 - \alpha_1 r\right]\cos\theta + \frac{1}{\beta}(F_{Lx} + F_{Ex}) \tag{3.34}$$

$$\dot{y} = \frac{\psi(r)}{\beta}\left[\alpha_3 r^3 - \alpha_1 r\right]\sin\theta + \frac{1}{\beta}(F_{Ly} + F_{Ey}), \tag{3.35}$$

and

$$\dot{r} = \frac{\psi(r)}{\beta}\left[\alpha_3 r^3 - \alpha_1 r\right] + \frac{1}{\beta}(F_{Lr} + F_{Er}) \tag{3.36}$$

$$\dot{\theta} = \frac{1}{r\beta}(F_{L\theta} + F_{E\theta}). \tag{3.37}$$

Note that (3.36) is precisely the state equation given in (3.16). Clearly, the angular velocity expressions (3.33) and (3.37) are not well-defined for particles at the origin ($r = 0$), which severely limits the usefulness of the angular state equations. In practice, we often consider only radial position.

3.4 Trap Characterization Parameters

In experiments in which the optical tweezer is used purely as a holding device, accurate calibration of the trapping forces is not important. However, in experiments that investigate the forces that arise due to various (usually biophysical) interactions, the trapping forces must be accurately quantified. If well aligned, the optical tweezer should exert a cylindrically symmetric force about the z-axis. While theoretical prediction of trapping forces is not easy, the forces can be calibrated empirically. A complete characterization of the trap requires calibration of both the axial as well as lateral trapping forces, but one is interested mostly in the lateral trapping capabilities (in the horizontal plane of the specimen) because it provides greater operating range [18]. Figure 3.13 shows a qualitative profile of the lateral force F_T of an optical trap as a function of bead displacement from the center of the trap [10].

3.4.1 Range of Influence

The range of influence R of the trap is the maximum distance that a stationary sphere can be placed away from the trap center and still be attracted towards the trap. The lateral range of influence can be found by placing a particle at a known lateral distance from the center of the trap with the trap turned off. Once the trap is turned on, if the particle is attracted towards the trap, it is within the range of influence. This procedure can be repeated for increasing lateral distances until the trap no longer influences the particle. In addition to the range of influence R, the linear force range R_l (Section 3.4.3) and the maximum force range R_F (Section 3.4.2) are also important parameters [29].

3.4.2 Strength (Maximum Force)

The strength of the trap is the maximum restoring force $(F_T)_{\max}$ that it can exert on a trapped particle. For large beads, the maximum force should be reached when the bead is roughly one bead radius r_b away from the trap center [10]. The maximum force range R_F is defined as the radius at which the maximum restoring force occurs. The circular locus of maximum force radii can be clearly seen in Figure 3.4.

[1] The velocity of the particle at polar coordinates (r, θ) is given by $\vec{v} = \dot{r}\hat{r} + r\dot{\theta}\hat{\theta}$ [28].

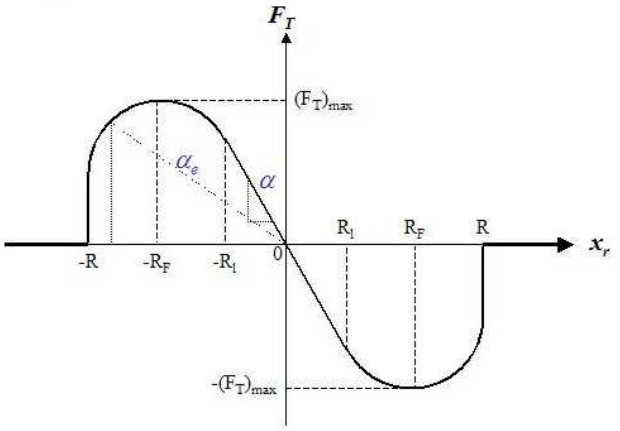

Figure 3.13: Qualitative lateral force profile of an optical trap.

3.4.3 Trap Stiffness

From (3.3), the effective trap stiffness α_e is defined such that

$$F_T = -\alpha_e x_r. \tag{3.38}$$

As shown in Figure 3.4, for small $|x_r|$, that is, within the linear force range R_l, $\alpha_e \approx \alpha$ is constant. Outside of R_l, $\alpha > \alpha_e(x_r) > 0$, which corresponds to the nonlinear force regime and for large $|x_r|$, $\alpha_e = 0$, which implies that the particle is outside of the range of influence R. According to Visscher and Block, "The stiffness of a trap, and the region over which it remains invariant, depend, in nontrivial ways on the optical wavelength and power, as well as the size, shape, and refractive index of the particle, and the refractive index of the surrounding medium" [30].

3.4.4 Capture Range Velocity

The capture range velocity v_R is the maximum velocity of moving particles at which the optical tweezers can slow down and trap the particles [31]. To account for statistical variations, Grego et al. defined the capture range velocity, v_R, as the velocity at which more than 50% of the tested particles passing through a focused volume around the laser waist are captured by the trap [31].

3.5 Trap Strength Factors

The strength of the trap is given by the expression

$$(F_T)_{\max} = Q\left(\frac{n_f P_T}{c_0}\right), \tag{3.39}$$

where Q is a dimensionless efficiency factor "that depends on the numerical aperture, laser wavelength, light polarization state, laser mode structure, relative index of refraction, and geometry of the [trapped] particle"[2] [20]. The quantity $\frac{n_f P_T}{c_o}$ is the incident momentum per second for

[2] A maximum efficiency of $\max(Q) = 2$ corresponds to the limiting case of reflection due to a plane mirror.

a laser beam of power P_T (at the focus) in a fluid medium of index of refraction n_f, where c_o is the velocity of light in vacuum. Using up to 1 W of laser power, typical trap strengths are on the order of tens of piconewtons [26]. The laser power P_T at the focus can be estimated by measuring the laser power just before the beam enters the microscope and then accounting for the fractional throughput of the microscope objective. Typical objectives absorb half or more of the laser light that enters the OEA [9]. Svoboda and Block measured a transmittance value of $59 \pm 2\%$ for the same objective as ours when trapping at $\lambda = 1064$ nm [20].

3.5.1 Laser

Laser Power

The strength of the trap is directly proportional to the laser power at the trap [12]. This follows from (3.39) in which Q is independent of P_T. Therefore, for a given trap configuration,

$$(F_T)_{\max} \propto P_T.$$

Although nonlinear optical force effects can occur at extremely high power densities, these effects are negligible for power densities on the order of 10^{11} W/m^2 or less [19].

Laser Focus

The strength of the trap will increase as the size of the focused spot is decreased. This occurs because, for a fixed laser power, the intensity gradient is highest when the focus spot is smallest. For a collimated laser beam of diameter d_λ and wavelength λ incident upon an ideal lens with focal length f_μ, the trap spot size w_T is diffraction-limited according to

$$w_T \geq \frac{1.22 f_\mu \lambda}{2 d_\lambda} = \frac{1.22\lambda}{n_f}\sqrt{\left(\frac{n_f}{N_A}\right)^2 - 1}, \tag{3.40}$$

where n_f is the index of refraction of the fluid medium and N_A is the numerical aperture of the lens [12]. In practice, to achieve sufficiently strong trapping, the microscope objective should be chosen such that $N_A \geq 1$ [20].

Laser Polarization

Lateral trapping forces depend on the state of polarization of the light. For equal laser power levels, "the lateral forces parallel to the polarization are about 10% greater than the lateral forces perpendicular to it" [32]. However, polarization has negligible effect on axial trapping forces [32].

3.5.2 Trapped Particles

Particle Size

Strongest trapping is expected for particles that are roughly the same size as the laser wavelength [14]. In particular, for the commonly used laser wavelength of approximately 1 μm, Gittes and Schmidt claim that trapped particles should be roughly matched in size to the laser focus, which is approximately 0.5 μm [26]. For large particles (in the Mie regime), the trapping force should be independent of particle radius r_b, whereas for small particles (in the Rayleigh regime), the trapping force should be proportional to r_b^3 [23]. Felgner et al. found that the trapping efficiency Q increased with bead diameter [15].

Particle Displacement Direction

The restoring force is weakest when the trapped particle is displaced from the trap center in the axial direction of light propagation (away from the lens) and the restoring force is strongest when the particle is displaced in the opposite axial direction [12]. The restoring force has intermediate strength when the particle is displaced in the transverse (lateral) plane.

3.6 Steering Consistency Requirements

To construct a movable trap that is consistent (i.e., constant trapping power, regardless of beam movement), the laser beam must satisfy two requirements (Figure 3.14):

1. The beam should pivot around the microscope objective entrance aperture (OEA), and
2. The beam should (slightly) overfill the OEA by the same amount even when the beam is moved [21].

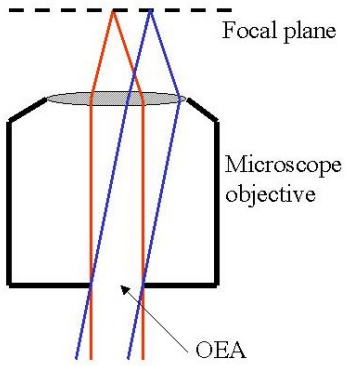

Figure 3.14: Steering consistency requirements.

Since commercial microscope objectives are not designed for use with lasers, the thin back cover surrounding the OEA may become deformed due to heat damage. Therefore, in many laser applications, the back cover of the microscope objective is removed. Once the back cover has been removed, the steering consistency requirements mentioned above are not as crucial as they would be if the back cover were in place. Even then, the steering system should be designed to conform with the steering consistency requirements because the microscope objective has been designed specifically for light that enters through the OEA.

Chapter 4

Stochastic Analysis

As described in Section 3.2, a trapped particle experiences random position fluctuations due to the Langevin force. As a result, the optical tweezer is an inherently stochastic system. In this chapter, we will recast the deterministic equations of motion from Section 3.2 in a form that is more suitable for stochastic analysis[1].

As mentioned in Section 3.5, the trapping force of an optical tweezer is proportional to the laser power. In this chapter, we will denote the laser power by the factor $\rho > 0$, which is defined relative to the power level used in [10]. For example, $\rho = 1$ corresponds to the same laser power level used to obtain Figures 3.1 and 3.3, which is approximately 100 mW (at the focus) [10]. The trapping force also increases with numerical aperture, so the force model (3.2), and therefore, the material in this section, are quantitatively accurate for a 1.25 NA (numerical aperture) microscope objective, which was used in [10]. However, as shown in [23], the trapping force for a spherical particle always has a profile that qualitatively matches (3.2). Therefore, our results can be extended qualitatively to higher numerical apertures (for example, NA = 1.30 or 1.40), if necessary.

As shown in Figure 3.4, an optical tweezer traps particles in not only one, but three dimensions. For a well-aligned trap, the trapping profile is cylindrically symmetric about the axial z direction in which laser light propagates. As a result, ignoring polarization effects, the optical trapping force along the y axis is almost identical to that along the x axis. Because of the lack of planar symmetry, however, the trapping force in the x direction is not invariant with respect to motion along the y axis. Therefore, when considering motion in a lateral plane, since the trapping force profile (3.2) is symmetric about the z-axis, it is convenient to use polar coordinates instead of Cartesian coordinates, as discussed in Section 3.3. In the remainder of this chapter, we will interpret the spatial coordinate x as representing radial position in the lateral plane from the center of the trap.

4.1 Spectra, Power, and Variance Conventions

Although power spectra and covariance functions are standard quantities used to analyze stochastic systems, their exact definitions vary in the literature. Therefore, to avoid ambiguity, we will clearly specify the relations between these quantities in accordance with [34]. The autocovariance function $r(t)$ of the second order, weakly stationary, scalar process $x(t)$ is defined as

$$r(t) = \mathrm{Cov}[x(t-\tau), x(\tau)] := E[x(t-\tau) - Ex(t-\tau)][x(\tau) - Ex(\tau)]. \tag{4.1}$$

[1] Some of the material in this chapter will appear in [33].

[34]. For continuous time, the double-sided spectral density is given by the integral

$$\phi(\omega) = \frac{1}{2\pi} \int_{-\infty}^{\infty} e^{-i\omega t} r(t) dt, \tag{4.2}$$

in which frequency ω is measured in radians per second [34]. It follows that the covariance function is given by the integral

$$r(t) = \int_{-\infty}^{\infty} e^{i\omega t} \phi(\omega) d\omega, \tag{4.3}$$

and we obtain the variance of x as

$$\mathrm{Var}(x) = r(0) = \int_{-\infty}^{\infty} \phi(\omega) d\omega, \tag{4.4}$$

which shows that the variance is given by the area under the spectral density function, which is a desired result of the definitions given by (4.1), (4.2), and (4.3) [34]. For this property of the variance to hold even when frequency f is measured in Hertz, we require that

$$\phi(\omega) d\omega = S(f) df, \tag{4.5}$$

where $S(f)$ is the double-sided power spectrum and $\omega = 2\pi f$. The correspondence between $\phi(\omega)$ and $S(f)$ is given by

$$\phi(\omega) = \frac{1}{2\pi} S(f), \tag{4.6}$$

which implies that the relation between the double-sided spectral density $\phi(\omega)$ and the single-sided (positively indexed) power spectrum $S^+(f) = 2S(f)$ (for positive frequencies) is

$$\phi(\omega) = \frac{1}{4\pi} S^+(f). \tag{4.7}$$

Combining (4.2) and (4.7), we obtain the relation

$$S^+(f) = 2 \int_{-\infty}^{\infty} e^{-i\omega t} r(t) dt. \tag{4.8}$$

White Noise

Denoting the Dirac delta function by $\delta(t)$, the covariance of a continuous time white noise process $e(t)$ is given by

$$r_e(t) = R_e \delta(t), \tag{4.9}$$

where R_e is a constant [34]. Clearly, the variance $r_e(0)$ of CT white noise is infinite [34]. We can combine (4.9) and (4.8) to obtain the relation

$$R_e = \frac{1}{2} S_e^+(f) = 2\pi \phi_e(\omega), \tag{4.10}$$

in which (4.7) was used to demonstrate consistency with [34]. Combining (4.10) and (3.10), the covariance $r_L(t)$ of the Langevin force is given by

$$r_L(t) = R_L \delta(t) = 2\beta k_B T \delta(t), \tag{4.11}$$

which shows that for a 1-μm bead trapped in water at room temperature,

$$\begin{aligned} R_L &\approx 2 \times 0.01 \ \frac{\text{pNs}}{\mu\text{m}} \times (4 \times 10^{-3} \ \text{pN}\mu\text{m}) \\ &= 8 \times 10^{-5} \ \mu\text{m}^2. \end{aligned}$$

For band-limited white noise, the spectral density $\phi_e(\omega)$ and power spectrum $S_e^+(f)$ are nonzero constants with finite frequency bands of $-\Omega < \omega < \Omega$ (rad/s) and $0 \leq F$ (Hz), respectively, where $F = \frac{\Omega}{2\pi}$. Therefore, the variance takes on a finite value

$$r_e(0) = 2\phi_e\Omega = S_e^+ F, \tag{4.12}$$

in which $\Omega = \pi$ implies 1 rad/s, or equivalently, $F = 0.5$ Hz. The spectral density and power spectrum conventions described in (4.12) are shown graphically in Figure 4.1.

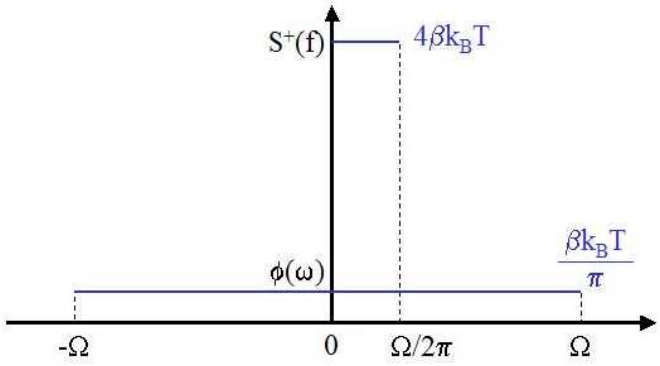

Figure 4.1: Spectral density and power spectrum for band-limited white noise. Listed Amplitudes correspond to the Langevin force.

4.2 Stochastic Differential Equation

Ignoring the external force F_E, the nonlinear noninertial state model (3.16) is given by

$$\begin{aligned} \dot{x} &= \rho \frac{\psi(x-u)}{\beta} \left[\alpha_3 (x-u)^3 - \alpha_1 (x-u)\right] + \frac{F_L}{\beta} \\ y &= x. \end{aligned} \tag{4.13}$$

Therefore, the open loop state model is given by

$$\begin{aligned} \dot{x} &= \rho \frac{\psi(x)}{\beta} \left[\alpha_3 x^3 - \alpha_1 x\right] + \frac{F_L}{\beta} \\ y &= x. \end{aligned} \tag{4.14}$$

Because it does not account for angular position θ, the state form (4.13) is not a complete state space description. For the purposes of this chapter, however, we are not concerned with angular position. Comparing with the standard state form

$$\dot{x} = f(x,t) + \sigma(x,t)e(t), \tag{4.15}$$

in which $e(t)$ is white noise with covariance $r_e(\tau) = \delta(\tau)$, and using (4.11), we see that $f(x,t) = f(x)$ and $\sigma(x,t) = \sigma$ are given by

$$\begin{aligned} f(x) &= \rho\frac{\psi(x)}{\beta}\big[\alpha_3 x^3 - \alpha_1 x\big] && (4.16)\\ \sigma^2 &= \frac{2k_BT}{\beta}. && (4.17)\end{aligned}$$

For a 1-μm bead trapped in water at room temperature, $\sigma^2 = 0.8\ \mu\text{m}^2$. We can also express (4.13) as a stochastic differential equation:

$$\begin{aligned} dx &= \rho\frac{\psi(x-u)}{\beta}\big[\alpha_3(x-u)^3 - \alpha_1(x-u)\big]dt + \frac{F_L}{\beta}dt\\ dy &= dx. && (4.18)\end{aligned}$$

Therefore, the open loop stochastic differential equation is given by

$$dx = \rho\frac{\psi(x)}{\beta}\big[\alpha_3 x^3 - \alpha_1 x\big]dt + \frac{F_L}{\beta}dt, \quad (4.19)$$

and comparing with the standard state form

$$dx = f(x,t)dt + \sigma(x,t)dw, \quad (4.20)$$

in which w is a Wiener process with incremental covariance dt, we see that $f(x)$ and σ are given by (4.16) and (4.17).

4.3 Probability Distribution

Defining $p = p(x,t;x_0,t_0)$ as the probability of being in state x at time t given that the particle is (initially) in state x_0 at time t_0, the conditional distribution p satisfies the Fokker-Planck equation (also known as the Kolmogorov forward equation) given by

$$\frac{\partial p}{\partial t} = -\frac{\partial}{\partial x}(pf) + \frac{1}{2}\frac{\partial^2}{\partial x^2}(\sigma^2 p), \quad (4.21)$$

where f and σ are defined according to the stochastic differential equation (4.20) [34]. The initial condition is specified as $p(x,t_0;x_0,t_0) = \delta(x - x_0)$.

4.3.1 Transient Analysis

The time-dependent Fokker-Planck equation (4.21) can be solved numerically, but we have not included the solution in this paper.

4.3.2 Steady State Analysis

By analyzing the probability distribution in steady-state, we can classify the nature of boundaries for a trapped particle. Substituting $\frac{\partial p}{\partial t} = 0$ into (4.21), we obtain:

$$\frac{\partial}{\partial x}(pf) = \frac{1}{2}\frac{\partial^2}{\partial x^2}(\sigma^2 p). \quad (4.22)$$

This can be integrated twice to obtain

$$\ln\left(\frac{p(x)}{p(0)}\right) = \frac{2}{\sigma^2}\int_0^x f(x)dx, \quad (4.23)$$

assuming $f(0) = 0$ and $\frac{dp}{dx}(x = 0) = 0$. The first assumption is satisfied according to (3.2), and we will subsequently see that the second assumption also holds. Denoting the integral in (4.23) as $I(x)$, we can use the expression for $f(x)$ from (4.17) to show that

$$I(x) = \begin{cases} \rho\frac{x^2}{4\beta}(\alpha_3 x^2 - 2\alpha_1) & \text{for } |x| < R = \sqrt{\frac{\alpha_1}{\alpha_3}} \\ -\rho\frac{\alpha_1^2}{4\beta\alpha_3} & \text{for } |x| \geq R, \end{cases} \tag{4.24}$$

which is shown graphically in the top plot of Figure 4.2 for $\rho = 1$. From (4.23), we see that

$$p(x) = p(0)e^{\frac{2}{\sigma^2}I(x)}, \tag{4.25}$$

which, combined with (4.24) and (4.17) gives

$$p(x) = \begin{cases} p(0)\exp\left[\rho\frac{x^2}{4k_BT}(\alpha_3 x^2 - 2\alpha_1)\right] & \text{for } |x| < R = \sqrt{\frac{\alpha_1}{\alpha_3}} \\ p(0)\exp\left[-\rho\frac{\alpha_1^2}{4k_BT\alpha_3}\right] & \text{for } |x| \geq R, \end{cases} \tag{4.26}$$

which is shown graphically in the bottom plot of Figure 4.2. Because the integral $I(x)$ is not

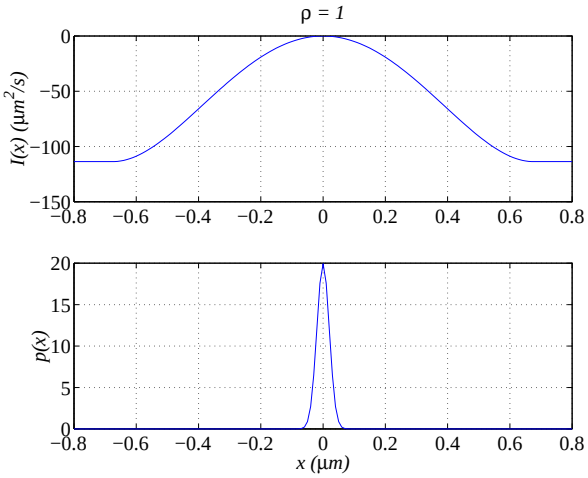

Figure 4.2: Normalized steady state probability distribution for $\rho = 1$, assuming finite absorbing boundaries at $x = \pm 50$ μm. In the bottom plot, the nonzero tails of the probability distributions are too small to be seen.

negatively unbounded outside of the trapping radius R, the probability density $p(x)$ has a small, but nonzero value for all positions outside of the trapping radius. In Figure 4.2, this nonzero tail is given by $p(x) \approx 8.3 \times 10^{-123}$. If we attempt to normalize $p(x)$ by imposing the condition

$$\int_{-\infty}^{\infty} p(x)dx = 1, \tag{4.27}$$

we find that $p(x)$ is zero for all x. In other words, in the absence of finite absorbing boundaries, the particle has a finite probability of being anywhere on the x-axis, which implies that, given enough time, particles will escape confinement by the trap and move in a Brownian fashion. In terms of classification of boundary conditions, this implies that a trapped particle has accessible boundaries at all locations in the lateral plane [35]. The normalized probability distribution

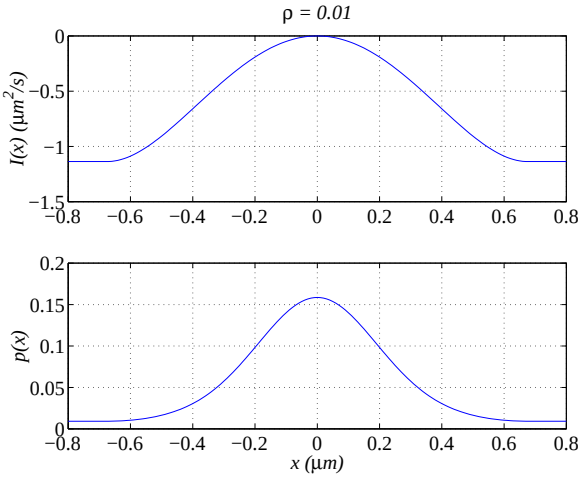

Figure 4.3: Normalized steady state probability distribution for $\rho = 0.01$, assuming finite absorbing boundaries at $x = \pm 50$ μm. The nonzero tails of the probability distributions are visible.

calculations are shown in Figure 4.3 for $\rho = 0.01$. At this reduced power level, the nonzero tails of the probability density are more pronounced, as seen in the bottom plot.

In practice, the fluid cell which contains trapped particles has lateral dimension of approximately 20 mm and the field of view is typically about 100 μm. Therefore, we can impose absorbing boundaries at $x = \pm 50$ μm, which has been done for the distributions shown in Figures 4.2 and 4.3.

4.4 First Exit Time

The performance of an optical trap can be characterized in several ways. Within the linear trapping regime, parameters such as trap stiffness and characteristic frequency are commonly used, whereas within the nonlinear (entire) trapping region, the maximum trapping force is often used [18, 26, 36]. In this section, we will investigate first exit times, which tell us how long a particle will remain within the optical trap. For a given optical tweezer configuration, the first exit time is an extremely useful measure of trapping capability because it quantifies the time horizon during which experiments can be conducted before trapped particles are lost. Although high-quality microscope objectives are capable of handling laser power levels of up to approximately 500 mW at the focus, typical optical tweezer experiments use much lower power levels [20]. It is especially important to use lower power levels when studying biological samples to avoid damaging them with heat, which is known as 'opticution' [20]. Furthermore, in applications in which the power from a single laser beam is shared by many traps, the power available for each trap can be very small; in this situation, it is useful to understand and quantify the lowest power levels that are capable of providing sufficiently strong traps.

In Section 4.3.2, we showed that, in theory, given enough time, a trapped particle will travel beyond the trapping radius R and escape the confinement of the trap. [35]. Therefore, we can define the first passage time T as the random variable

$$T = T(x_0, r_1, r_2) := \sup\{t | X(\tau) \in (r_1, r_2), \quad 0 \leq \tau \leq t\}, \tag{4.28}$$

where $X(\tau)$ is the random variable corresponding to particle position x with initial condition

$X(0) = x_0$. According to (3.2), if we set $r_1 = -R$ and $r_2 = R$ in (4.28), we can define the first exit time T_1 as

$$T_1 := T(x_0, -R, R) = \sup\{t | X(\tau) \in (-R, R), \quad 0 \leq \tau \leq t\}. \tag{4.29}$$

In theory, it is possible for a particle to escape from the trap and wander back into it as a result of Brownian motion. Therefore, the 'exit times' described in this section are not synonymous with 'escape times'; according to our model, a particle never truly escapes from the trap unless it hits an absorbing boundary.

4.4.1 Exit Time Distribution

If we define $g = g(t; x_0, -R, R)$ as the probability density function of the first exit time $T(x_0, -R, R)$, we can use results from [35] to show that the Laplace transform $G = G(s; x_0, -R, R)$ is given by the expression

$$G(s; x_0, -R, R) = \frac{\epsilon_2(x_0)[\epsilon_1(R) - \epsilon_2(-R)] - \epsilon_1(x_0)[\epsilon_2(R) - \epsilon_2(-R)]}{\epsilon_1(R)\epsilon_2(-R) - \epsilon_1(-R)\epsilon_2(R)}, \tag{4.30}$$

where $\epsilon_1(x)$ and $\epsilon_2(x)$ are any two linearly independent solutions of the ordinary differential equation

$$\frac{k_B T}{\beta}\frac{d^2\epsilon}{dx^2} + \rho\frac{(\alpha_3 x^3 - \alpha_1 x)}{\beta}\frac{d\epsilon}{dx} - s\epsilon = 0. \tag{4.31}$$

Obtaining the above density function g of the first exit time requires tedious calculations that are unnecessary for the purposes of this section. To simplify our analysis, we will investigate the mean first exit time, which can be obtained using much simpler calculations.

4.4.2 Mean Exit Time

For our system, the mean exit time $m_1 := E\{T_1\}$ is given by the homogeneous linear second order ordinary differential equation

$$\frac{1}{2}\sigma^2\frac{d^2 m_1}{dx_0^2} + f(x_0)\frac{dm_1}{dx_0} = -1, \tag{4.32}$$

with two-point boundary conditions, $m_1(-R) = m_1(R) = 0$ [37]. Substituting σ and f from (4.17), we obtain

$$\frac{k_B T}{\beta}\frac{d^2 m_1}{dx_0^2} + \rho\frac{(\alpha_3 x_0^3 - \alpha_1 x_0)}{\beta}\frac{dm_1}{dx_0} + 1 = 0, \tag{4.33}$$

which can be solved numerically. The mean exit time for $\rho = 1$ (100 mW) is bounded, but extremely large, with a maximum in the vicinity of over 10^{100} trillion years, for $x_0 = 0$. This length of time is unbounded for all practical purposes! As shown in Figure 4.4, reducing the power to $\rho = 0.01$ (1 mW) drastically reduces the mean exit time such that its maximum is approximately 2.51 s at $x_0 = 0$. For comparison, the mean exit time for $\rho = 0$ is 0.57 s, which corresponds to free diffusion of an untrapped particle due to Brownian motion.

Figure 4.5 shows the maximum mean exit time $m_1(0)$ as a function of the laser power factor ρ for $\rho \leq 0.1$ (10 mW). The solid line pertains to a 1-μm diameter polystyrene bead in water at biological temperature ($\sigma^2 = 0.8$ μm^2; $\beta = 0.01$ pNs/μm). For comparison, three other combinations of σ^2 and β have also been plotted. The maximum mean exit time (solid line) for

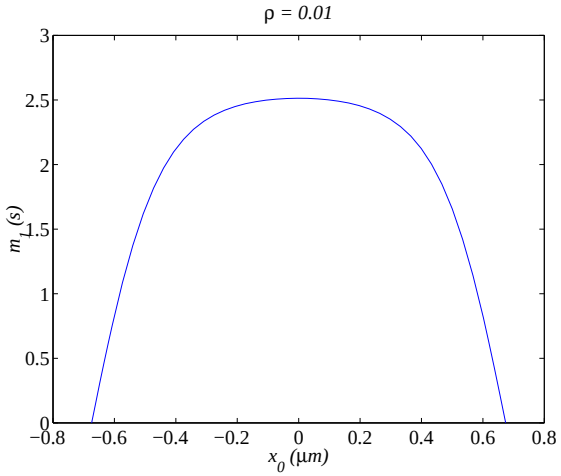

Figure 4.4: Mean exit time for $\rho = 0.01$. Maximum is $m_1(0) = 2.51$ s.

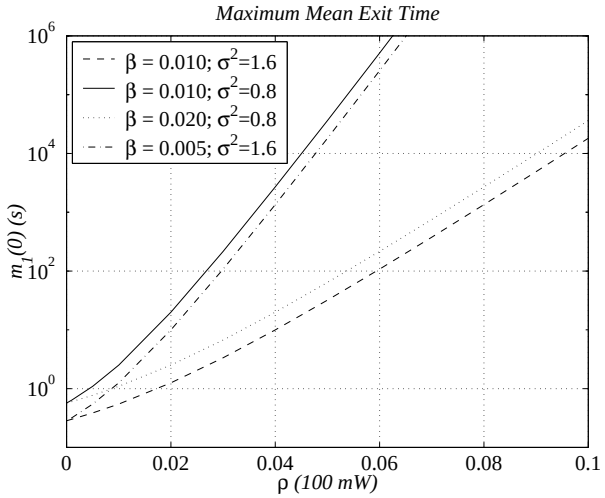

Figure 4.5: Maximum mean exit time as a function of laser power factor. The mean exit time increases exponentially with laser power.

$\rho = 0.05$ (5 mW) is 3.63×10^4 s, or about 10 hours, which is more than sufficient for present-day optical tweezer experiments. (Due to factors such as drift and cross-contamination, many biological experiments are conducted for not more than a few minutes at a stretch [26, 11]).

According to Figure 4.5, the maximum mean exit time for $\rho = 0$ appears to be directly proportional to σ^2. That is, with reference to (7.21),

$$[m_1(0)]_{\rho=0} \propto \sigma^2 \propto \frac{k_B T}{\beta}. \tag{4.34}$$

Furthermore, for a given value of ρ, the rate of change of the logarithm of the maximum mean exit time (with respect to ρ) appears to be inversely proportional to $\sigma^2\beta$. That is, with reference

to (7.21),

$$\left[\frac{d\log m_1(0)}{d\rho}\right]_{\rho \text{ const.}} \propto \frac{1}{\sigma^2\beta} \propto \frac{1}{k_B T}. \tag{4.35}$$

Figure 4.6 shows the maximum mean exit time $m_1(0)$ from the linear region $R_l = 0.2$ μm as a function of the laser power factor.

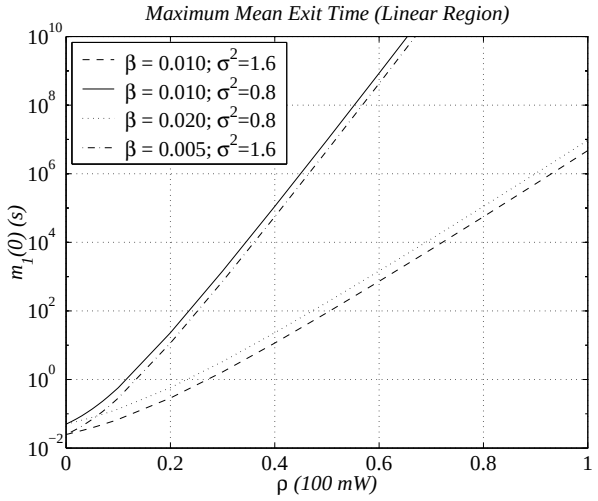

Figure 4.6: Maximum mean exit time from the linear region (±200 nm) as a function of laser power factor.

4.4.3 Experimental Results

Verifying the theoretical mean exit time results from Section 4.4.2 is difficult for a number of reasons:

1. Typical position detection systems, such as a photodetector circuit, are ineffective or inaccurate beyond the linear trapping region. As a result, real-time position detection at the outskirts of the trapping radius usually requires a real-time imaging system with very high spatial and temporal resolution. Such a system is not available in our laboratory.

2. Once a particle escapes the trap, it will often drift away. To obtain enough measurements of the exit time to make statistically meaningful statements, we would require a system that automatically captures particles and measures their exit times. The alternative would be to manually trap and measure mean exit times, but his is inaccurate and labor intensive.

3. The lateral mean exit time calculations do not account for the fact that the particle might escape in the axial direction. A thorough experimental verification of exit times would require an accurate model of the axial trapping force, which is not currently available.

However, we can compute the mean passage time for particles within the linear region quite easily by detecting zero crossings and subsequent excursions outside of the radius r of interest. Figure 4.7 shows how the mean exit time can be calculated for a 9.61-μm bead starting at the origin. The position data shown is the same data used in Figure 7.1.

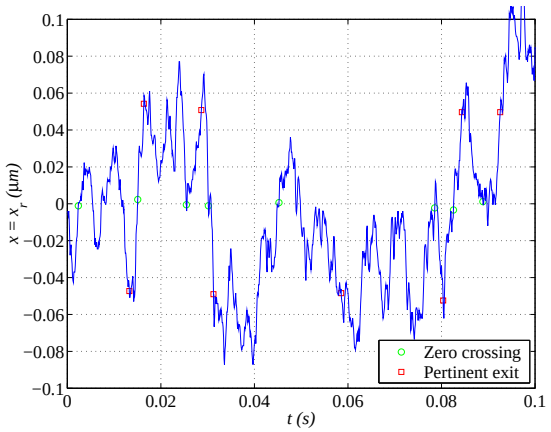

Figure 4.7: Calculation of maximum mean exit time from $x_r = \pm 0.05$ μm for a 9.61-μm polystyrene bead. Green stars depict pertinent zero crossings; Red squares depict pertinent excursions outside of $x_r = \pm 0.05$ μm. Experimental data was sampled at 10 kHz for a total of 30 seconds.

Figure 4.8 shows the calculated mean exit times for a 9.6-μm diameter bead in a Phosphate-Buffered Saline (PBS) solution, which is used to prevent beads from clumping together. For comparison, theoretical values for $\alpha_1 = 1.81$ pN/μm and $\beta = 0.015$ pNs/μm are also shown. (We assume $\alpha_3 = 0$ within the linear trapping region.) These stiffness and drag values were obtained from the power spectrum calibration in Section 7.2. Clearly, the theoretical and experimental values are in close agreement. The slight discrepancies for low and high values of r are most likely due to unmodeled nonlinearities in the position detector response; furthermore, experimental mean passage times for low r are artificially inflated due to quantization errors.

Although the experimental results in this section pertain to a bead that is much larger than the 1-μm bead studied in the previous sections, the results apply to beads of any size, as long as they remain within the linear region. If we considered the entire nonlinear trapping region, the cubic model (3.2) would have to be re-scaled; it is unclear how the nonlinear force model should be modified to accurately account for larger beads.

4.5 Discussion

In this section, we applied the Fokker-Planck equation to analyze the stochastic behavior of a spherical particle trapped in an optical tweezer. In theory, given enough time, a trapped particle will escape confinement from the trap. In general, we observe that the calculated maximum mean exit time with no trapping force ($\rho = 0$) is directly proportional to $\frac{T}{\beta}$. Furthermore, the rate of change of the logarithm of the (calculated) maximum mean exit time for a particular value of ρ is inversely proportional to absolute temperature T.

We obtained specific results for a 1-μm diameter polystyrene bead trapped in water at biological temperature. In particular, for laser powers of greater than approximately 5 mW at the focus, the mean first escape time is extremely large, and unbounded for all practical purposes. In effect, a trapped particle will not escape. With no laser power (i.e., in the absence of an optical trap), the particle moves in a Brownian manner, which has a maximum mean escape time in the radial x direction of just under 0.6 s. We show that the maximum mean exit time increases exponentially with laser power. In particular, for laser power greater than 20 mW, the mean exit time in the radial x direction increases by approximately 1.2 orders of

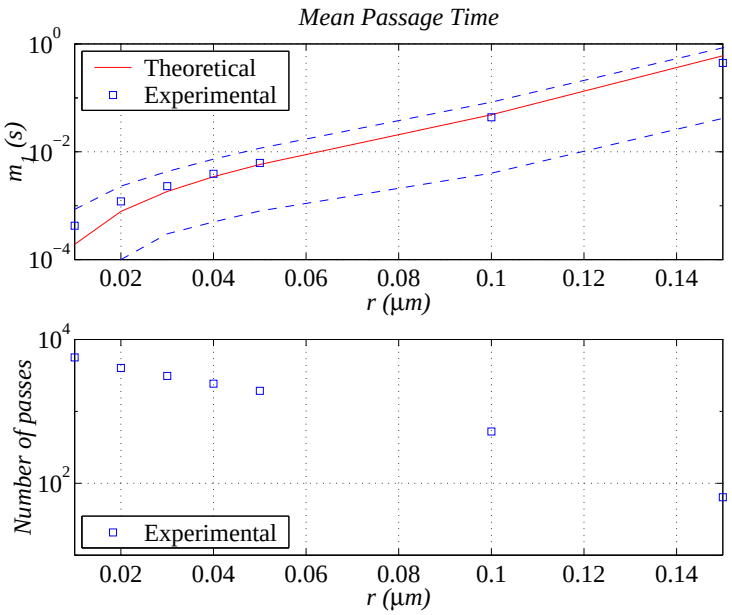

Figure 4.8: Maximum mean exit time within the linear region for a 9.6-μm polystyrene bead. Top plot shows measured mean exit time, including measured standard deviation bounds (dashed lines); bottom plot shows number of pertinent crossings outside of the radius of interest. Theoretical values assume $\alpha = 1.81$ pN/μm and $\beta = 0.015$ pNs/μm; experimental data was sampled at 10 kHz for a total of 30 seconds.

magnitude for each additional milliwatt of laser power.

We also measure the mean exit (passage) time and standard deviations of a 9.6-μm bead within the linear trapping region. Experimental results are in close agreement with theoretical results. Because the mean exit time is very sensitive to the values of α and β, the measured mean exit times can be used to experimentally verify the accuracy of calibration results obtained from other calibration methods, such as the power spectrum. This will be discussed in greater detail in Chapter 7.

As mentioned in Section 3.2, an optical tweezer traps particles in three dimensions. The axial trapping force directed towards the microscope objective (in the z direction), will be weaker than the lateral trapping force. Consequently, in a three-dimensional optical trap, a trapped particle is more likely to escape in the axial direction away from the microscope objective (in the direction of laser light propagation) than in any other direction. Therefore, if we consider all three spatial dimensions, the actual mean escape times will likely be less than that for just the lateral plane considered in this chapter. In the absence of an experimentally verified trapping force model for the axial z direction, we will not attempt to calculate 3-dimensional exit times in this chapter. Instead, we will assume trapped particles have been sufficiently[2] stabilized in the axial z direction that they do not escape. In practice, axial stabilization (within measurement error) can be achieved using feedback with appropriate sensors and actuators [10, 18].

By casting our system as a stochastic differential equation and using a lateral nonlinear trapping force model of an optical trap, we have developed a framework for studying the stochastic behavior of trapped particles in the lateral plane. This has enabled us to study the mean first

[2]The feedback gain should be high enough to restrict the particle within the trapping radius, but not so high that instability is induced.

exit time, which is a useful measure of the trapping capability of an optical tweezer. Although our results apply specifically to (commonly used) 1-μm diameter polystyrene beads trapped in water using a 1.25 NA microscope objective, the methods used in this chapter are applicable to a wide variety of optical tweezer systems, once appropriate adjustments have been made to account for different trapping force profiles (F), particle sizes (r), fluid properties (β), and temperature (T).

Chapter 5

Construction of Optical Tweezers

This section describes construction of our optical tweezers. The structure is loosely based on the optical tweezers constructed by Stephen Quake and Chris Meiners at Caltech[1]. Instead of directing a laser into an existing microscope, a home-made inverted microscope was built. This provides greater flexibility with the positioning of various optical components that are mounted on a $3' \times 4'$ optical table. A general view of the optical components in our system is shown in Figure 5.1.

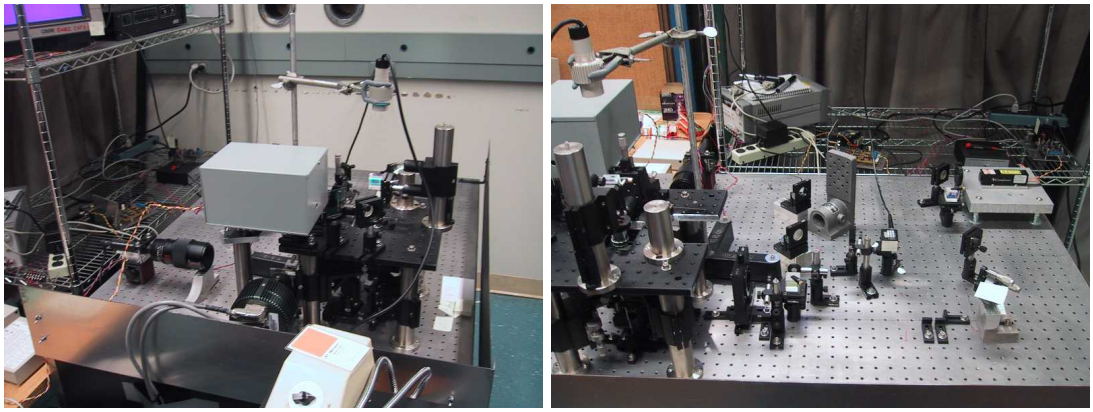

Figure 5.1: General view of optical components from left and front.

Appendix B contains detailed information about construction of the optical tweezers. Procedures for the systematic alignment of the various optical components can be found in [12, 9, 38]. Sterba and Sheetz describe how optical tweezers can be incorporated into an existing inverted microscope (if necessary) [9].

5.1 Trapping System

A horizontal two-axis platform translation stage (Model 406, Newport) is used to hold and translate trapped specimens. The stage can be moved independently in both the x and y directions using manual micrometers (Model SM-13, Newport) that have a range of 13 mm and a vernier resolution of 1 μm. The traps are created using a 100×/1.3 NA oil immersion

[1]Patricia Swift and I visited Quake's laboratory at Caltech in December 1999.

microscope objective (Plan Neofluar, Zeiss) that has a conjugate plane at infinity and a working distance of 200 μm. The microscope objective is inserted through the circular aperture of the translation stage. Two views of our sample translation stage are shown in Figure 5.2.

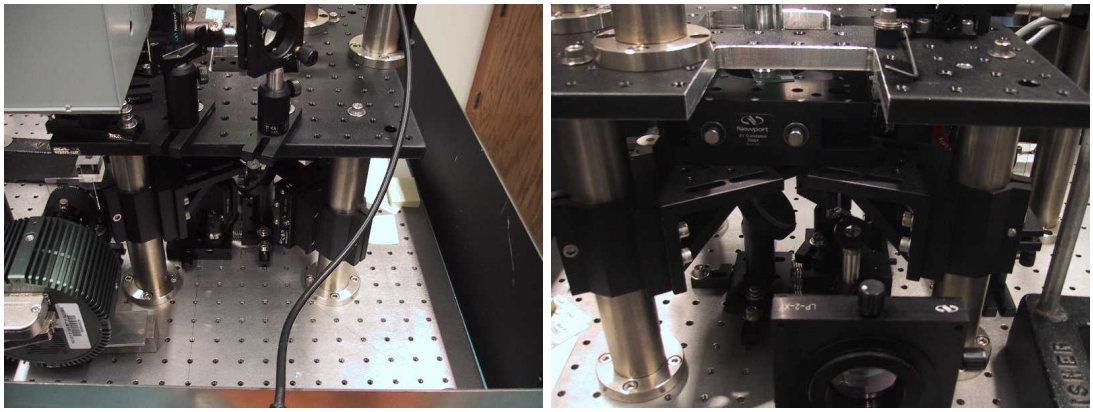

Figure 5.2: View of sample translation stage from left and right.

As shown in Figure 5.3, specimens for trapping are contained within a fluid cell that consists of a square cover glass (thickness $\sim 170\mu$m) stuck to a standard microscope cover slip using double-stick tape spacers (thickness $\sim 75\mu$m).

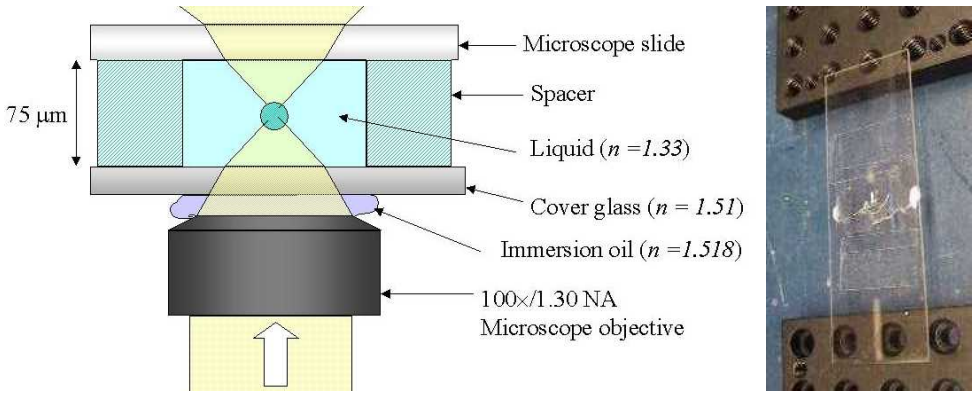

Figure 5.3: Schematic diagram of Trapping cell. Left figure shows the configuration used to achieve trapping; right figure shows top view of a typical trapping cell (rotated 90°).

The trapping laser shown in Figure 5.4 is a horizontally polarized continuous wave (CW) diode-pumped infrared Nd:YAG laser (Model IRCL-700-1064, Crystalaser) with a wavelength of $\lambda = 1.064$ μm. It has a manually adjustable power range of $P_\lambda = 370$–760 mW and an output beam diameter of $d_\lambda = 1.2$ mm.

For a given laser, the trap will be strongest when the diameter of the incoming laser beam at the objective $d_{\lambda\mu}$, is slightly larger than the diameter of the microscope objective entrance aperture, d_μ [12]. The diameter of the objective entrance aperture d_μ is given by the formula[2]

[2]Unless indicated otherwise, all formulas are in SI units.

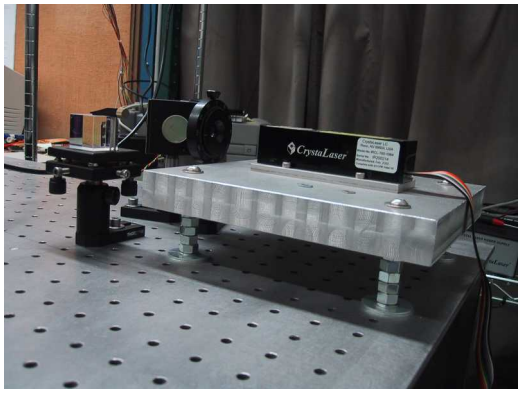

Figure 5.4: View of laser, waveplate, and polarizing beam-splitting cube.

$$d_\mu = 2N_A f_\mu = 2N_A \left(\frac{0.164}{M_\mu} \right), \tag{5.1}$$

where f_μ is the effective focal length of the microscope objective and M_μ is the magnification of the objective [39]. For our trapping objective, $N_A = 1.30$ and $M_\mu = 100$, which implies that

$$f_\mu = 1.64 \text{ mm}$$

and

$$d_\mu = 4.264 \text{ mm}.$$

As shown in Section 5.3, plano-convex lenses are used to expand the laser beam from 1.2 mm to slightly larger than d_μ.

The microscope objective can be moved vertically using a manual micrometer and translation stage (Model 423, Newport). For a trap arising due to a normally incident, collimated laser beam, if the microscope objective is moved axially (vertically) by some distance Δz_μ, the vertical distance that the laser focus (the trap) is moved within the fluid cell is given by

$$\Delta z_T = \left(\frac{n_f}{n_o} \right) \Delta z_\mu, \tag{5.2}$$

where $\frac{n_f}{n_o}$ is the ratio of the refractive index of the fluid suspension medium ($n_f \sim 1.33$ for water) to the refraction index of the immersion oil ($n_o \sim 1.158$) [15]. Therefore, for our system,

$$\Delta z_T = 1.15 \Delta z_\mu. \tag{5.3}$$

For instances in which the trapping laser beam does not enter the objective perpendicularly (i.e., when the trap has been moved laterally), moving the microscope objective is not a recommended method for achieving axial trap movement because the steering consistency requirements will be violated and the trap may become weak and ineffective. This problem can be avoided by employing the steering scheme described in Section D.1.1 for axial steering.

5.2 Viewing System

The same microscope objective used to create the trap is also used to view particles within the trap. The disadvantage of building ones own microscope is the need to construct an imaging system, but this was done without too much difficulty. Since room lighting is barely adequate for clear viewing of trapped particles, additional illumination is provided by a portable light source (Nikon). Because the illuminating light is not focused, it has a negligible effect on trap performance. Images of particles within the trapping plane are viewed by focusing the viewing light onto an analog CCD camera array. Signals from the CCD color video camera (Model XC-999, Sony) are sent to a videocassette recorder for recording (if necessary) and to a 13"-color video monitor for viewing.

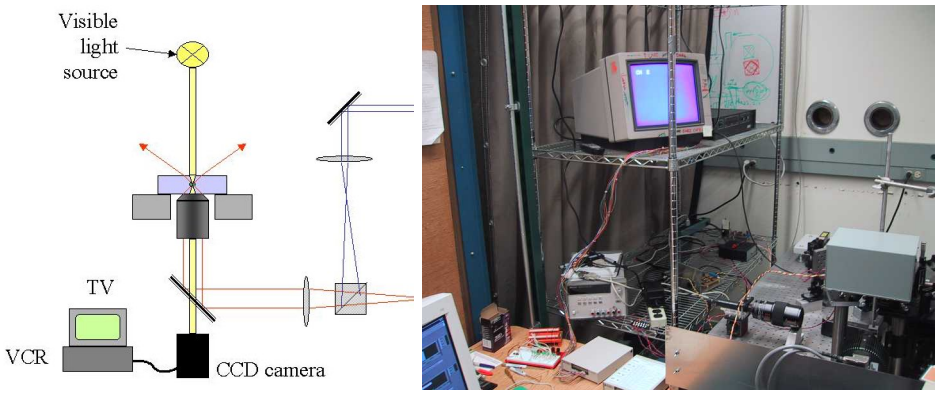

Figure 5.5: Video viewing system.

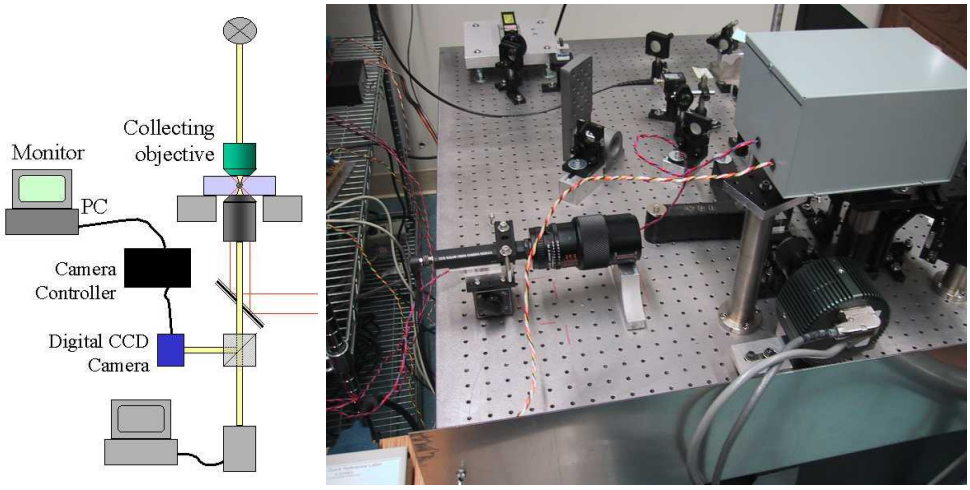

Figure 5.6: Digital viewing system. Left figure shows schematic diagram of the digital viewing system and right figure shows both video and digital cameras. Digital camera controller and PC are shown in Figure 5.16.

For calibration and recording purposes, it is very convenient to view and save particle images using a digital camera. As shown in Figure 5.6, a broad-band cube beamsplitter (Model 44-

3663, Coherent) is used to split the the imaging light such that 45% of the light is transmitted towards the analog CCD camera described above and 45% of the light is reflected to a digital CCD camera (MicroMAX:1300YHS, Princeton Instruments). Images collected by this digital camera are sent to a PC (Pentium II processor) via a digital camera controller (MicroMAX 5MHz, Princeton Instruments). The digital images are viewed on a large 17" computer monitor. The PC is equipped with sophisticated image processing software (Imaging Workbench 2.2, Axon Instruments) for real-time data collection and mostly off-line data analysis. Even if image-processing software is used, however, the resolving power of an optical imaging system is limited by diffraction to 200–300 nm [40].

A digital image of a 10 μm polystyrene bead that was trapped using our optical tweezers is shown in Figure 1.4. For that particular image, the laser output was set at approximately half power, all of which was used to create a horizontally polarized trap.

5.3 Lateral Steering System

The steering system for our dual-trap optical tweezer is based on a design suggested by Fallman and Axner [21]. The arrangement of optical components is shown in Figure 5.7.

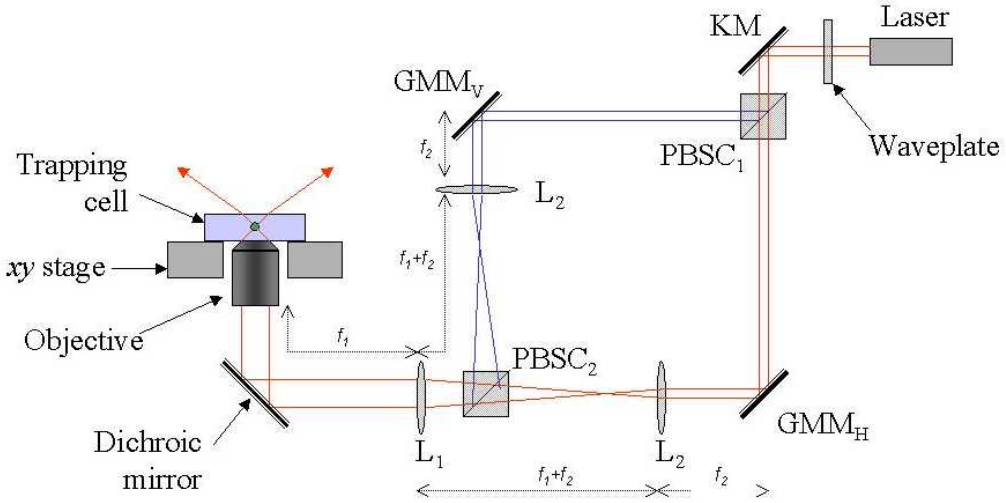

Figure 5.7: Lateral steering using mirrors.

Dual traps are created by splitting the incoming laser beam into two separate components according to polarization. This is done using a polarizing beam-splitting cube $PBSC_1$ which splits the beam into two orthogonally polarized components that are later recombined using another cube $PBSC_2$. The cubes are designed to transmit horizontally polarized (p-plane) light and reflect vertically polarized (s-plane) light (both at $\lambda = 1064$ nm). For the split to occur (i.e., for the creation of two traps), the laser beam needs to be polarized in both the horizontal (parallel to optical table) and vertical (perpendicular to optical table) directions. Since our laser has an output that is horizontally polarized, vertical polarization was induced by inserting a waveplate just after the laser output aperture. By manually rotating the waveplate, the direction of polarization can be rotated (continuously) as desired. This allows the laser power to be divided between each separate path according to a manually adjustable ratio. Two gimbal-mounted mirrors, GMM_H and GMM_V, can be used to independently deflect each beam

component about two orthogonal axes. Therefore, each trap can be steered independently in the x and y directions. Since the two traps are formed by beams with orthogonal polarization, "there is little interference when they are brought into close proximity, although residual interference can occur, due to depolarizing effects arising from the use of high-numerical aperture optics"[3] [18].

For both beam paths, lens L_1 (with focal length f_1) and lens L_2 are chosen and positioned to guarantee that the steering consistency requirements from Section 3.6 are met. Lenses L_1 and L_2 are placed at a distance f_1+f_2 apart such that they form a telescope that expands the laser beam by the ratio $\frac{f_1}{f_2}$. Lens L_1 is placed at a distance f_1 from the objective entrance aperture, while L_2 is placed at a distance f_2 from the gimbal-mounted mirror. According to geometric optics, the relationship between the diameter of the laser beam at the objective entrance aperture, $d_{\lambda\mu}$, and the diameter of the incoming laser beam, d_λ, is

$$d_{\lambda\mu} = \frac{f_1}{f_2} d_\lambda. \tag{5.4}$$

The lateral (horizontal) motion of the trap in the x direction, Δx_T, is related to the angular deflection of the gimbal-mounted mirror, $\Delta\theta_G$ according to

$$\Delta x_T = -2 f_\mu \frac{f_2}{f_1} \Delta\theta_G, \tag{5.5}$$

where f_μ is the effective focal length of the microscope objective. For our system, $d_\lambda = 1.2$ mm, $f_1 = 300$ mm, $f_2 = 75.6$ mm, and $f_E = 1.64$ mm. Therefore, $d_{\lambda\mu} = 4.762$ mm and

$$\underbrace{\Delta x_T}_{\mu\text{m}} = -0.8265 \underbrace{\Delta\theta_G}_{\text{mrad}}, \tag{5.6}$$

where Δx_T is in microns and $\Delta\theta_G$ is in milliradians. The motion of the trap in the y direction is analogous.

5.3.1 Motorization

For many experiments, at least one of the optical traps must be moved in a very specific, controlled manner. To this end, the gimbal-mounted mirrors can be equipped with motorized actuators. Of the two gimbal-mounted mirrors shown in Figure 5.7, only the mirror GMM_H (Model U100-G, Newport) that steers the horizontally polarized laser component is designed to be equipped with motors. Motors can be conveniently manipulated using a joystick, computer keyboard, or mouse. Motors are also needed for the smooth, controlled lateral movement of the sample translation stage. Two closed-loop DC motor actuators with non-rotating spindles were purchased from Polytec PI. They can be used as a direct substitute for the manual micrometers on both the gimbal-mounted mirror GMM_H and the sample translation stage. Selected specifications for each motor are listed in Table 5.1.

The motors are driven by a 2-channel DC motor controller board (Model C-842.20, Polytec PI) with an ISA bus interface. The controller board provides PID control of the DC motors through a Windows NT-based *LabVIEW* software interface.

5.3.2 Acousto-Optic Deflection

For experiments in which the laser beam needs to be moved very quickly, motorized actuators are too slow because of their limited mechanical bandwidth. Instead, extremely fast beam deflections

[3] To reduce polarization cross talk and interference effects, Meiners and Quake chopped the two orthogonally polarized trapping beams alternately at a frequency of 100 kHz [41].

DC Motor Parameter	Model M-230.10	Model M-222.50
Travel Range	10 mm	10 mm
Design Resolution	4.6 nm/count	8.4 nm/count
Min. Incremental Motion	50 nm	50 nm
Unidirectional Repeatability	0.1 μm	0.1 μm
Backlash	2 μm	2 μm
Max. Velocity	1.5 mm/s	1.5 mm/s
Optical Encoder Resolution	2048 counts/rev	2000 counts/rev
Transmission Ratio	219.7504 counts/μm	118.5679 counts/μm

Table 5.1: DC motor specifications [42].

can be achieved by passing the laser beam through an acousto-optic deflector (AOD). In an AOD, beam deflection is achieved by sending the laser through a density grating in a crystal created by a traveling acoustic wave at ultrasound frequencies as shown in Figure 5.8.

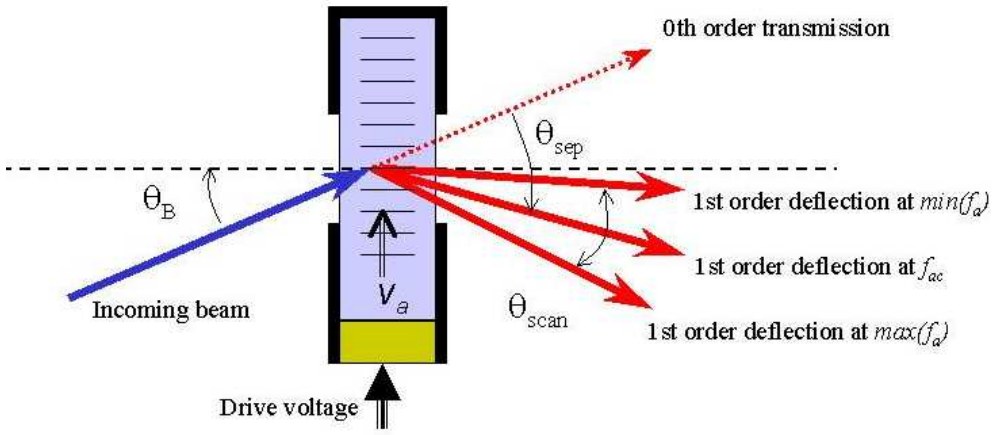

Figure 5.8: Beam deflection using an acousto-optic deflector. Incoming beam has been angled to achieve maximum first order deflection efficiency at center frequency.

The deflection angle θ_1 for first-order[4] light is given by

$$\theta_1 = \frac{\lambda f_a}{v_a}, \tag{5.7}$$

where λ is the laser wavelength, f_a is the acoustic wave frequency and v_a is the velocity of the sound wave [18]. Since the sound wave is constant for a given crystal, the deflection angle for monochromatic light is proportional to the acoustic frequency:

$$\theta_1 \propto f_a$$

From (5.7), for an AOD with a maximum and minimum acoustic frequency of $(f_a)_{\max}$ and

[4]Technically, the 1st order deflection shown in Figure 5.8 is the -1st order deflection, but this detail will be ignored.

$(f_a)_{\min}$ respectively, the maximum scan angle θ_{scan} is given by

$$\theta_{\text{scan}} = \frac{\lambda\left[(f_a)_{\max} - (f_a)_{\min}\right]}{v_a}. \tag{5.8}$$

For a given acoustic frequency f_a, first order deflection efficiency $\eta_1(f_a)$ is theoretically maximized when the incident angle θ_i of the laser beam is equal to the Bragg angle $\theta_B(f_a)$,

$$\lim_{\eta_1(f_a)\to(\eta_1(f_a))_{\max}} \theta_i = \theta_B(f_a) = \frac{\lambda f_a}{2v_a}, \tag{5.9}$$

which implies that, for any given incident angle θ_i, the first order efficiency will be maximized at a specific frequency [43]. Therefore, for fixed θ_i, deflection efficiency will change as the frequency is varied. The maximum possible first order efficiency $(\eta_1)_{\max}$ is achieved at the center frequency f_{ac} of the acoustic range:

$$\lim_{\eta_1\to(\eta_1)_{\max}} \theta_i = \theta_B = \frac{\lambda f_{ac}}{2v_a}, \tag{5.10}$$

where $\theta_B := \theta_B(f_{ac})$. The separation angle θ_{sep} is defined as the angle between the incident laser beam from (5.10) and the first order deflection beam from (5.7) when efficiency is maximized:

$$\theta_{sep} = 2\theta_B = \frac{\lambda f_{ac}}{v_a}. \tag{5.11}$$

Our optical tweezers system is equipped with one single-axis AOD (Model N45035-3-6.5DEG-1.06, NEOS Technologies) that uses TeO_2 as its crystal interaction material. The (slow) shear axis TeO_2 has an acoustic velocity of $v_a = 660$ m/s [44]. Selected AOD specifications are listed in Table 5.2. According to (5.6), the scan angle specified in Table 5.2 suggests that the AOD can be used to deflect the trap by a maximum lateral distance of 26.45 μm.

AOD Parameter	Specification
Center Frequency f_{ac}	35 MHz
Acoustic Frequency Range, $(f_a)_{\min}$ to $(f_a)_{\max}$	25–45 MHz
Intensity Variation	< 2 dB
Maximum 1st Order Diffraction Efficiency, $\max(\eta_1)$	65%
Scan Angle θ_{scan}	32 mrad $\approx 1.8^o$
Separation Angle θ_{sep}	56 mrad $\approx 3.2^o$
Input Light Polarization	linear, $\parallel \vec{v_a}$
Output Light Polarization	linear, $\perp \vec{v_a}$
0th Order Transmission Efficiency η_0 at $f_a = 0$	95%

Table 5.2: Acousto-optic deflector specifications [44].

The acoustic frequency is generated using a 32-bit digital frequency synthesizer driver (Model 64020-200-2ASDFS, NEOS Technologies) which is capable of generating a frequency range of 20-200 MHz with a resolution (minimum step size) of < 1 Hz. The intensity of the deflected beam can be modulated if necessary using a 0–1 V analog voltage signal. The acoustic frequency can be specified manually or using computer input. Although the response time of an AOD is intrinsically limited by the ratio of the acoustic velocity to the incident laser beam diameter: $\tau_a = d_\lambda/v_a$, the actual bandwidth will be considerably less due to delays in the computer interface [18].

Unlike the gimbal-mounted mirrors from Figure 5.7 which deflect the laser beam by $\sim 90^o$, the AOD deflects the beam by $\sim \theta_{sep} = 3.2^o$. Furthermore, Table 5.2 indicates that the AOD causes the polarization state of the laser beam to rotate by 90^o. Therefore, the AOD cannot be used as a direct substitute for a mirror. Instead, the AOD can be positioned as shown in Figure 5.9 and Figure 5.10. In Figure 5.9, GMM_V is replaced by the AOD, while a $\lambda/2$ waveplate is inserted prior to $PBSC_2$ to convert the AOD output beam polarization from horizontal to vertical. In this configuration, the AOD can be used to steer the vertically polarized trap in one direction, while GMM_H can be independently used to steer the horizontally polarized trap in the lateral plane as before. In Figure 5.10, only one trap exists because the AOD output polarization is not changed by a waveplate and therefore, GMM_H cannot be used simultaneously.

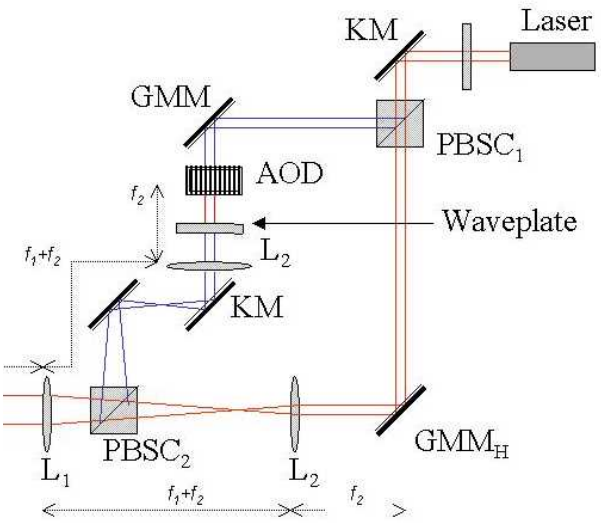

Figure 5.9: Lateral steering using an AOD with polarization correction. This arrangement provides two independent trapping beams, but requires an extra waveplate.

AOD Calibration details can be found in Section 6.3.

5.4 Position Detection System

Sensitive position detectors can be used to make quantitative measurements of nanometer displacements and piconewton forces with millisecond resolution [10]. The most common method of detecting a trapped particle's position is to image the particle onto a quadrant photodiode, after magnification by a microscope objective. The particle can be imaged using a light source independent of the trapping laser, or the particle can be imaged using the trapping laser itself. Although the former method is better suited for feedback-enhanced or time-shared schemes, its bandwidth is noise-limited to less than 1 kHz [18]. For larger temporal bandwidths (up to 100 kHz), the trapping laser itself should be used to image the particle [45].

The trap position detectors are mounted on a $12'' \times 12''$ aluminum breadboard located above the specimen stage. A rectangular aperture was machined through the center of the breadboard such that imaging light can pass through. A compact three-axis stage (Model 460-XYZ, Newport) is used to manually position a $20\times/0.4$ NA microscope objective (LD Achroplan, Zeiss) through the breadboard and directly above the specimen. Since this low-NA microscope objective collects the laser beam after it has passed through the trapping region, it is known

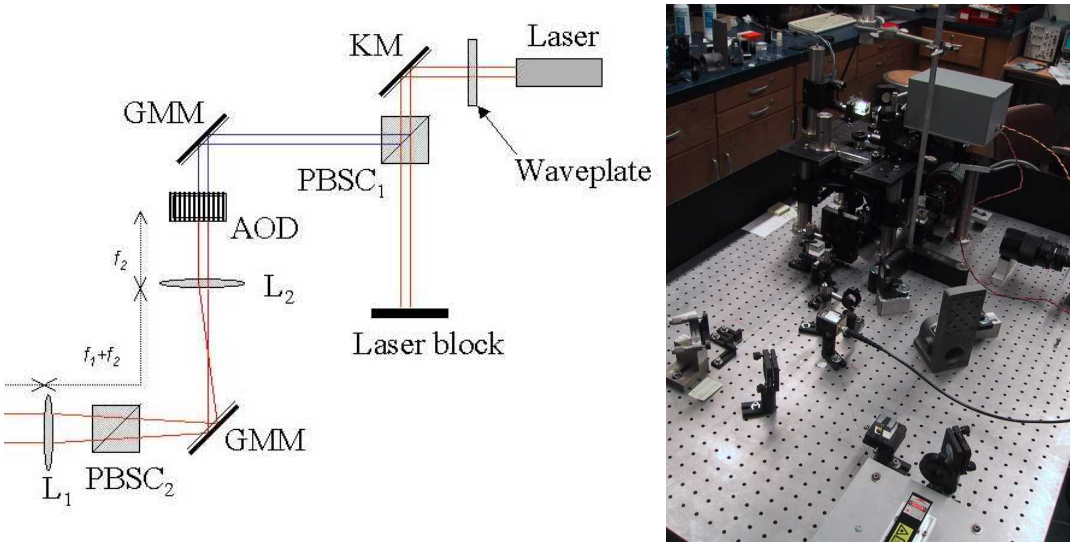

Figure 5.10: Lateral steering using an AOD without polarization correction. This arrangement provides only one trapping beam.

as the "collecting objective". The laser beams collected by the collecting objective are used for position detection. Above the specimen plane, a third polarizing beam-splitting cube ($PBSC_3$) is used to deflect the two orthogonally polarized detection beams into separate paths so that the position of particles in the two traps can be measured independently (Figure 5.11).

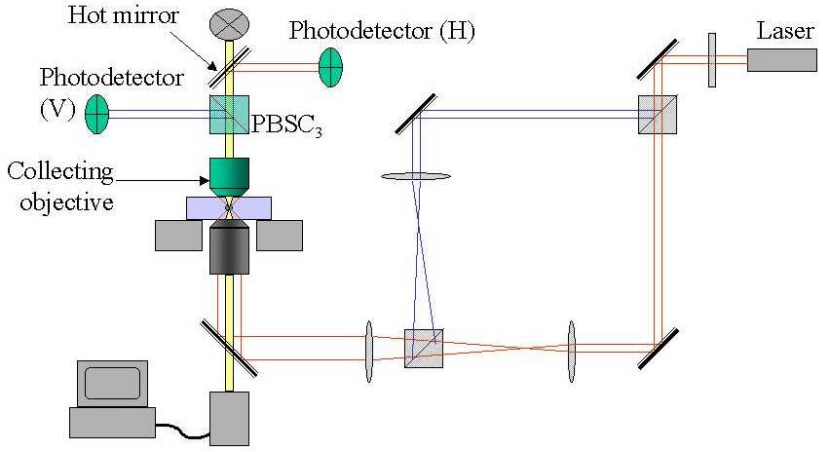

Figure 5.11: Bead position detectors.

Photographs of our position detection system are shown in Figure 5.12.

The photodetector circuit was designed by Patricia Swift according to manufacturer recommendations [46, 47]. Incoming laser light is detected using four-element segmented photodiodes. When light hits each segment, a current proportional to the incident light power is generated. The current output from each segment of the photodiode is converted to a voltage using low-noise precision operation amplifiers. As shown in Figure 5.13, these voltages are then appropriately

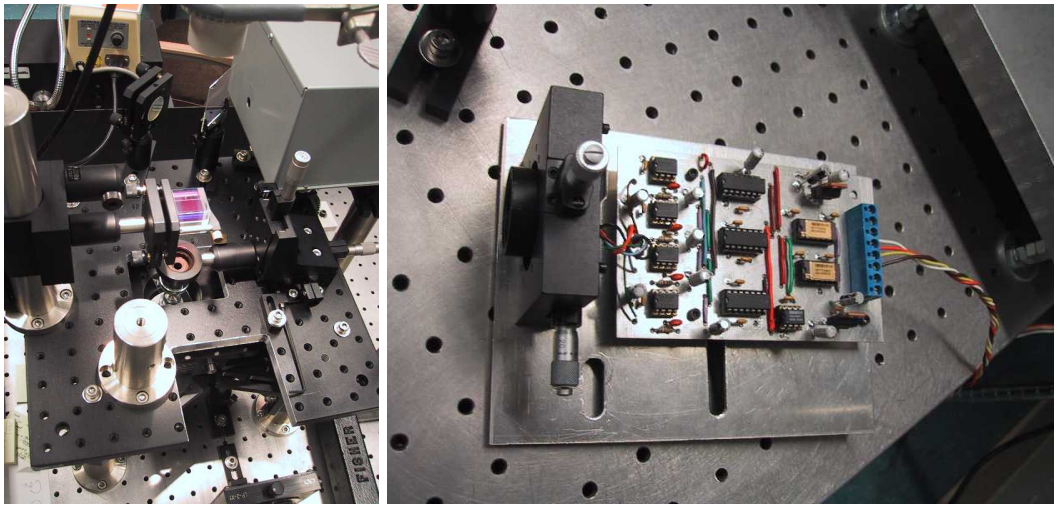

Figure 5.12: View of position detection system and circuit. Left figure shows one detector, which is shielded within an aluminum chassis. Right figure shows the circuit contained within the chassis.

summed using dual high-speed precision difference amplifiers to obtain three separate voltage channels that indicate the x position, y position, and total power of the incident beam. The x and y position voltages are normalized by the total power level using analog multipliers. Although normalization of the position signals could have been done using software, hardware was used to reduce computation time. To reduce signal noise due to stray capacitances, the circuit was built using a custom-built printed circuit board. The prototype was constructed by Verne Parmenter and two similar circuit boards were constructed based on the prototype. Since the displacement rise time for a typical optical tweezer is on the millisecond time scale[5] [10], it is recommended that position detectors have a temporal bandwidth of greater than 10 kHz [18]. The detector bandwidth can be adjusted by an appropriate choice of capacitors and resistors. Construction details can be found in Appendix B. All three photodetector circuits are powered using a single DC power supply (HP E3631A, Hewlett Packard). The circuits are protected from power fluctuations using ±15 V voltage regulators. To reduce electromagnetic noise, the photodetector circuits are shielded (enclosed) in an aluminum chassis.

For high sensitivity and ease of construction, we have chosen to operate the photodetector in the "photovoltaic" mode. This is preferred when the photodiode is used in low frequency applications (up to 350 kHz) [47]. The operating bandwidth in Hertz, f_{OP}, is given by [47]

$$f_{OP} = \frac{1}{2\pi R_F C_F}. \tag{5.12}$$

For the circuit shown in Figure 5.13, $R_F = 100k\Omega$ and $C_F = 330$ pF, implying a bandwidth of $f_{OP} = 4.8$ kHz. For fastest response and greatest bandwidth, the photodiode can be used in the "photoconductive" mode, which is more complicated [48]. Figure 5.14 shows the measured position of a trapped bead to a square wave trap displacement that has a peak-to-peak amplitude of 0.4 μm and frequency 2 Hz. Trap position x_T is actuated using an AOD.

The prototype photodetector circuit can be used to measure the position and power of the trapping laser beam after deflection by the gimbal-mounted mirrors. As shown in Figure 5.15,

[5]This is for a 300-nm step displacement at laser powers from 3–150 mW. Less power and greater step size will increase the lag time [10].

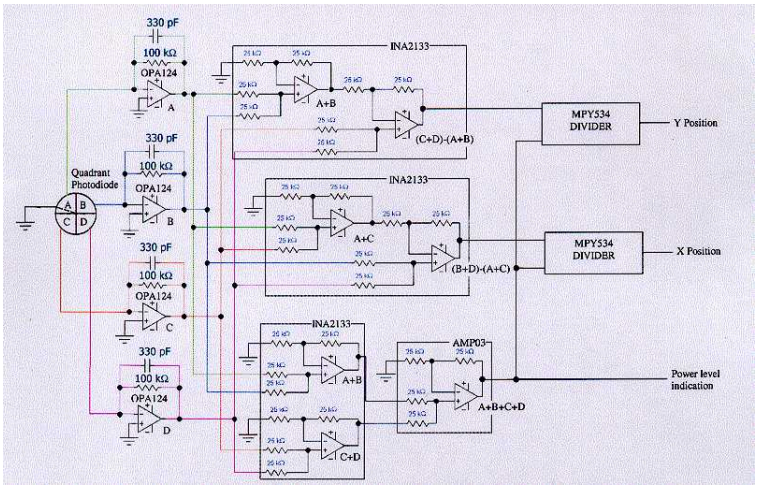

Figure 5.13: Position detector circuit diagram for using a quadrant photodiode in photovoltaic mode with a bandwidth of 4.8 kHz [46].

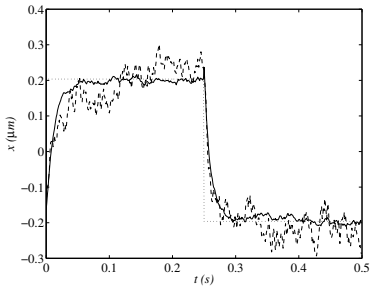

Figure 5.14: Step response of a trapped 10-μm diameter bead to a square wave trap displacement. Trap position x_T (dotted line), bead position x (dashed line) and the average bead position (solid line) for 30 traces of data are shown.

a small fraction ($\sim 4\%$) of the incoming beam can be deflected onto the photodetector using a beam sampler (Model 44-2434, Coherent). The drawback of this particular beam sampler is its large thickness, which causes a slight lateral shift in the incoming laser beam.

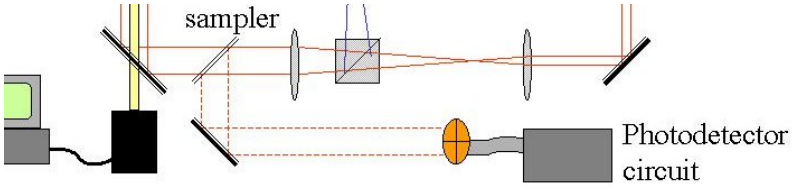

Figure 5.15: Optional Laser position detector. Detector measures trap position (x_T, y_T) and total power.

5.5 Computer Interface

For data acquisition and control, a computer interface has been established between the various sensors and actuators in the optical tweezer system. This was done using a 16-bit multifunction I/O board (Model PCI-6052E, National Instruments) and a high-speed 32-bit digital pattern I/O board (Model PCI-6534, National Instruments). The multifunction I/O board is mainly used to acquire signals from the photodetectors, while the digital I/O board is mainly used to generate the binary drive commands for the AOD driver. Selected specifications for the two boards are shown in Table 5.3 [49]. Laboratory signals are interfaced to each data acquisition board using shielded connector blocks (Model SCB-68, National Instruments) and shielded cables. A RTSI ("Real-Time System Integration") cable is used to synchronize the two data acquisition boards.

Board Parameter	Model PCI-6052E	Model PCI-6534
Analog Inputs	16 SE/8 DI	0
Resolution	16 bits	-
Sampling Rate	333 kS/s	-
Input Range	± 0.05 to ± 10 V	-
Analog Outputs	2	0
Resolution	16 bits	-
Output Rate	333 kS/s	-
Output Range	$\pm$ 10 V	-
Digital I/O	8	32
Maximum Rate		80 MBytes/s
Counter/Timers	2, 24-bit	

Table 5.3: Computer data acquisition board specifications [49]. (SE = Single Ended, DI = Differential, kS/s = kilosamples per second.)

Figure 5.16 shows the PC interface used for data acquisition and digital image processing. The data acquisition PC uses a *Pentium III* processor that runs *Windows NT*, while the image processing PC uses a *Pentium II* processor that runs *Windows 98*.

Figure 5.16: View of data acquisition PC (left) and digital image processing PC (right), including camera controller.

Chapter 6

Equipment Calibration

6.1 Manual Micrometers

The manual micrometers used in our system have a minimum incremental motion of 1 μm. According to the Newport catalog, the *ULTIMA* gimbal mirror-mount has a position resolution of 0.0011° when equipped with a 100 TPI (threads per inch) linear actuator [50]. This means that a 1° turn by a 100 TPI actuator will turn the *ULTIMA* gimbal-mirror mount by an angle of 0.0011°. A 1° turn by a 100 TPI actuator corresponds to linear motion of

$$\frac{0.01 \text{ in.}}{\text{turn}} \times \frac{1 \text{ turn}}{360^\circ} \times \frac{25.4 \times 10^3 \ \mu\text{m}}{1 \text{ in.}} = 0.7056 \ \mu\text{m}.$$

Therefore, the correspondenece between gimbal-mirror mount deflection $\Delta\theta_G$ and linear actuator translation Δx_{la} is

$$\frac{\Delta\theta_G}{\Delta x_{la}} = \frac{0.0011}{0.7056 \ \mu\text{m}} \times \frac{\pi \text{ rad}}{180^\circ} = 2.721 \times 10^{-5} \text{ rad}/\mu\text{m}.$$

Therefore, when used with an *ULTIMA* gimbal-mirror mount, the linear translation of the micrometer head is converted to angular motion of the mirror according to

$$\underbrace{\Delta\theta_G}_{\text{mrad}} = 0.02721 \underbrace{\Delta x_{la}}_{\mu\text{m}}. \tag{6.1}$$

Equation (6.1) can be combined with (5.6) to obtain the (expected) correspondence between linear actuator motion and trap position:

$$\underbrace{\Delta x_T}_{\mu\text{m}} = -0.02249 \underbrace{\Delta x_{la}}_{\mu\text{m}}, \tag{6.2}$$

where both Δx_T and Δx_{la} are in microns. In other words, linear actuator motion is reduced by a factor of 44.5 at the trap. Since the manual micrometers have a minimum incremental motion of 1 μm, (6.2) implies that the minimum incremental motion of the trap using a manual micrometer is 22.5 nm.

6.2 DC Motors

As listed in Table 5.1, the closed-loop DC motors are equipped with optical encoders that sense shaft position with an accuracy of either 4.6 nm or 8.4 nm (depending on which motor is being

used), while the minimum incremental motion for both motors in 50 nm. Therefore, according to (6.2), for an *ULTIMA* gimbal-mounted mirror equipped with these motors, the minimum incremental motion of the trap is 1.1 nm, while the optical encoders can sense trap position with an accuracy of either 0.10 nm or 0.19 nm.

6.3 Acousto-Optic Deflector

The AOD digital frequency synthesizer has an internal oscillator that generates a clock signal that is used to produce an RF (radio frequency) output. The output acoustic frequency f_a is a function of the internal clock rate f_{CK} and the decimal drive command K_{10} which is provided either manually or by computer interface:

$$f_a = \frac{f_{CK} K_{10}}{2^n}. \tag{6.3}$$

For our synthesizer, $f_{CK} = 1000$ MHz and $n = 31$. Therefore, a desired output acoustic frequency f_a can be generated by providing the decimal drive command

$$K_{10} = \frac{f_a 2^n}{f_{CK}} = \frac{f_a 2^{31}}{1000 \times 10^6}. \tag{6.4}$$

The decimal command K_{10} is converted to either hexadecimal (HEX) for manual interface or to binary for computer interface. The correspondence between a change in acoustic frequency Δf_a and the resulting change in lateral trap position Δx_T is obtained by combining (5.7) and (5.6):

$$\underbrace{\Delta x_T}_{\mu\text{m}} = -1.332 \underbrace{\Delta f_a}_{\text{MHz}}, \tag{6.5}$$

where Δx_T is in microns and Δf_a is in MHz. Setting $K_{10} = 1$ in (6.3), the minimum frequency step size is

$$(\Delta f_a)_{\min} = \frac{f_{CK}}{2^n}, \tag{6.6}$$

which is equal to 0.4657 Hz for our AOD driver. This value, when substituted into (6.5), shows that the minimum incremental motion of our trap using the AOD is 6.20×10^{-4} nm. This is significantly better than the corresponding values for the mechanical actuators discussed in previous sections.

Movement of trap position by the AOD can be calibrated using digital CCD images. The digital viewing system is first calibrated using a precision grid carrying a line pattern with 10-μm spacing (Part 11-7796, Coherent). Once the correspondence between pixels and nanometers has been obtained, the AOD is calibrated by capturing digital video images of a trapped bead. The bead is moved to different lateral positions along a straight line by driving the AOD at different frequencies. At each frequency, a digital image of the trapped bead is captured and saved. These saved images are later analyzed off-line using centroid-tracking algorithms, which can calculate the exact position of the trapped bead. Since the drive frequency for each image is known, the relation between drive frequency and trap position can be obtained.

As mentioned in Section 5.3.2, the first order deflection efficiency η_1 of the AOD varies across the acoustic frequency range. The manufacturer-calibrated efficiency profile for our AOD is shown in Figure 6.1 [44]. Although a local maximum of $\eta_1 = 80\%$ exists at the center frequency $f_{ac} = 35$ MHz, the global maximum of 97% occurs at $f_a = 41.5$ MHz.

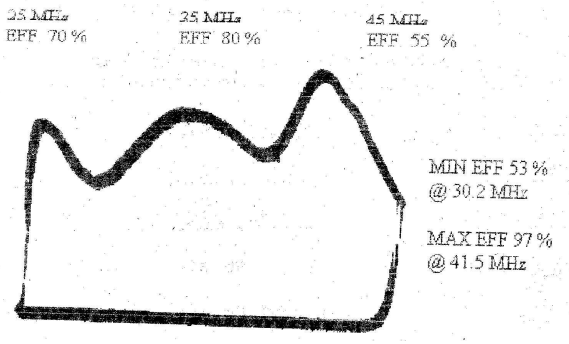

Figure 6.1: AOD first order deflection efficiency profile, re-printed from [44].

6.4 Position Detectors

As mentioned in Section 5.4, the most common method of detecting a trapped particle's position is to image the particle onto a quadrant photodiode, after magnification by a collecting objective. The collecting objective is used to collect the trapping laser light after it has passed through the trap. The trapped particle behaves like a lens, since after the laser light passes through the particle, the light is deflected before it goes through the collecting objective. The light that passes through the collecting objective is imaged on to a quadrant photodiode.

We used the method described by Visscher et al. in which the quadrant photodiode is placed specifically "on the optical axis in a position that is optically conjugate to the back focal plane of the microscope" [18]. Their method can be used to detect nanometer-scale displacements in the lateral direction, but it is "nearly insensitive to axial movements" [18]. The main advantage of this method is that "its response is rendered insensitive to the xy position of the optical trap itself within the specimen plane: instead, it responds mainly to a relative displacement between an object and the center of the trap, wherever the trap is located (in practice, within an area ~ 5 μm or so in diameter)" [18].

Once the AOD has been calibrated, the photodetector response can be calibrated using another trapped bead. As above, the bead is moved to different lateral positions along a straight line by driving the AOD at different frequencies. At each trap position (uniquely specified by each drive frequency), the detector response is recorded. Thus, the relation between trap position and detector output can be obtained. Since the AOD has high reproducibility, detector output can be averaged for many runs, which reduces the effects of Brownian noise in the trap [18]. Figure 6.2 shows the average detector step response of a trapped 9.61-μm bead for steps within the linear region. Recall that the detector has been aligned to measure relative position x_r. The detector response is almost linear, but the linear constant (slope) is sign dependent. For low data (negative steps), the detector response is approximately 0.79 V/μm, whereas for high data (positive steps), the detector response is approximately 1.18 V/μm. This disparity is due to combination of slight mismatches in resistor values in the high-impedance photodetector circuit and slight misalignments in the optical trap.

Visscher et al. claim that detector response is linear for trap displacements within $\sim \pm 100$ nm, but the detector range can be extended to $\sim \pm 200$ nm by fitting the detector output to a cubic or higher order polynomial [18]. For our system, the detector response is approximately linear within the entire linear range $\sim \pm 200$ nm, which corresponds to $\Delta x_r \pm 400$ nm. Furthermore, Allersma et al. showed that for small beads with diameter d, the position detector response, in volts per nanometer, should be proportional to d^3; after passing through a maximum, however, the detector response should decrease according to $1/d$ as the bead size becomes large [45].

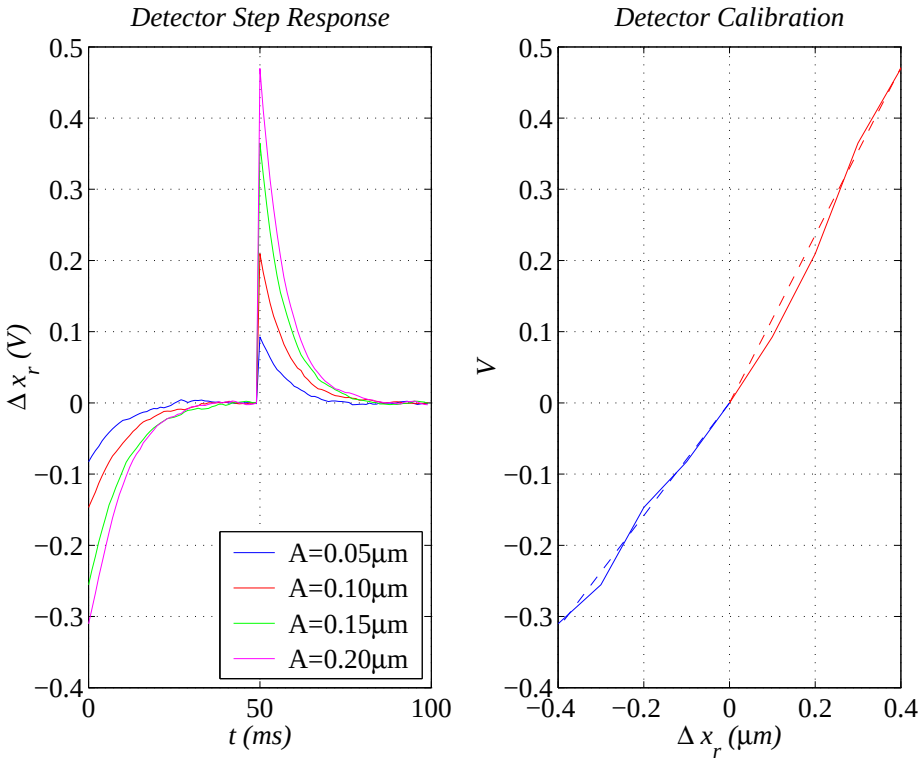

Figure 6.2: Average detector step response for a 9.61-μm diameter bead. Detector step responses are the average of 300 steps, each sampled at 1 kHz with a low-pass filter at 10 kHz.

Figure 6.3 shows the measured position of a trapped bead to a square wave trap displacement that has a peak-to-peak amplitude 0.4 μm and frequency 2 Hz. The characteristic frequency of the shown system is approximately 75 rad/s [36]. Trap position x_T is actuated using an AOD and bead relative position x_r is measured directly by the detector. Bead position x is calculated according to (3.1).

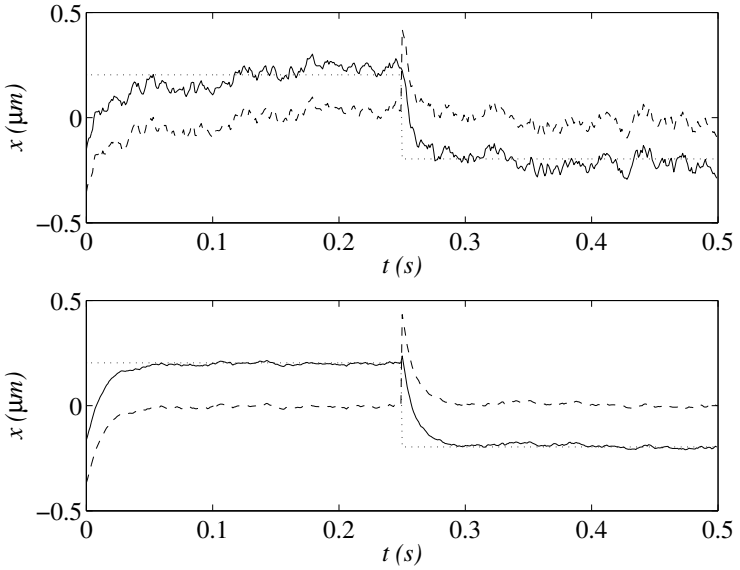

Figure 6.3: Step response of a trapped 10-μm bead for $\omega_c \approx 75$ rad/s. Top figure shows raw data and bottom figure shows the average of 30 cycles of data. Trap position x_T (dotted line), bead relative position x_r (dashed line), and bead position x (solid line) are shown.

Chapter 7

Off-Line Identification Methods

In this chapter, we discuss several off-line calibration methods that have been performed for our optical tweezer system. Most optical tweezer users, such as physicists and biophysicists, have been using off-line methods for empirical calibration of the trapping parameters described in Section 3.4. Each method has its own advantages and disadvantages, as summarized in Table 7.1.

ID Method	Trap Regime	ID Parameter	Position Detector	β	Motion Req.
Equipartition	Linear	α	Cal.PD (BW)	No	None
Power Spectrum	Linear	ω_c	PD (BW)	No	None
		α, β	Cal.PD (BW)	No	None
Step Response	Linear	ω_c	Cal.PD (BW)	No	Step
	Nonlinear	F_T, α_e	Cal.PD (BW)	Yes	Step
Drag Force	Linear	α	Cal.PD	Yes	Wave
	Nonlinear	α_e	Cal.PD	Yes	Wave
Lateral Escape Force	Nonlinear	v_{esc}, R_F	VCR	No	Rough
		$(F_T)_{\max}$, α_e	VCR	Yes	Rough
Lateral Capture	Nonlinear	v_R	VCR	No	Rough

Table 7.1: Overview of off-line identification methods. Cal. = Calibrated, PD = Photodetector, BW = with high analog bandwidth, β = Drag knowledge required.

Strongest trapping is expected for particles that are roughly the same size as the laser wavelength [14], which is $\lambda = 1.064$ μm, for our system. For testing and calibration of the optical tweezer, we trapped polystyrene spheres of diameters 10.06 μm, 9.61 μm and 1.05 μm.

7.1 Equipartition Method

In the equipartition method, the trap stiffness α is obtained by measuring the thermal fluctuations of trapped particle position x. According to the Equipartition theorem, for a particle bound in a harmonic potential,

$$k_B T = \alpha \sigma_x^2 \tag{7.1}$$

where σ_x^2 is the variance [18, 26]. As mentioned in Section 3.2, at biological temperatures, k_BT is approximately 4×10^{-3} pNμm [26]. The variance is defined as

$$\sigma_x^2 = E\{x^2\} - \{Ex\}^2, \tag{7.2}$$

which can be estimated directly from position data according to

$$\widehat{\sigma}_x^2 = \frac{1}{N-1}\sum_{i=1}^{N}(x_i - \overline{x})^2, \tag{7.3}$$

in which N is the total number of position data samples and $\overline{x}$ is the mean of the position data.

Although knowledge of the viscous drag coefficient is not needed, this method requires both a well-calibrated position detector with a high analog bandwidth and an environment with minimal noise [18]. The analog bandwidth of the detection system must be large because any lowpass filtering will underestimate σ_x^2 and hence, inflate α, while noise must be minimized because any sources of noise will artificially inflate σ_x^2 and therefore, underestimate α [18]. Note that, although the analog bandwidth needs to be high, the digital bandwidth (sampling rate) need not be correspondingly high because the position signal has random phase [30]. The top plot of Figure 7.1 shows the position fluctuations of a trapped 9.61-μm diameter polystyrene bead. A direct calculation of position variance according to (7.3) yielded $\sigma_x^2 = 0.0026\ \mu\text{m}^2$ for $N = 300000$ data samples. By substituting this variance value in (7.1), the trap stiffness is calculated as $\alpha = 1.5$ pN/μm. As shown in Section 7.2, the direct measurement of position variance overestimates the variance due to thermal motion alone. Therefore, the stiffness calculated in this section using (7.3) is an underestimate.

7.2 Power Spectrum Method

Much information can be obtained from the power spectrum of a trapped particle [1]. From (3.22), the equation of motion of particle position x in a stationary fluid with trap position x_T set to zero can be approximated by a Langevin equation [18],

$$\alpha x(t) + \beta \dot{x}(t) = F_L(t), \tag{7.4}$$

which, for zero initial conditions, can be written as

$$X(s) = G_{yd}(s)F_L(s), \tag{7.5}$$

in which

$$G_{yd}(s) = \frac{\frac{1}{\beta}}{s + \omega_c}, \tag{7.6}$$

according to (3.26). For a linear time-invariant (LTI) system such as (7.5), the input and output spectra are related according to

$$\phi_x(\omega) = G_{yd}(i\omega)G_{yd}(-i\omega)\phi_L(\omega), \tag{7.7}$$

where the input signal is assumed to have finite variance [34]. As mentioned in Section 3.2, $F_L(t)$ is a Langevin (random thermal) force with an average value of zero, $E\{F_L(t)\} = 0$, and constant single-sided power spectrum $S_L^+(f)$ given by

$$S_L^+(f) = 2F_L(f)F_L^*(f) = 4\beta k_B T, \tag{7.8}$$

[1] Some of the formulas in this section are borrowed from [26], but their derivation has been modified to conform with the stochastic normalization conventions from [34], which were explained in Chapter 4.

in which the Fourier transforms are double-sided [26]. Using (4.6), we can express (7.8) in terms of a single-sided spectral density as

$$\phi_L^+(\omega) = \frac{2\beta k_B T}{\pi}. \tag{7.9}$$

Substituting (7.9) and (7.6) into (7.7), we obtain

$$\phi_x^+(\omega) = \frac{2k_B T}{\pi\beta(\omega_c^2 + \omega^2)}. \tag{7.10}$$

In practice, it is convenient to express frequency in Hertz. In that case, we can re-express (7.7) using $\omega = 2\pi f$ and then substitute (7.8) directly to obtain

$$S_x^+(f) = \frac{k_B T}{\beta\pi^2(f_c^2 + f^2)}. \tag{7.11}$$

From (7.11), if one fits the power spectrum $S_x^+(f)$ to a Lorentzian shape, the roll-off frequency should be equal to the characteristic frequency of the trap f_c [26]. Therefore, with prior knowledge of viscous drag β, trap stiffness α can be obtained from the roll-off frequency. Furthermore, for low frequencies $f \ll f_c$, the power spectrum is approximately constant, $S_x^+(f) \approx S_0$, given by

$$S_0 = \frac{k_B T}{\beta\pi^2 f_c^2} \tag{7.12}$$

[26]. Equation (7.12) shows that β can be calculated once f_c and S_0 have been measured:

$$\beta = \frac{k_B T}{S_0\pi^2 f_c^2} \tag{7.13}$$

[26]. This is useful in experiments in which the drag coefficient is not known. Furthermore, trap stiffness α can be calculated as

$$\alpha = \frac{2k_B T}{\pi S_0 f_c} \tag{7.14}$$

[26]. At higher frequencies, $f \gg f_c$, the power spectrum is inversely proportional to the square of the frequency, $S_x^+(f) \propto \frac{1}{f^2}$, which is characteristic of free diffusion [26]. In effect, the particle does not feel the confinement of the trap during very short time intervals [26].

Since the power spectrum is estimated using discrete position data, we will explain how this is done. To avoid aliasing of the power spectrum, it is important to low-pass filter the signal before sampling it, with a cutoff frequency equal to the Nyquist frequency f_{Ny} given by

$$f_{Ny} = \frac{f_s}{2}, \tag{7.15}$$

where f_s is the sampling frequency of the position data. For some applications, it is also necessary to multiply the data by a normalized window to remove oscillations in the power spectrum [26], but we did not apply windowing to our data. For N discrete data points x_n separated by sampling time δt, the N independent Fourier components $X(f_m)$ are obtained according to

$$X(f_m) = \sum_{n=1}^{N} x_n e^{2\pi i n m/N}, \tag{7.16}$$

where the discrete frequencies f_m are defined as

$$f_m = \ m\delta f \quad \text{, for} - N/2 \leq \ m \leq N/2, \tag{7.17}$$

in which δf is the frequency resolution given by

$$\delta f = \frac{1}{N\delta t} \tag{7.18}$$

[26]. To deal with only positive frequencies, the single-sided power spectrum is calculated as

$$S_x^+(f_m) = \begin{cases} \frac{2}{N^2\delta f}|X(f_m)|^2 & \text{for } 0 < m < N/2 \\ \frac{1}{N^2\delta f}|X(f_m)|^2 & \text{for } m = 0, N/2 \end{cases} \tag{7.19}$$

[26]. Note that the highest frequency index in (7.19) is $N/2$, which means that the maximum frequency considered is equal to the Nyquist frequency f_{Ny}. Gittes and Schmidt show that the sum of all the discrete components of $S^+(f_m)$ for nonzero frequencies should be equal to the calculated variance σ_x^2 of the position data:

$$\sum_{m=1}^{N/2} S^+(f_m)\delta f = \sigma_x^2 \tag{7.20}$$

[26]. They also show that the trap position variance σ_x^2 due to thermal noise alone is given by

$$\sigma_x^2 = \frac{1}{2}\pi S_0 f_c \tag{7.21}$$

[26]. As mentioned in Section 7.1, although one might be tempted to calculate (estimate) σ_x^2 directly from position data using (7.3), such a variance would be artificially inflated due to very low-frequency noise from drift and mechanical vibrations [26]. Therefore, (7.21) provides a more accurate estimate of σ_x^2, according to our system model.

Note that the summation in (7.19) is the discrete equivalent of the continuous time definition of the single-sided position power spectrum,

$$S_x^+(f) := 2X(f)X^*(f), \tag{7.22}$$

in which $X(f)$ is the double-sided Fourier transform of $x(t)$ and $X^*(f)$ is its complex conjugate [20, 34, 18]. In continuous time, the Fourier transform pairs are defined as:

$$X(f) \ := \ \int_{-\infty}^{\infty} x(t)e^{-i2\pi ft}dt \tag{7.23}$$

$$x(t) \ = \ \int_{-\infty}^{\infty} X(f)e^{i2\pi ft}df. \tag{7.24}$$

[51]. Furthermore, the variance in continuous time can be expressed as:

$$\sigma_x^2 = \int_0^{\infty} S_x^+(f)df, \tag{7.25}$$

whose discrete equivalent is (7.20). Note that (7.25) is consistent with (4.4).

Formally, with some abuse of notation, we can denote the calculated power spectrum in (7.19) as $\widehat{S}_x^+(f_m)$, to indicate that it is an estimate (realization) of the actual power spectrum. The second order properties of the realization and actual spectrum are given by:

$$E\widehat{S}^+(f_m) \ = \ S^+(f_m) + \frac{C_1}{N} \tag{7.26}$$

$$E\{\left[\widehat{S}^+(f_m) - S^+(f_m)\right]^2\} \ = \ \left[S^+(f_m)\right]^2 + \frac{C_2}{N}, \tag{7.27}$$

where the constants C_1 and C_2 must satisfy the condition

$$\sum_{\tau=-\infty}^{\infty} |\tau R_x(\tau)| \leq C_1, C_2, \tag{7.28}$$

in which $R_x(\tau)$ is the covariance of x [52]. In other words, although the calculated power spectrum $\widehat{S}^+(f_m)$ is asymptotically unbiased, it is an extremely erratic function: the standard deviation of each point is typically equal to its mean [26]. Fortunately, if we calculate the power spectra for many different data sets, the values of $\widehat{S}^+(f_m)$ for a chosen frequency f_m will be uncorrelated. Therefore, to obtain a smooth curve, we can calculate power spectra for many data sets and then average them. The true spectral characteristics of the system can be obtained from the smooth, average power spectrum of an infinite number of data sets [26, 52]. Although smoother power spectra can be calculated from a single data set by applying a frequency windowing function to exploit the correlation between adjacent points on the spectrum, such methods may introduce an expected bias in the calculated power spectrum because the assumed correlation may not be symmetric [52].

Figure 7.1 shows both the position fluctuations of a trapped 9.61 μm bead due to Brownian (random thermal) motion and the computed average of 30 power spectra. According to the average power spectrum, $f_c \approx 19$ Hz, implying $\omega_c = 2\pi f_c \approx 119$ rad/s. Furthermore, $S_0 = 7.4 \times 10^{-5}$ μm^2/Hz, which implies that $\beta = 0.015$ pNs/μm using (7.13), $\alpha = 1.8$ pN/μm using (7.14), and $\sigma_x^2 = 0.0022$ μm^2 using (7.21). Recall from Section 7.1 that a direct calculation of position variance yielded $\sigma_x^2 = 0.0026$ μm^2, which results in an underestimate of trap stiffness. The calculated drag coefficient β is much lower than expected for a bead of this size at room temperature, which suggests that the viscosity of the PBS solution is less than water at room temperature. The viscosity may have decreased due to local heating near the laser focus; errors in detector calibration may also underestimate the viscosity. The small peak in the power spectrum near 200 Hz is likely due to noise in the laboratory environment and slight misalignments.

According to Visscher et al.,

> "The use of power spectra to calibrate trap stiffness can be particularly helpful in exposing potential problems with optical tweezers. If the tweezers are misaligned, the beam is corrupted, or something is awry with the position detection system, then the power spectrum rapidly becomes non-Lorentzian and/or displays peaks at specific noise frequencies. These details can be readily missed with other methods. Because only the roll-off frequency needs to be determined, the power spectrum may have arbitrary amplitude scaling, so that absolute calibration of the position sensor is unnecessary. When an absolute calibration is available, the value of the power spectrum at zero frequency also provides identical information to the Equipartition method" [18].

7.3 Step Response Method

The step response of a trapped particle can be used to calibrate characteristic frequency; application of a single step is known as a "bump test". From (3.22), particle position x in a stationary fluid is given by

$$\alpha x(t) + \beta \dot{x}(t) = \alpha x_T(t) + F_L(t). \tag{7.29}$$

Since the Langevin force $F_L(t)$ has an average value of zero, for a small trap step size $x_T(0^+)$ (i.e., within the linear force region R_l), the average step response is given by

$$x(t) = x_T(0^+)\left[1 - e^{-\omega_c t}\right] \tag{7.30}$$

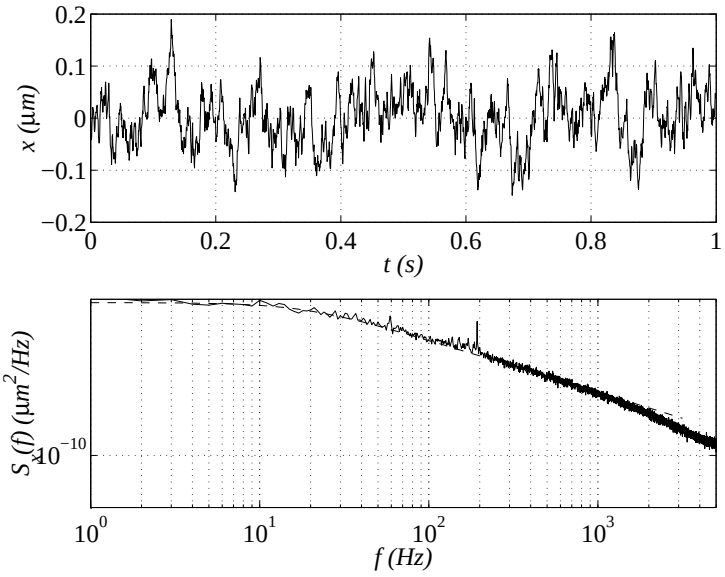

Figure 7.1: Top figure shows position fluctuations of a trapped 9.61-μm bead. Bottom figure shows the average of 30 power spectra and its Lorentzian fit (dashed line). Data was sampled at 10 kHz. The steep roll-off beyond 2 kHz is due to the limited analog bandwidth (4.8 kHz) of the position detectors, which act as a lowpass filter near the Nyquist frequency.

which shows that the characteristic frequency ω_c can be obtained from the step response data. Furthermore, trap stiffness α can be obtained from knowledge of the viscous damping factor β [18]. A calibrated detector is not required, but the time constant for trap movement must be faster than the characteristic damping time of the particle, $\tau_c := 1/\omega_c = \frac{\beta}{\alpha}$ [18].

A more robust method for obtaining ω_c is to re-arrange (7.30) and take the natural logarithm, to obtain

$$\ln\left[1 - \frac{x(t)}{x_T(0^+)}\right] = -\omega_c t. \tag{7.31}$$

If we define the left-hand side as Z, we obtain a linear expression

$$-Z = \omega_c t, \tag{7.32}$$

which shows that the characteristic frequency is equal to the slope of $-Z$ versus t [53].

The initial velocity of the particle $\dot{x}(0)$ can be obtained by taking the slope of the step response or by differentiating (7.30):

$$\dot{x}(t) = x_T(0^+)\omega_c e^{-\omega_c t}$$

and substituting $t = 0$:

$$\dot{x}(0) = x_T(0^+)\omega_c. \tag{7.33}$$

Knowledge of $\dot{x}(0)$ can be combined with (3.9) to calculate the trapping force $F_T(x_r)$ as a function of trap position:

$$F_T(x_r) = 6\pi\eta_f r_b x_T(0^+)\omega_c. \tag{7.34}$$

In fact, initial particle velocity data can be used to calculate (model) the entire nonlinear trapping profile of an optical trap, as demonstrated in [10]. Simmons et al. used velocity data to compute the experimental model shown in Figure 3.1.

Figure 6.2 shows the average step response of a trapped 9.61-μm bead to steps within the linear region. Figure 7.2 shows step response calibration results, according to a least squares fit to the linear relation (7.32). Note that early data (for very small t) is very sensitive to measurement noise and should not be used for calibrations. Clearly, the step response for $A = 0.05$ μm is very sensitive to Langevin noise (because of the small signal to noise ratio) and is not a good choice for calibration. According to the $A = 0.10$ μm step response, $\omega_c \approx 134.6$ rad/s for high data (positive steps) and $\omega_c \approx 107.3$ rad/s for low data (negative steps); according to the $A = 0.15$ μm step response, $\omega_c \approx 136.5$ rad/s for high data (positive steps) and $\omega_c \approx 104.1$ rad/s for low data (negative steps). The trap is stiffer for positive displacements than it is for negative displacements. This is indicative of a system that is not perfectly aligned; even a slight misalignment will cause a component of the axial restoring force to increase the lateral trapping force in one direction and reduce it in the opposite lateral direction. An important feature of the step response method is that it is capable of revealing and quantifying such asymmetries in trap stiffness.

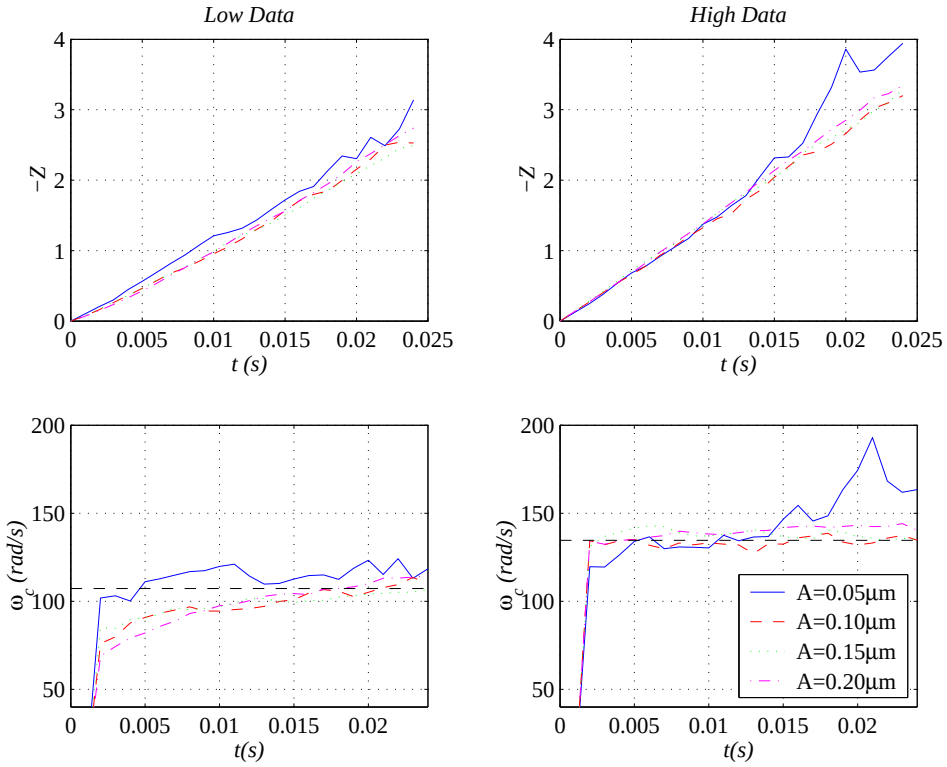

Figure 7.2: Calibration of characteristic frequency using step responses. Top plots show $-Z$ versus time; bottom plots show calibrated values of ω_c. Dashed lines in bottom plots show ω_c calibration for $A = 0.10$ μm steps. Clearly, the trap is stiffer for high data (positive steps) than it is for low data (negative steps).

Chapter 8

On-Line Identification Methods

During the 2004 American Control Conference, Metin Sitti of Carnegie Mellon University made the following observation during an invited tutorial session titled "Introduction to Micro-and Nano-Scale Sensors, Actuators and Robots":

> "Designing robust and stable controllers for nano-scale systems to achieve a specific task becomes very challenging. There are many constraints exerted on the controller design and performance by the time-varying nonlinear system dynamics, system parameter uncertainties and changes, short dynamic time-scales, disturbances from the environment, sensitivity to the changes in system parameters, limited sensor information, limited actuator motion precision and range, and limited power issues. Here, on-line system identification methods and adaptive and self-tuning controllers specific to the nano-scale systems become very attractive for a high performance and autonomous control." [27]

In practice, the characteristic frequency of an optical trap can vary due to laser fluctuations, local heating, and cross-contamination. Methods that depend on purely off-line (batch) data analysis do not account for these effects and may suggest an erroneous value for the characteristic frequency. Therefore, in a laboratory environment in which experimental conditions are not entirely constant, on-line (recursive) parameter estimation methods could potentially provide a more reliable (up-to-date) measure of characteristic frequency than the off-line methods from Section 7. This is especially true for experiments in which the effective trap stiffness changes due to a force interaction between a trapped bead and an external entity such as a biological molecule.

From (3.23), the noninertial equation of motion in the linear regime can be written in state space form as

$$\begin{aligned} \dot{x} &= -\omega_c x + \omega_c u + \frac{1}{\beta}\left(F_L + F_E\right) \\ y &= x + n, \end{aligned} \tag{8.1}$$

where we have included measurement noise n. Assuming zero initial conditions, (8.1) can be expressed using Laplace transforms as:

$$Y(s) = G_{yu}(s)U(s) + G_{yd}(s)\left[D_L(s) + D_E(s)\right] + N(s), \tag{8.2}$$

in which the first order transfer functions are given by

$$G_{yu}(s) = \frac{\omega_c}{s + \omega_c} \tag{8.3}$$

and

$$G_{yd}(s) = \frac{\frac{1}{\beta}}{s + \omega_c}. \tag{8.4}$$

A schematic block diagram of the linear plant P is reproduced in Figure 8.1.

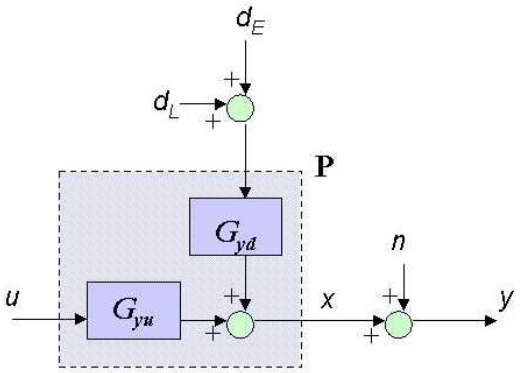

Figure 8.1: Linear plant block diagram, in which $u := x_T$, $d_L := F_L$, $d_E := F_E$, and n is measurement noise.

8.1 Discrete Time Parameter Estimation

In this section we describe how the continuous time system (8.2) can be converted to a discrete time model, which can be used for parameter estimation using a computer. The estimated discrete time parameters can be converted back to continuous time parameters using straightforward formulas. Much of the estimation techniques described in this section are from [52, 54].

8.1.1 Zero-Order-Hold Model

A continuous-time (CT) SISO model of the form

$$Y(s) = G(s)U(s) \tag{8.5}$$

with first order transfer function

$$G(s) = \frac{b}{s + a} \tag{8.6}$$

can be zero-order hold sampled with sampling time h to obtain the discrete-time (DT) difference equation

$$y(kh) = H(q)u(kh), \tag{8.7}$$

where k is a positive integer and $H(q)$ is the first order pulse transfer operator given by

$$H(q) = \frac{b_1}{q + a_1}, \tag{8.8}$$

in which q is the forward shift operator and

$$\begin{aligned} a_1 &= -e^{-ah} \\ b_1 &= \frac{b}{a}\left(1 - e^{-ah}\right) \end{aligned} \tag{8.9}$$

[55]. From (8.9) and (8.8), for $a = b = \omega_c$, we have

$$\begin{aligned} a_1 &= -e^{-\omega_c h} \\ b_1 &= 1 - e^{-\omega_c h} \end{aligned} \tag{8.10}$$

and the causal, zero-order hold representation of $G_{yu}(s)$ in (8.3) is given by

$$H_{yu}(q) = \frac{(1 - e^{-\omega_c h})q^{-1}}{1 - e^{-\omega_c h}q^{-1}}, \tag{8.11}$$

which is equivalent to a causal difference equation of the form $y(kh) + a_1 y(kh-h) = b_1 u(kh-h)$. Note that, according to (8.10):

$$b_1 = 1 + a_1. \tag{8.12}$$

Furthermore, from (8.8) and (8.11), we obtain

$$\frac{da_1}{d\omega_c} = \frac{db_1}{d\omega_c} = he^{-\omega_c h}. \tag{8.13}$$

The discrete output coefficient a_1 for different values of ω_c and h are shown in Figure 8.2.

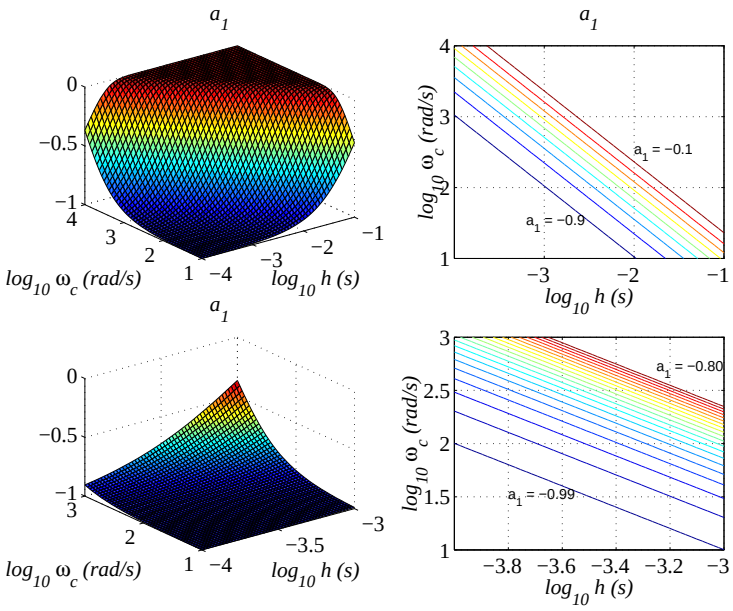

Figure 8.2: Discrete output coefficient a_1 as a function of characteristic frequency ω_c and sampling time h. Bottom plots show enlarged details of the top plots. As ω_c and h are decreased, a_1 tends to -1.

From (8.9), if we use a DT identification algorithm to obtain DT parameter estimates $\widehat{a}_1$ and $\widehat{b}_1$, the corresponding CT parameter estimates $\widehat{a}$ and $\widehat{b}$ are given by

$$\widehat{a} = -\frac{1}{h}\ln(-\widehat{a}_1) \tag{8.14}$$

$$\widehat{b} = -\left(\frac{\widehat{b}_1}{1+\widehat{a}_1}\right)\frac{1}{h}\ln(-\widehat{a}_1). \tag{8.15}$$

The causal, zero-order hold equivalent of $G_{yd}(s)$ in (8.4) is given by

$$[H_{yd}(q)]_{\text{causal}} = \frac{\frac{1}{\alpha}(1-e^{-\omega_c h})q^{-1}}{1-e^{-\omega_c h}q^{-1}}, \tag{8.16}$$

which is equivalent to a causal difference equation of the form $y(kh)+a_1y(kh-h) = \frac{b_1}{\alpha}d(kh-h)$. Although a causal filter such as (8.16) is a natural choice from a physical point of view, we would like to model the fact that the white noise disturbance has a direct term through the filter H_{yd}. In other words, the white noise is assumed to go through the denominator dynamics of the system before being added to the output [52]. To impose this noncausal condition while retaining the dynamic behavior of the causal disturbance model, we can shift the causal pulse transfer function in (8.16) by one time unit to obtain

$$H_{yd}(q) = \frac{\frac{1}{\alpha}(1-e^{-\omega_c h})}{1-e^{-\omega_c h}q^{-1}}, \tag{8.17}$$

which is equivalent to a causal difference equation of the form $y(kh) + a_1y(kh-h) = \frac{b_1}{\alpha}d(kh)$. Therefore, the combined difference equation corresponding to the models (8.11) and (8.17) is given by

$$y(kh) + a_1y(kh-h) = b_1u(kh-h) + \frac{b_1}{\alpha}d(kh), \tag{8.18}$$

in which $d(kh)$ is white noise with variance σ_d^2. Since the white noise contribution $\{d(kh)\}$ enters as a direct error term in the difference equation, the discrete model (8.18) is known as an "equation error model" [52]. If we normalize the white noise such that its coefficient in (8.18) is 1, we can express our discrete linear system in the standard ARX (Auto-Regression with eXtra inputs) form,

$$y(kh) + a_1y(kh-h) = b_1u(kh-h) + e(kh), \tag{8.19}$$

in which $\{e(kh)\}$ is white noise with variance $\sigma_e^2 = (\frac{b_1}{\alpha})^2\sigma_d^2$. Clearly, the output and input orders are $n_a = n_b = 1$. The ARX model structure is shown schematically in Figure 8.3.

In case the input u to the system is, in fact, piece-wise constant (i.e., zero-order held) between samples, the discrete representation (8.8) accurately describes the dynamics of the system (at the sampling instances), even in the continuous case [55]. If, on the other hand, the input is not piecewise continuous, our imposition of the ZOH on the input has a net effect of delaying the input by half of a sample [56]. The effect of this delay becomes negligible as the sampling time is decreased.

Normalizing the sampling time to 1, for ease of notation, we can re-write the ARX model (8.19) as the first order linear difference equation

$$y(t) + a_1y(t-1) = b_1u(t-1) + e(t). \tag{8.20}$$

Defining the parameter vector θ and the time-dependent regression vector $\phi(t)$ as

$$\theta = [a_1 \;\; b_1]^T \tag{8.21}$$

$$\phi(t) = [-y(t-1) \;\; u(t-1)]^T, \tag{8.22}$$

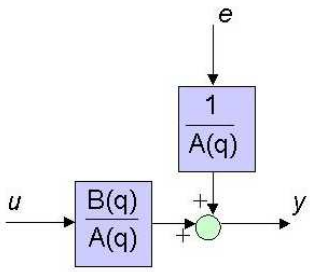

Figure 8.3: Standard ARX model structure [52]. $A(q) = 1 + a_1 q^{-1}$, $B(q) = b_1 q^{-1}$, and {e[k]} is white noise.

we can express the actual output as

$$y(t) = \phi^T(t)\theta + e(t), \tag{8.23}$$

and the (linearly) calculated output value as

$$\widehat{y}(t|\theta) = \phi^T(t)\theta. \tag{8.24}$$

Because of the linear relationship between ϕ and θ, the predictor (8.24) is known as a linear regression, even though ϕ and θ themselves can be nonlinear constructs.

8.1.2 General Estimation Framework

For a general discrete system described by the model

$$y(t) = G(q,\theta)u(t) + H(q,\theta)e(t), \tag{8.25}$$

in which $\theta \in \mathcal{D}_\mathcal{M} \subset \mathbb{R}^{\mathrm{d}}$ is the parameter vector, the general linear predictor is of the form

$$\widehat{y}(t|\theta) = W_y(q,\theta)y(t) + W_u(q,\theta)u(t), \tag{8.26}$$

where $\mathcal{D}_\mathcal{M}$ is the set of values that θ ranges over within the chosen model structure and d is the dimension of θ, that is, the number of (unknown) parameters being estimated [52]. For one-step ahead prediction,

$$\begin{aligned} W_y(q,\theta) &= 1 - H^{-1}(q,\theta) \\ W_u(q,\theta) &= H^{-1}(q,\theta)G(q,\theta) \end{aligned} \tag{8.27}$$

[52]. Assuming we have collected a set Z_N of discrete input output data from the system for N sampling instances:

$$Z_N = \{y(1), u(1), y(2), u(2), ..., y(N), u(N)\}, \tag{8.28}$$

a general parameter estimation method can be formally expressed as a mapping that uses the data set Z_N to select the best value (estimate) of the parameter vector $\widehat{\theta}_N$:

$$Z_N \rightarrow \widehat{\theta}_N \in \mathcal{D}_\mathcal{M} \subset \mathbb{R}^{\mathrm{d}}. \tag{8.29}$$

For our purposes, it is imperative that the system is identifiable. That is, the parameter estimates must be consistent:

$$\lim_{N\rightarrow\infty} \widehat{\theta}_N = \theta_*, \tag{8.30}$$

in which we use θ_* to denote the actual (true) parameter vector [54]. In other words, we require that the parameter estimates are unbiased:

$$E\widehat{\theta} = \theta_* \tag{8.31}$$

[54].

The question remains how we should define what the "best" estimate is. Defining the prediction error or *innovation* for a given estimator as

$$\epsilon(t,\theta) = y(t) - \widehat{y}(t|\theta), \tag{8.32}$$

we can define a general criterion function

$$V_N(\theta, Z_N) = \sum_{t=1}^{N} \beta(N,t) l\left(\epsilon(t,\theta)\right), \tag{8.33}$$

in which $\beta(N,t)$ is a weighting function and $l(\cdot)$ is a scalar norm that is typically positive. We can then define prediction error identification methods (PEM's) as methods in which we select the estimate $\widehat{\theta}_N$ according to the minimization

$$\widehat{\theta}_N = \widehat{\theta}_N(Z_N) = \arg\min_{\theta \in \mathcal{D}_{\mathcal{M}}} V_N(\theta, Z_N) \tag{8.34}$$

[52]. The Least Squares (LS) method is a special case of PEM in which we use the quadratic norm

$$l(\epsilon) = \frac{1}{2}\epsilon^2, \tag{8.35}$$

which, according to (8.33), (8.32) and (8.24), gives the weighted Least Squares criterion function

$$V_N^{LS}(\theta, Z_N) = \sum_{t=1}^{N} \beta(N,t) \frac{1}{2} (\underbrace{y(t) - \phi^T(t)\theta}_{\epsilon(t,\theta)})^2, \tag{8.36}$$

which can be minimized analytically to obtain the weighted LS estimate (LSE),

$$\widehat{\theta}_N^{LS} = \left[\frac{1}{N}\sum_{t=1}^{N} \beta(N,t)\phi(t)\phi^T(t)\right]^{-1} \frac{1}{N}\sum_{t=1}^{N} \beta(N,t)\phi(t)y(t), \tag{8.37}$$

[52]. Prediction error methods are sometimes referred to as generalized least squares (GLS) methods [54]. In general, (8.37) should not be used directly because it is sensitive to numerical rounding errors [54]. Defining the symmetric, deterministic matrix $R(N)$ and the column vector $f_y(N)$ as:

$$R(N) = \frac{1}{N}\sum_{t=1}^{N} \phi(t)\phi^T(t) \tag{8.38}$$

$$f_y(N) = \frac{1}{N}\sum_{t=1}^{N} \phi(t)y(t), \tag{8.39}$$

we can re-write the unweighted LSE as

$$\widehat{\theta}_N^{LS} = R^{-1}(N) f_y(N). \tag{8.40}$$

Furthermore, defining the parameter estimation error at time N as

$$\tilde{\theta}_N := \widehat{\theta}_N - \theta_*, \tag{8.41}$$

it can be shown that

$$E\{\tilde{\theta}_N\} = 0 \tag{8.42}$$

$$E\{\tilde{\theta}_N \tilde{\theta}_N^T\} = \sigma_e^2 [R^*(N)]^{-1}, \tag{8.43}$$

where σ_e^2 is the variance of $e(t)$ and

$$R^*(N) := \lim_{N\to\infty} R(N) \tag{8.44}$$

$$= \lim_{N\to\infty} \frac{1}{N} \sum_{t=1}^{N} \phi(t)\phi^T(t)$$

$$:= \overline{E}\{\phi(t)\phi^T(t)\} \tag{8.45}$$

and

$$f_e^*(N) := \lim_{N\to\infty} f_e(N) \tag{8.46}$$

$$= \lim_{N\to\infty} \frac{1}{N} \sum_{t=1}^{N} \phi(t)e(t)$$

$$:= \overline{E}\{\phi(t)e(t)\}, \tag{8.47}$$

in which the symbol $\overline{E}$ denotes an asymptotic ensemble average:

$$\overline{E} := \lim_{N\to\infty} \frac{1}{N} \sum_{t=1}^{N} \tag{8.48}$$

[52]. The above definition for $\overline{E}$ allows us to consider both stochastic and deterministic systems. For (8.43) to hold, we require that:

1. R^* is nonsingular
2. $f^* = 0$

[52]. The invertibility of R^* can be guaranteed by a wise choice of input properties; this issue will be discussed further in Section 8.1.3 [1]. The condition $f^* = 0$ holds if either (a) e is white noise, or (b) u is independent of the zero mean sequence e and $n_a = 0$ in the ARX model [52]. For our system, the first condition is satisfied because e is, indeed, white noise. Therefore, the asymptotic properties (8.43) hold for our system. In other words, the LSE is asymptotically unbiased and its covariance can be interpreted as being proportional to the system noise to signal ratio.

In general, the Mean Square Error (MSE) matrix in (8.43) is difficult to calculate for finite N [52]. However, based on the Cramer-Rao inequality, it can be shown that, for all unbiased parameter estimation methods and any N,

$$\mathrm{Cov}\widehat{\theta}_N \geq \kappa_0 \left[\sum_{t=1}^{N} E\psi(t,\theta_0)\psi^T(t,\theta_0) \right]^{-1}, \tag{8.49}$$

[1] R^* is usually singular if the input $u(t)$ is generated by a linear low-order feedback from the output [54].

where $\psi(t,\theta)$ is defined as the sensitivity (gradient) of $\widehat{y}(t|\theta)$:

$$\psi(t,\theta) := \frac{d}{d\theta}\widehat{y}(t|\theta) = -\frac{d}{d\theta}\epsilon(t,\theta) \tag{8.50}$$

[52]. Furthermore, $\kappa_0 = \sigma_e^2$ for Gaussian innovations [52]:

$$\epsilon(t,\theta_*) = e(t) = N(m,\sigma_e^2), \tag{8.51}$$

which holds for our ARX model. The lowerbound of the covariance matrix in (8.49) is achieved by the well-known Maximum Likelihood Estimator (MLE) [57, 52]. Furthermore, for the special case when the likelihood function is Gaussian, it can be shown that maximization of the likelihood function is equivalent to minimization of the least squares criterion [57]. That is, under this condition,

$$\widehat{\theta}_N^{ML} \equiv \widehat{\theta}_N^{LS}. \tag{8.52}$$

Although the ML method has this optimal convergence property, it is primarily an off-line method, and therefore, not useful for on-line calibrations[2] [55]. However, it can be shown that the LSE asymptotically achieves the Cramer-Rao bound for normal innovations as in (8.51). That is, as N tends to infinity,

$$\lim_{N\to\infty} \mathrm{Cov}\widehat{\theta}_N^{LS} = \frac{\sigma_e^2}{N}\left[\overline{E}\psi(t,\theta_*)\psi^T(t,\theta_*)\right]^{-1} \tag{8.53}$$

[52]. Since the above expression is valid for very large N, the question remains how accurate it is for small N. Ljung states that (8.53) is "valid within 10% for $N \geq 300$" [52]. Also, for ARX models, $\psi(t,\theta) = \phi(t,\theta)$, which allows us to express (8.53) in terms of the regression vector:

$$\lim_{N\to\infty} \mathrm{Cov}\widehat{\theta}_N^{LS} = \frac{\sigma_e^2}{N}\left[\overline{E}\phi(t,\theta_*)\phi^T(t,\theta_*)\right]^{-1} \tag{8.54}$$

[52]. For example, for the two-parameter ARX model,

$$y(t) + a_1 y(t-1) = b_1 u(t-1) + e(t), \tag{8.55}$$

we can use (8.22) to express (8.54) as:

$$\lim_{N\to\infty} \mathrm{Cov}\widehat{\theta}_N^{LS} = \frac{\sigma_e^2}{N}\begin{bmatrix} \overline{E}y^2(k) & -\overline{E}y(k)u(k) \\ -\overline{E}u(k)y(k) & \overline{E}u^2(k) \end{bmatrix}^{-1} \tag{8.56}$$

If we assume signals are ergodic, we can use (8.56) to evaluate approximate expressions for the covariance of unbiased estimates [3]. For example, with $e(t) = N(0,\sigma_e^2)$ and $u(t) = N(0,\sigma_u^2)$, we can show that

$$\mathrm{Cov}(\widehat{a_1})_N \approx \frac{1}{N}\frac{\sigma_e^2(1-a_1^2)}{\sigma_e^2 + \sigma_u^2(1+a_1)^2} \tag{8.57}$$

$$\mathrm{Cov}(\widehat{b_1})_N \approx \frac{1}{N}\frac{\sigma_e^2}{\sigma_e^2}, \tag{8.58}$$

[2] A recursive version of the ML method, the RML, is recommended for ARMAX model structures [52].

[3] A stationary stochastic process $x(t)$ is considered ergodic with respect to its first and second moments if

$$\frac{1}{N}\sum_{t=1}^{N} x(t) \rightarrow Ex(t)$$

$$\frac{1}{N}\sum_{t=1}^{N} x(t+\tau)x(t) \rightarrow Ex(t+\tau)x(t)$$

with probability 1 as $N \to \infty$ [54].

for large N. Similarly, for the single-parameter ARX model

$$y(t) + a_1 y(t-1) = (1+a_1)u(t-1) + e(t), \tag{8.59}$$

we can show that

$$\mathrm{Cov}(\widehat{a_1})_N \approx \frac{1}{N}\frac{\sigma_e^2(1-a_1^2)}{\sigma_e^2 + 2\sigma_u^2(1+a_1)}, \tag{8.60}$$

for large N. The asymptotic covariance expressions (8.57), (8.58) and (8.60) are plotted in Figure 8.4 for $\sigma_e^2 = 8\times10^{-4}$, $\sigma_u^2 = 10\sigma_e^2$, $\beta = 0.1$, and $h = 1$ ms. Clearly, the single parameter estimate converges faster than the 2 parameter estimate. In light of this fact and the relation (8.12), it may seem pointless to estimate both a_1 and b_1 instead of estimating just a_1. The reason that like to estimate both parameters, is that estimating two parameters serves as a check to verify that the algorithm converges to the same value (in CT) for both estimates.

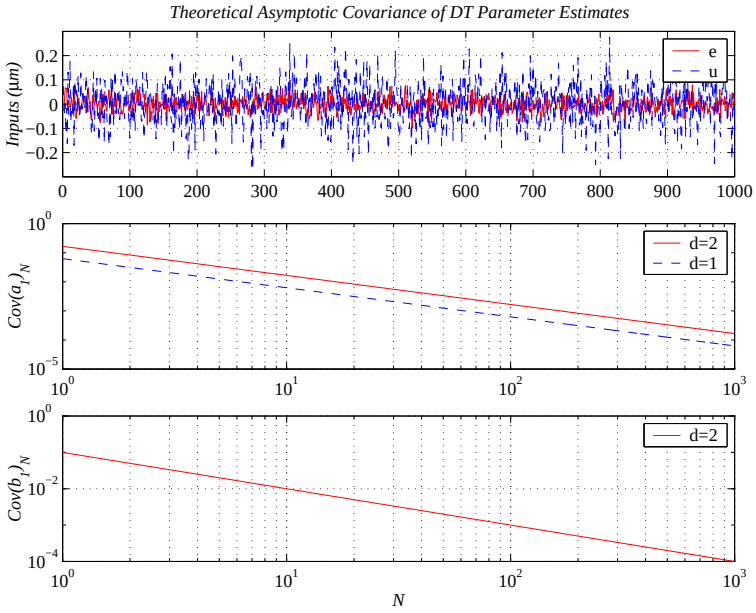

Figure 8.4: Theoretical Asymptotic Covariance of DT Parameter Estimates. Top figure shows input white noise; middle figure shows covariance of $\widehat{a}_1$; bottom figure shows covariance of $\widehat{b}_1$; d is the number of parameters being estimated. Simulations are for $\sigma_e^2 = 8\times10^{-4}$, $\sigma_u^2 = 10\sigma_e^2$, $\beta = 0.1$, and $h = 1$ ms.

Another issue of concern is whether the criterion function has local minima. Fortunately, for an LS method with a linear regression, the criterion function has no nonglobal (i.e., false) minima regardless of the data properties [52]. However, to distinguish between different models within a set, the data needs to be informative enough [52]. This issue will be discussed in the next subsection.

8.1.3 Choice of Input

When considering the choice of input, we are concerned with four issues:

1. Second-order properties (spectrum) of u

2. Shape of u

3. Sampling time h

4. Number of data points N.

Input Signal Spectrum

It is well-known that an open loop experiment is informative if the input is persistently exciting (PE), that is, if all modes of the system are excited during the experiment [52, 54]. A quasi-stationary signal $u(t)$ with spectrum $\phi_u(\omega)$ is considered PE if $\phi_u(\omega) > 0$ for almost all ω [52]. Similarly, $u(t)$ is PE of order n if $\phi_u(\omega) > 0$ on at least n points in the interval $-\pi < \omega \leq \pi$ [52]. For our ARX system, $n_b + n_a = 2$, which implies that, in the open loop case, an input signal with PE of order 2 or greater will be informative [52]. That is, a single sinusoidal input will be sufficient since it is PE of order 2. In fact, for our ARX system, even a single step input, which is only PE of order 1, will give consistent estimates as long as noise is present, that is $\sigma_e^2 > 0$ [54]. In this case, even though the input signal is not sufficiently PE, the noise excites the system in a constructive manner [4]. Although, in theory, it is quite easy to find an input signal that is PE for our ARX system, in practice, we prefer using more complicated signals with higher order of PE to obtain faster convergence properties.

Combining (8.50) and (8.53), we can express the covariance as

$$\lim_{N\to\infty} \text{Cov}\widehat{\theta}_N^{LS} = \frac{\sigma_e^2}{N}\left[\overline{E}\left(\frac{d}{d\theta}\widehat{y}(t|\theta)\right)\left(\frac{d}{d\theta}\widehat{y}(t|\theta)\right)^T\right]^{-1}. \tag{8.61}$$

Accordingly, a small variance in $\widehat{\theta}_N$ can be achieved by choosing a predictor that has a high sensitivity to θ [52]. Hence, it is logical to choose the inputs so that the predicted output is very sensitive to variations in θ. In the frequency domain, this requirement can be expressed as follows: spend the input power at frequencies in which the Bode plot is sensitive to parameter variations [52]. For a first order low pass filter, this implies that the input power should be concentrated at frequencies near the characteristic (cutoff) frequency ($\omega \approx \omega_c$), as shown in Figure 8.5.

In fact, in the frequency domain, PEM's can be interpreted as methods that fit the estimate of the model transfer function to the actual model transfer function according to a weighted norm equal to the signal to noise ratio for each frequency [52]. With some notational abuse, this statement can be expressed as

$$V_N(\theta, Z_N) \approx \frac{1}{4\pi}\int_{-\pi}^{\pi}\left|\widehat{G}_N(e^{i\omega}) - G(e^{i\omega},\theta)\right|^2 \frac{\widehat{\phi}_{uN}(\omega)}{\widehat{\phi}_{vN}(\omega,\theta)}d\omega. \tag{8.62}$$

Therefore, in addition to choosing the inputs so that the predicted output is very sensitive to variations in ω_c, we would also like to maximize the signal to noise ratio. Graphically, this condition is expressed in the lower plot of Figure 8.5, in which $|G(i\omega)|^n \times \frac{d|G(i\omega)|}{d\omega_c}$ is plotted as a function of input frequency ω, for different values of n. As the signal to noise ratio becomes more important (i.e., as n is increased), the input frequency band of interest shifts towards the left.

Ljung states that: "In practice, it is suitable to decide upon an important and interesting frequency band to identify the system in question, and then select a signal with more or less flat spectrum over this band." [52]. One way to do this is to let the input signal be a realization of Gaussian white noise, filtered through a linear band-pass filter, as described in the next section.

[4] An impulse input, which is PE of no order, is not useful because it will give a consistent estimate only if $e(2) = 0$, which is not true in general [54].

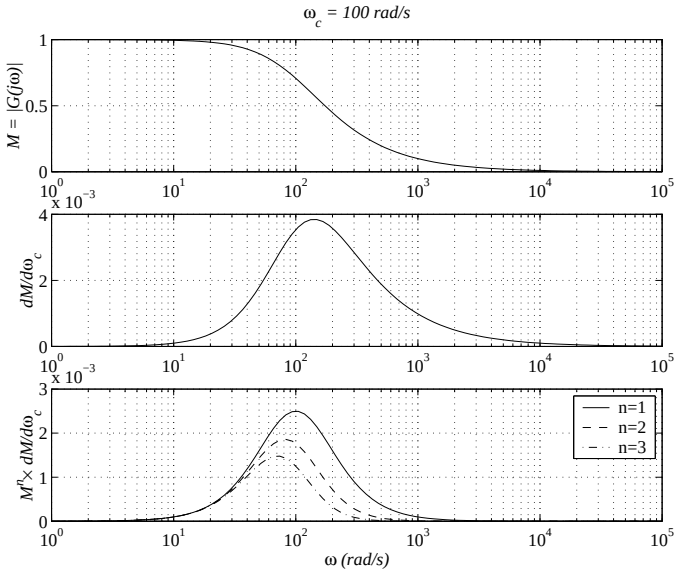

Figure 8.5: Bode plot sensitivity for $\omega_c = 100$ rad/s. Top plot shows magnitude frequency response; middle plot shows sensitivity of the magnitude with respect to ω_c; bottom plot shows combination of magnitude sensitivity and magnitude.

Input Signal Shape

The PE criterion is determined by the input spectrum and makes no reference to the input shape. Therefore, if we choose an input signal with the necessary order of PE, we must use other criteria to select the shape of the input signal.

From (8.56), we see that, for our first-order system, the covariance matrix is typically proportional to the input power [52]. Therefore we would like to maximize the input power within practical limits. This property can be expressed in terms of the crest factor C_r, which should be minimized to maximize the input power and thereby reduce the covariance of the parameter estimates [52]. For a discrete input sequence $u(k)$ with zero mean, the crest factor is given by

$$C_r^2 = \frac{\max\limits_k \; u^2(k)}{\lim\limits_{N\to\infty} \frac{1}{N}\sum\limits_{k=1}^{N} u^2(k)}, \tag{8.63}$$

which is clearly at its theoretical lower bound, $(C_r)_{\min} = 1$, for binary, symmetric signals such as a square wave [52].

Ljung states that: "for linear system identification, achieve a desired input spectrum for a signal with as small a crest factor as possible. Unfortunately, these properties are somewhat in conflict: if it is easy to manipulate a signal's spectrum, it tends to have a high crest factor and *vice versa*" [52]. An optimal crest factor of 1 is achieved by a random binary signal. Such a signal can be obtained by taking a realization of white, zero mean Gaussian noise that has been band-pass filtered and then setting the amplitude equal to one of two levels depending on its sign [52]. Taking the sign is a nonlinear operation that will distort the signal spectrum, but as long as the distortion is not too pronounced, we can still use the input signal. In fact, we can verify the signal spectrum properties off-line prior to using it. Figure 8.6 compares the calculated spectra

of white noise, filtered white noise, and random binary noise obtained by taking the sign of the filtered white noise. Taking the sign distorts the filtered spectrum by generating more power at frequencies outside of the filter pass-band. However, the pass-band is still clearly visible. A comparison between a square wave and sine wave is also provided in the figure. Although both waveforms have a frequency of 10 Hz, the square wave has a higher discrete power spectrum peak (0.3202 μm^2/Hz) than the sine wave 0.2 μm^2/Hz). The square wave also has power at several harmonic frequencies, whereas the sine wave has a clean spectrum with a single peak. Clearly, the square wave is a superior choice of input compared to the sign wave[5].

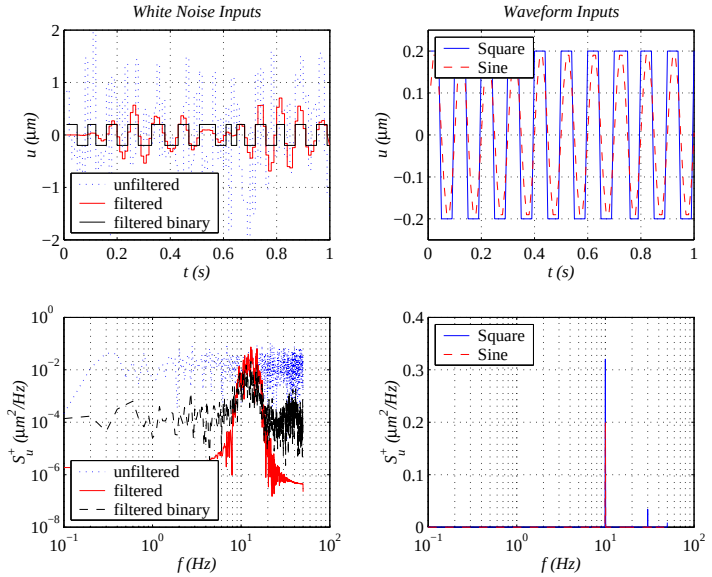

Figure 8.6: Comparison of different input signal spectra. Top plots show signals; bottom plots show their discrete power spectra. Left plots correspond to white noise (sampling time 10 ms; unit variance), white noise filtered through a 5th order Butterworth filter with passband 60-100 rad/s, and random binary noise obtained by taking the sign of the filtered white noise. Right plots correspond to the deterministic waveforms.

Another input signal with an (almost) optimal crest factor is the so-called pseudo-random binary signal (PRBS), which is a periodic, deterministic signal with white-noise like properties for large periods M [6]. In practice, we choose $M \geq N$ because, by definition, white noise is PE of all orders, while a PRBS signal is PE of order at most M [54]. The PRBS signal does not have exactly zero mean and its spectrum consists of a fixed number of equally spaced frequency peaks [52]. As M is increased, the first and second order properties of a PRBS approaches white-noise properties. If necessary, the PRBS can be given a low-frequency character by sampling at a clock frequency that is slower than the sampling frequency that generates the PRBS [52, 54]. In effect, the clock period acts like a lowpass filter. Ljung recommends a clock frequency that is 2.5 times the bandwidth of interest [52]. Therefore, for a system with characteristic frequency $\omega_c = 100$ rad/s, the clock frequency f_{PRBS} should be chosen as 250 rad/s, or about 40 Hz.

[5]Although the high frequency peaks in the square wave can cause some undesirable nonlinear effects, such effects can be ignored since the peaks rapidly diminish in magnitude. In practice, effects of the high frequency peaks can be minimized by sampling at a high rate and including an anti-alias filter.

[6]By white noise properties we mean first and second moment properties. The distribution functions can be very different because the PRBS takes on only two distinct values [54].

Sampling Time

When approximating a CT system by a DT model, there may be some modeling inaccuracies due to intersample behavior. The discrepancy between the CT model and the DT model can be made insignificant by sampling much faster than the bandwidth of the system [52]. An added benefit is that the high-frequency components in the output that originate from the input become insignificant [52]. In effect, we are ensuring that the process is well-damped above the Nyquist frequency.

However, "very fast sampling can lead to numerical problems, models fit in high frequency bands, and poor returns for extra work" [52]. This is clearly demonstrated in Figure 8.2, in which very high sampling times result in a DT output coefficient a_1 closer to the unit circle. Furthermore, for very fast sampling, the numerical value of a_1 becomes very sensitive with respect to the CT characteristic frequency ω_c, which opens the possibility of significant errors due to numerical roundoff and limited resolution of position detectors. Ljung suggests that, in most cases, the sampling frequency should be chosen "about ten times the bandwidth of the system" [52].

Number of Samples

According to the asymptotic expression (8.53), as the number N of data points increases, the covariance decreases: with an infinite number of (uncorrupted) data, the covariance should be zero. In practice, ofcourse, we collect a finite number of data points. The improvements in covariance with increased N are shown clearly in Figure 8.4.

8.2 Recursive Least Squares Method

This section describes the (discrete-time) Recursive Least Squares (RLS) method, as described in [52, 54].

8.2.1 RLS Algorithm

Some of the RLS results in this section are from [58]. In this section, we will use the sampling time h as the unit of time. We would like to compute the DT parameter estimate $\widehat{\theta}(k) := [\widehat{a}_1 \;\; \widehat{b}_1]^T$ at sample k that minimizes the weighted least-squares criterion:

$$\widehat{\theta}(t) = \arg\min_{\theta} \sum_{k=1}^{t} \beta(t,k)[y(k) - \phi^T(k)\theta]^2, \tag{8.64}$$

where $\phi(t) := [-y(t-1) \;\; u(t-1)]^T$ is the regression vector that contains the input and output data, and $\beta(t,k)$ is a weighting sequence with the property,

$$\begin{aligned} \beta(t,k) &= \lambda(t)\beta(t-1,k), \quad 0 \le k \le t-1 \\ \beta(t,t) &= 1, \end{aligned} \tag{8.65}$$

in which $\lambda(t)$ is the forgetting factor [52]. For a forgetting factor λ that tends to 1 as $t \to \infty$, the on-line and off-line LS methods have the same asymptotic properties [54]. The RLS algorithm is given by

$$\widehat{\theta}(t) = \widehat{\theta}(t-1) + L(t)\left[y(t) - \phi^T(t)\widehat{\theta}(t-1)\right] \tag{8.66}$$

$$L(t) = \frac{P(t-1)\phi(t)}{\lambda(t) + \phi^T(t)P(t-1)\phi(t)} \tag{8.67}$$

$$P(t) = \frac{1}{\lambda(t)}\left[P(t-1) - \frac{P(t-1)\phi(t)\phi^T(t)P(t-1)}{\lambda(t) + \phi^T(t)P(t-1)\phi(t)}\right], \tag{8.68}$$

where

$$P(t) := \left[\sum_{k=1}^{t} \beta(t,k)\phi(k)\phi^T(k)\right]^{-1} \tag{8.69}$$

is the scaled covariance matrix of the parameters at sample t [52]. The initial parameter vector is denoted as $\widehat{\theta}(0) = \theta_0$ and the initial covariance matrix is denoted as $P(0) = P_0$. In other words, θ_0 is what we guess the parameter vector to be before seeing the data, and P_0 reflects our confidence in this guess [52]. Another interpretation of such an initial covariance matrix is that it corresponds to the parameters having a prior covariance proportional to P_0 [55]. Without *a priori* information, common choices are $\widehat{\theta}(0) = 0$ and $P(0) = pI$, where $p > 0$ is a large scalar [54]. With initial conditions, the parameter estimates are given by

$$\begin{aligned} \widehat{\theta}_N^{LS} &= \left[\beta(N,0)P_0^{-1} + \sum_{t=1}^{N} \beta(N,t)\phi(t)\phi^T(t)\right]^{-1} \\ &\quad \times \left[\beta(N,0)P_0^{-1}\theta_0 + \sum_{t=1}^{N} \beta(N,t)\phi(t)y(t)\right] \end{aligned} \tag{8.70}$$

[52]. Clearly, for large P_0, the inverse matrix P_0^{-1} is small, and the difference between (8.70) and (8.37) becomes negligible. In fact, with time, the on-line estimate approaches the off-line estimate,

$$\widehat{\theta}^{RLS}(t) \approx \widehat{\theta}_{\text{offline}} \tag{8.71}$$

[54]. In fact, if we denote the time at which (8.71) first holds as t_0, it can be shown that, for $\lambda = 1$, a good choice of p is given by

$$p \gg \frac{1}{t_0 \sigma_\phi^2}, \tag{8.72}$$

in which σ_ϕ^2 is the minimum variance of the elements of $\phi(t)$ [54]. A typical practical choice of t_0 is 10-25 [54].

The initial regression vector is specified as $\phi(0) = [0 \;\; 0]^T$. The forgetting factor λ is constant for a slowly changing system and can be chosen according to

$$\lambda = 1 - \frac{1}{K}, \tag{8.73}$$

where K is the memory time constant. Data older than K samples are weighted by a factor $e^{-1} \approx 36\%$ compared to the most recent data [52]. For an LTI system, it is natural to require that all data be given equal weight, which implies that no data is discounted. By setting $K \to \infty$ in (8.73), we obtain $\lambda = 1$.

8.2.2 Computer Simulations

In general is always advisable to test an identification experiment using computer simulations before implementing it on an actual experiment [52].

The CT system described by (3.24) was simulated using *Simulink* with a simulation sampling time of $t_s = 0.1$ ms, corresponding to 10 kilosamples per second (kS/s). The Langevin disturbance was modeled as band-limited white noise with bandwidth 10 kHz and constant power $S_L^+(f) = 1.6 \times 10^{-3} \; \frac{\text{pN}^2}{\text{Hz}}$. As mentioned in Section 3.2, this represents the Langevin force that

acts on a 10-μm diameter polystyrene bead at biological temperatures. To facilitate comparison with experimental results in Section 8.2.4, the actual characteristic frequency of the simulated system is chosen as $\omega_c = 100$ rad/s. According to Section 8.1.1, for RLS sampling time $h = 1$ ms, the actual parameters are given by

$$a = b = 100 \tag{8.74}$$

and

$$\theta_* = \begin{bmatrix} a_1 \\ b_1 \end{bmatrix} = \begin{bmatrix} -0.9048 \\ 0.09516 \end{bmatrix}. \tag{8.75}$$

We assume an initial characteristic frequency guess of $\widehat{\omega}_c(0) = 80$ rad/s, which corresponds to an error of 20% (20 rad/s). According to Section 8.1.1, the initial parameter conditions are given by

$$\widehat{a}(0) = \widehat{b}(0) = 80 \tag{8.76}$$

and

$$\theta_0 = \begin{bmatrix} \widehat{a}_1(0) \\ \widehat{b}_1(0) \end{bmatrix} = \begin{bmatrix} -0.9231 \\ 0.0769 \end{bmatrix}. \tag{8.77}$$

For invertibility, we assume the initial covariance matrix is of the form

$$P_0 = \begin{bmatrix} p & 0 \\ 0 & p \end{bmatrix},$$

in which $p > 0$. In the simulations that follow, we will denote the input signal amplitude by A and input frequency by f.

Figure 8.7 shows results for an input square wave with $A = 0.2$ μm and $f = 10$ Hz. The top left plot shows the input and output (I/O) signals; the top right plot shows the power spectrum of the input signal; the bottom left plot shows the DT parameter estimates, and the bottom right plot shows the CT parameter estimates. For comparison, the DT estimates are plotted as $1 + \widehat{a}_1$ and $\widehat{b}_1$, since, according to (8.12), we would like these two quantities to converge to the same value. After fluctuating wildly at the onset, both the DT and CT parameter estimates eventually converge close to the correct values of b_1 and ω_c, respectively. The $\omega_c \pm 5\%$ and $\omega_c \pm 2\%$ limits are included in the bottom right plot as a reference.

The parameter estimates display fluctuations that diminish with time. In particular, the CT parameter estimates settle to within 5% of ω_c in under 0.6 s and to within 2% in under 1 s. The direct correspondence between the DT and CT estimates can be seen from the similar shape of their plots. As shown in (8.13), fluctuations in the DT estimates will amplify the CT estimates by a factor of over 1000. The reason for the paramater fluctuations is the Langevin disturbance. This is demonstrated by Figure 8.8, which is a simulation for zero Langevin disturbance (a hypothetical situation). In this case, no oscillations are observed and the CT parameter estimates settle to within 5% of ω_c in under 3 ms (3 iterations) and to within 2% in under 4 ms (4 iterations).

8.2.3 Effect of Identification Parameters

Input Frequency and Amplitude

We found that both $f = 2$ Hz and $f = 20$ Hz resulted in slower parameter convergence. The value of $f = 10$ Hz was used because it gave the fastest convergence for the chosen value of ω_c.

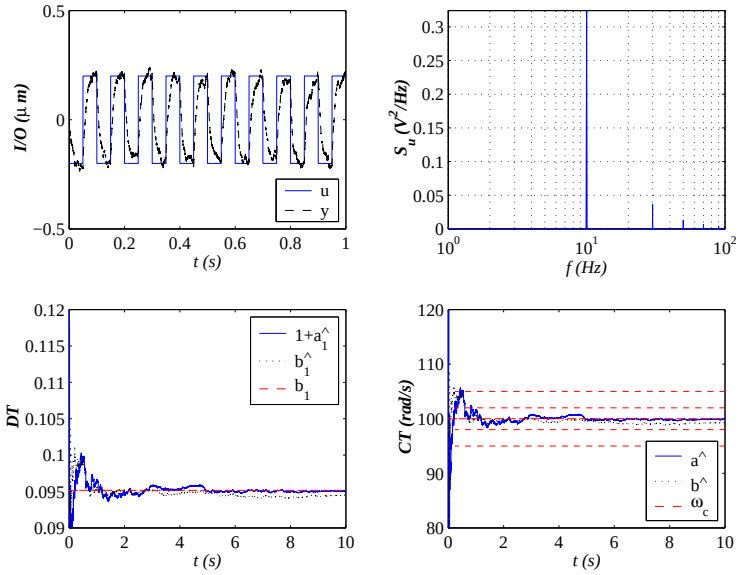

Figure 8.7: Simulation of RLS for $h = 1$ ms, $\lambda = 1$, $p = 10^4$; square wave input, $A = 0.2$ μm and $f = 10$ Hz. Dash-dotted lines on the bottom right plot show $\omega_c \pm 5\%$ and $\omega_c \pm 2\%$ limits.

This is consistent with the practical recommendation that input power be selected at frequency bands in which a "good model is particularly important", or more formally, frequencies at which the "Bode plot is sensitive to parameter variations" [52]. Figure 8.9 shows the covariances of the CT parameter estimates for different input frequencies and different input amplitudes for $\omega_c = 100$ rad/s. Clearly, the covariances of the DT coefficients improve (decrease) with increased amplitude (greater input signal to noise ratio). The covariance of the input coefficient b_1 decreases with frequency because it depends directly on the PE criterion [55]. The output coefficient a_1 is more sensitive to noise and its covariance is lowest for input frequencies near the characteristic frequency.

Input Shape

We found that a square wave provides much faster convergence than a sinusoidal input ($f = 10$ Hz). The superiority of the square wave can be explained using the crest factor C_r, as described in Section 8.1.3. Figure 8.10 shows results for an input PRBS with $A = 0.2$ μm and cutoff at $f_{PRBS} = 40$ Hz. The CT parameter estimates settle to within 5% of ω_c in under 0.5 s and to within 2% in under 1 s. The results are comparable to a square wave with $f = 10$ Hz.

Simulation results for binary filtered white noise was not promising. Parameter convergence was slow compared to the square wave and the PRBS.

Forgetting Factor

According to (8.73), a forgetting factor of $\lambda = 0.9999$ corresponds to a memory time constant of $K = 10000$ samples, which is equivalent to $t = 10$ s for $h = 1$ ms. Figure 8.11 shows simulation results for $\lambda = 0.9999$. The CT parameter estimates settle to within 5% of ω_c in under 0.6 s, and they settle within the 2% limit within 1 s. However, the parameter estimates fluctuate more for the $\lambda = 0.9999$ case than for the $\lambda = 1$ case shown in Figure 8.7. Intuitively, since the past data is exponentially discounted with time, there is less smoothing of the past data.

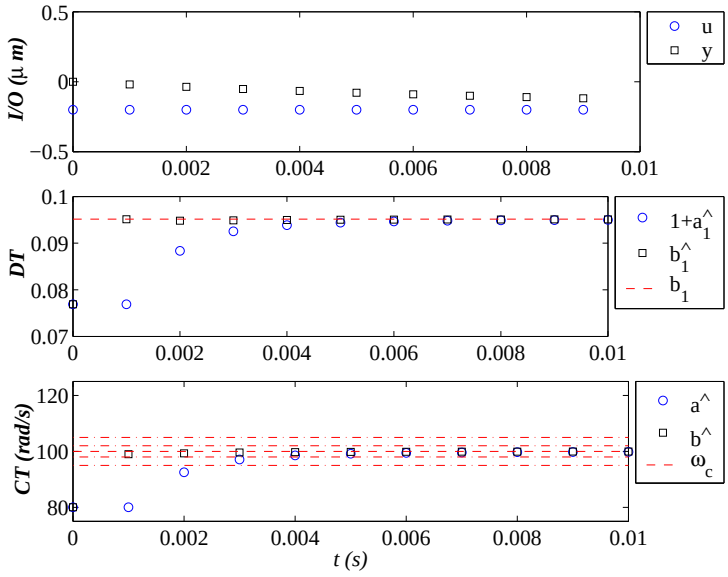

Figure 8.8: Hypothetical $F_L = 0$ simulation of RLS for $h = 1$ ms, $\lambda = 1$, $p = 10^4$; square wave input, $A = 0.2$ μm and $f = 10$ Hz.

It is known that, as λ is decreased, the RLS algorithm becomes more sensitive, which results in quicker convergence [54]. However, the RLS also becomes more sensitive to noise, which causes the parameter estimates to oscillate about its actual value [54]. To exploit these convergence effects of the forgetting factor, it is sometimes customary to choose the forgetting factor as

$$\lambda(t) = 1 - \nu^t[1 - \lambda(0)], \tag{8.78}$$

where typical values are $\nu = 0.99$ and $\lambda(0) = 0.95$ [54].

Lowpass Filter Bandwidth

In general, filtering will not distort the input-output relationships provided both the input and output are subject to exactly the same filters [52]. Effects if filtering can also be neglected by sampling fast enough that the Nyquist frequency is significantly greater than the bandwidth. Computer simulations show that an analog RC lowpass filter with a 1 kHz bandwidth will reduce the parameter estimates by about 5%, while a bandwidth of 5 kHz will reduce the estimates by about 1%.

8.2.4 Experimental Results

Since the RLS algorithm does not require real-time feedback control, we were able to investigate its performance by collecting input and output data from our system using *LabVIEW* data acquisition software and hardware and then processing the data using *MATLAB* [36]. Data was sampled at a rate of 1 kS/s with an analog lowpass filter at 10 kHz. The lowpass filter has a higher cutoff than the Nyquist frequency to a avoid undesirable distortion of the output signal; the price we pay is the signal contains some measurement noise, but this is negligible. Also, small offsets in the position detection system's alignment can distort the estimation data. In the case of a square wave, such offsets can be removed by averaging.

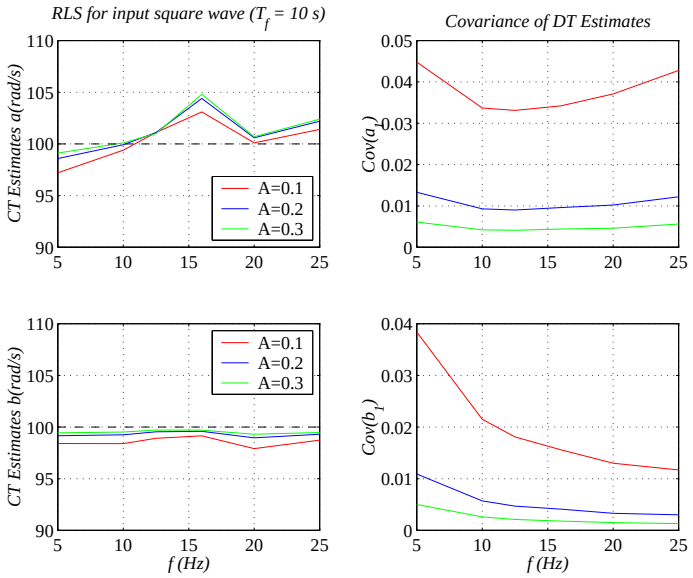

Figure 8.9: Comparison of RLS simulations for different square wave input frequencies and amplitudes; $\omega_c = 100$ rad/s, $h = 1$ ms, $\lambda = 1$, $p = 10^4$; square wave input for 10 seconds. Top plots correspond to output coefficients a and a_1; right plots correspond to input coefficients b and b_1.

Figure 8.12 shows results for an input square wave with $A = 0.15$ μm and $f = 10$ Hz.

After initial fluctuations, the parameter estimates appear to reach steady values within 9 seconds. The values of the CT estimates after 30 s are $\widehat{a} = 112$ rad/s and $\widehat{b} = 113$ rad/s. Figure 8.13 shows results for an input square wave with $A = 0.05$ μm and $f = 10$ Hz. The parameter estimates appear to reach steady values within 19 seconds. The values of the CT estimates after 30 s are $\widehat{a} = 105$ rad/s and $\widehat{b} = 114$ rad/s.

Experimental results for a PRBS were not encouraging. In theory, the PRBS should provide fast convergence, comparable to a square wave input. As mentioned above, offsets or misalignments in the position detection system can severely distort the estimation. In the case of square wave, we were able use averaging to calculate and remove the offset from our data prior to identification. For the PRBS, this is much more difficult to do because the signal has large periods. In practice, ofcourse, we should not have to adjust offsets when implementing an on-line calibration because that would defeat the purpose of on-line calibrations. The solution is to implement an automatic tracking system that can automatically align the laser beam onto the detector. The tracking criterion can be implemented in an RLS manner. Alternatively, a second (diffuse) laser beam can be used purely for position detection [18].

8.2.5 Closed Loop Recursive Least Squares

In Chapter 9, we discuss the implementation of CT feedback control. In this section, we will jump ahead and consider whether identifying the system in closed loop has the potential of providing significant benefits in identification speed. Substituting (9.9) and (9.8) into (9.4), the output transfer function for proportional control with pure error feedback and no measurement

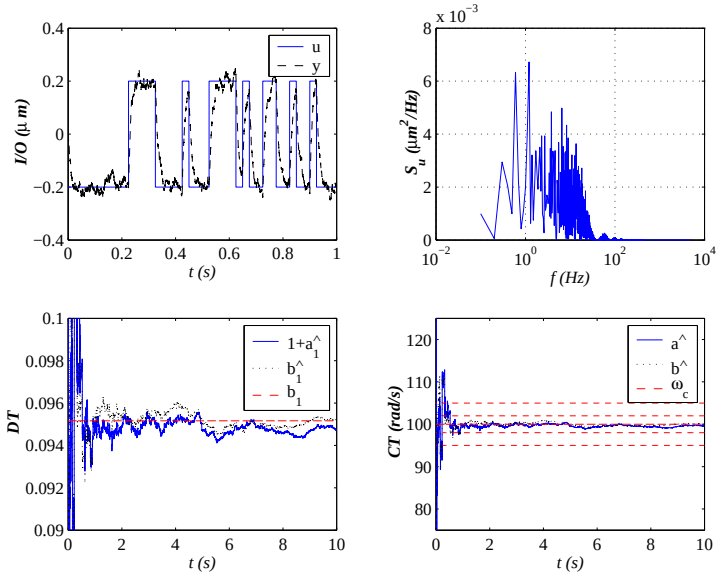

Figure 8.10: Simulation of RLS for $h = 1$ ms, $\lambda = 1$, $p = 10^4$; PRBS input, $A = 0.2$ μm and $f_{PRBS} = 40$ Hz. $\alpha = 10$, $\beta = 0.1$: $\omega_c = 100$.

noise is given by:

$$Y(s) = \frac{\omega_c}{s + (1 + k_p)\omega_c} R(s) + \frac{\frac{1}{\beta}}{s + (1 + k_p)\omega_c} D(s), \tag{8.79}$$

in which we require $k_p > -1$ for closed loop stability. The DC gain from reference to output is $\frac{1}{k_p+1}$, which implies that choosing positive k_p will reduce output amplitude, when compared to open loop operation. The signal to noise ratio (between reference input and Langevin disturbance) is not affected, however. Choosing negative k_p will increase the output amplitude. Consequently, when using $k_p < 0$, the reference input r should be chosen sufficiently small that the output does not move beyond the linear trapping region. From the results of Section 8.1.1, it is clear that the ZOH parameter estimates are given by the expressions:

$$\begin{aligned} a_1 &= -e^{-(k_p+1)\omega_c h} \\ b_1 &= \frac{1}{k_p + 1}\left[1 - e^{-(k_p+1)\omega_c h}\right], \end{aligned} \tag{8.80}$$

and the corresponding CT estimates are given by (8.14) and (8.15), which are reproduced below:

$$\widehat{a} = -\frac{1}{h}\ln(-\widehat{a}_1) \tag{8.81}$$

$$\widehat{b} = -\left(\frac{\widehat{b}_1}{1 + \widehat{a}_1}\right)\frac{1}{h}\ln(-\widehat{a}_1). \tag{8.82}$$

From the transfer function from reference to output in (8.79), we see that the estimates of the characteristic frequency are given by:

$$(\widehat{\omega}_c)_a = \frac{\widehat{a}}{k_p + 1} \tag{8.83}$$

$$(\widehat{\omega}_c)_b = \widehat{b}. \tag{8.84}$$

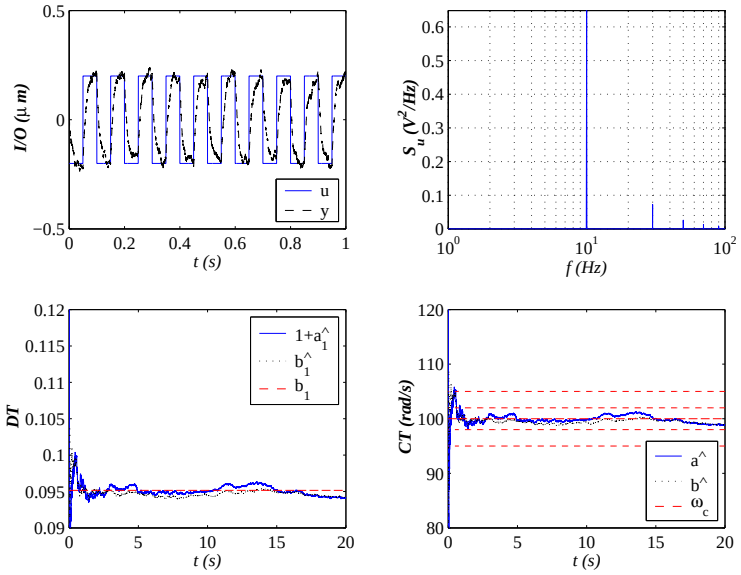

Figure 8.11: Simulation of RLS for $h = 1$ ms, $\lambda = 0.9999$, $p = 10^4$; square wave input, $A = 0.2$ μm and $f = 10$ Hz.

Figure 8.14 shows a (hypothetical) closed loop RLS simulation for $k_p = 9$ for an input square wave with $A = 2$ μm and $f = 10$ Hz. The parameter estimates converge very quickly and show less initial overshoot than the open loop case. However, the usefulness of this type of closed loop calibration depends on bead size, which determines the trapping radius. For example, the input amplitude of $A = 2$ μm used in this simulation cannot be implemented for a smaller, 1-μm diameter bead.

8.2.6 Identification of Cubic Spring Constants

As mentioned in Section 7.3, the nonlinear trapping force can be computed using initial velocity data for step responses within the trapping region [10]. In this section, we will reformulate the RLS algorithm from Section 8.2 to compute the nonlinear trap parameters. From 3.16, in the absence of external forces, our noninertial system can be represented in state space form as:

$$\begin{aligned} \dot{x} &= \frac{\psi(x-u)}{\beta}\left[\alpha_3(x-u)^3 - \alpha_1(x-u)\right] + \frac{1}{\beta}F_L \\ y &= x. \end{aligned} \tag{8.85}$$

Defining

$$w := (x-u)^3, \tag{8.86}$$

we can express (8.85) within the trapping radius as:

$$\begin{aligned} \dot{x} &= \frac{1}{\beta}\left[\alpha_3 w - \alpha_1(x-u)\right] + \frac{1}{\beta}F_L \\ y &= x, \end{aligned} \tag{8.87}$$

This can be expressed using Laplace transforms as:

$$Y(s) = \frac{b_w}{s+a}W(s) + \frac{b_u}{s+a}U(s) + \frac{\frac{1}{\beta}}{s+a}D(s), \tag{8.88}$$

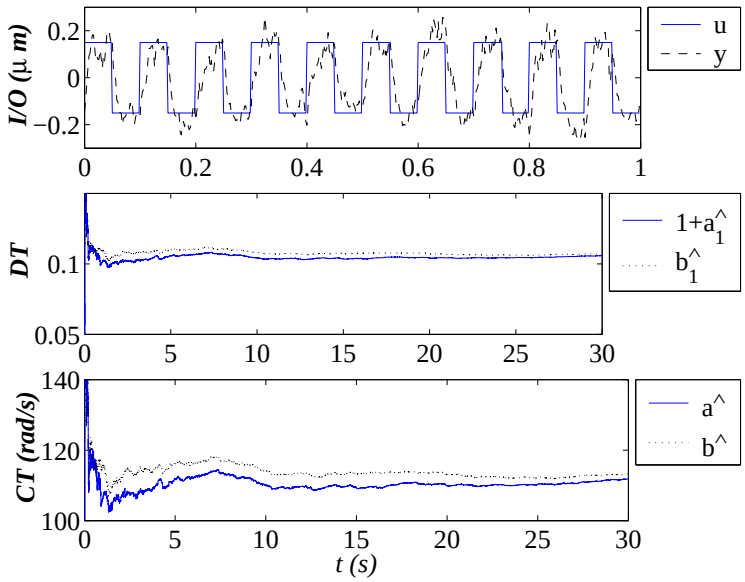

Figure 8.12: Implementation of RLS for experimental data with $h = 1$ ms, $\lambda = 1$, $p = 10^4$; square wave input, $A = 0.15$ μm and $f = 10$ Hz.

in which $a = b_u = \frac{\alpha_1}{\beta}$, $b_w = \frac{\alpha_3}{\beta}$, and $D(s) = F_L(s)$. Comparing with the results from Section 8.1.1, the difference equation corresponding to (8.88) is given by

$$y(kh) + a_1 y(kh-h) = b_{w1} w(kh-h) + b_{u1} u(kh-h) + e(kh), \tag{8.89}$$

where $a_1 = -e^{\frac{\alpha_1}{\beta}h}$, $b_{u1} = 1 - e^{\frac{\alpha_1}{\beta}h}$, $b_{u1} = \frac{\alpha_3}{\alpha_1}(1 - e^{\frac{\alpha_3}{\beta}h})$. By defining the regression vector (for normalized time) as

$$\phi(t) = [-y(t-1) \;\; \{y(t-1) - u(t-1)\}^3 \;\; u(t-1)]^T, \tag{8.90}$$

the parameter vector $\theta = [a_1 \;\; b_{w1} \;\; b_{u1}]^T$ can be estimated using the RLS method described in previous sections. This enables us to calculate the CT quantities $\frac{\alpha_1}{\beta}$ and $\frac{\alpha_3}{\beta}$.

8.3 Continuous Time Parameter Estimation

In case a real-time computer interface is not available, parameters can be estimated on-line using continuous-time (CT) identification methods. This section considers one such CT adaptive identification method.

8.3.1 Normalized Gradient Approach [7]

Reference [59] describes a normalized gradient (NG) algorithm for adaptive parameter estimation of linear time-invariant systems. This section describes the application of that NG approach for calibrating the characteristic frequency of an optical tweezer. The NG algorithm is designed for on-line CT system identification. For implementation of on-line CT parameter estimation, the optical tweezer system is parametrized according to the equation

$$P(s)y(t) = Z(s)u(t),$$

[7] Most of this section is excerpted from [36].

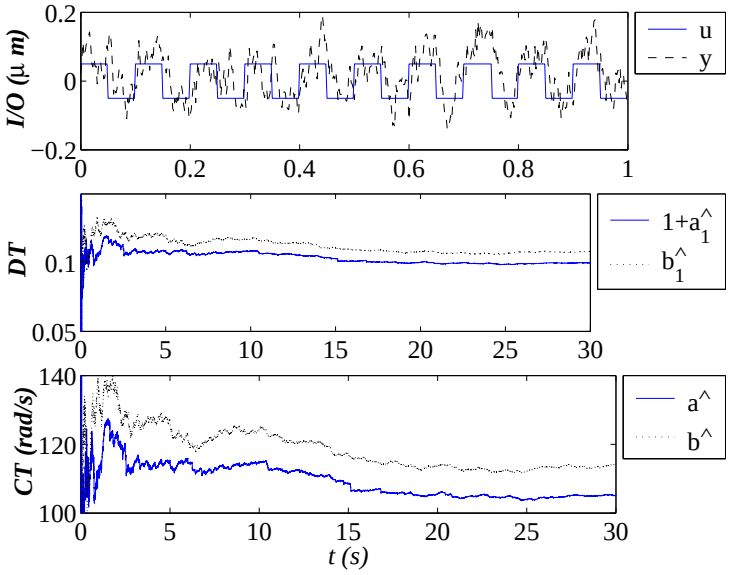

Figure 8.13: Implementation of RLS for experimental data with $h = 1$ ms, $\lambda = 1$, $p = 10^4$; square wave input, $A = 0.05$ μm and $f = 10$ Hz.

where $u(t) \in \mathbb{R}$ is the measured system input and $y(t) \in \mathbb{R}$ is the measured system output and initial conditions are assumed to be zero. According to (3.27), for a noninertial system, $Z(s)$ is a constant $z = \omega_c$ (order $n_Z = 0$), while $P(s)$ is a first order ($n_P = 1$) polynomial of the form

$$P(s) = s + p,$$

in which $p = \omega_c$ is a constant. As in the (DT) RLS case, although both p and z are identical for our system, we will estimate both parameters, instead of just one. Estimating two parameters serves as a check to verify that the algorithm converges to the same value for both. Choosing a Hurwitz polynomial $\Lambda(s) = s + \lambda$, of the same degree as $P(s)$, the unknown (actual) parameter vector θ_* is given by

$$\theta_* := [z \quad \lambda - p]^T \in \mathbb{R}^2,$$

and the known (measured) regressor vector $\phi(t)$ is given by

$$\begin{aligned} \phi(t) &= \frac{1}{\Lambda(s)} [u(t) \quad y(t)]^T \\ &= \left[\frac{u(t)}{s+\lambda} \quad \frac{y(t)}{s+\lambda} \right]^T \in \mathbb{R}^2. \end{aligned}$$

Letting $\theta(t)$ be the estimate of θ_*, to be obtained using an adaptive NG algorithm, the estimation error $\epsilon(t)$ is defined as

$$\epsilon(t) := \theta^T(t)\phi(t) - y(t) = \tilde{\theta}^T(t)\phi(t),$$

where the parameter error $\tilde{\theta}(t) := \theta(t) - \theta_*$. The quantity $\theta^T(t)\phi(t)$ is the estimate of system output based on the parameter estimates.

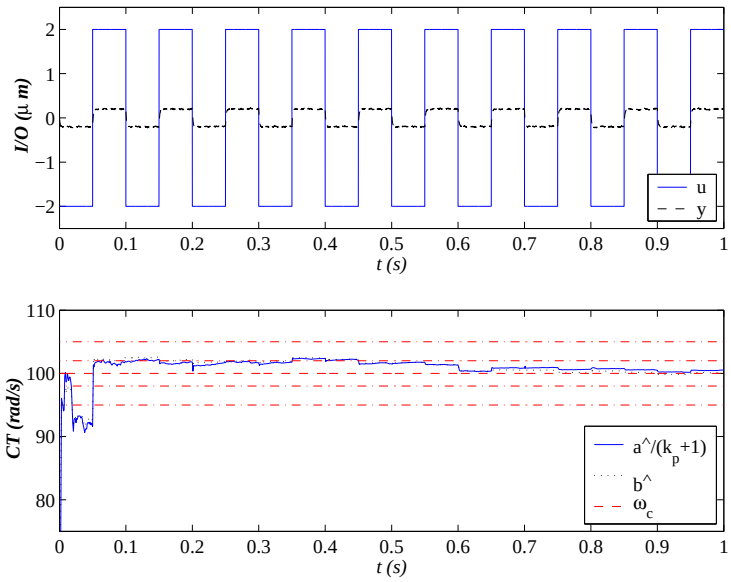

Figure 8.14: Simulation of closed loop RLS for $k_p = 9$ (proportional control), $h = 1$ ms, $\lambda = 1$, $p = 10^4$; square wave input, $A = 2$ μm and $f = 10$ Hz.

Algorithm

The NG algorithm is based on tuning the parameter vector $\theta(t)$ in the steepest descent direction to minimize a normalized instantaneous cost function

$$J(\theta) = \frac{\epsilon^2}{2M^2} = \frac{(\theta - \theta_*)^T \phi \phi^T (\theta - \theta_*)}{2M^2}, \tag{8.91}$$

where $M(t)$ is a normalizing signal given by

$$M(t) = \sqrt{1 + \kappa \phi^T(t)\phi(t)}, \tag{8.92}$$

in which $\kappa > 0$ is a design parameter. For the chosen $J(\theta)$, the adaptive parameter update law is given by:

$$\dot{\theta}(t) = -\frac{\Gamma \phi(t) \epsilon(t)}{M^2(t)}, \ \theta(t_0) = \theta_0, \ t \geq t_0. \tag{8.93}$$

where $\Gamma = \Gamma^T > 0$ and θ_0 is an initial estimate of θ_*. The NG algorithm described by Equation (8.93) guarantees that

1. $\theta(t), \dot{\theta}(t), \frac{\epsilon(t)}{M(t)} \in \mathcal{L}^\infty$, and
2. $\frac{\epsilon(t)}{M(t)}, \ \dot{\theta}(t) \in \mathcal{L}^2$.

Furthermore, the parameter estimate $\theta(t)$ will converge to the actual parameter value θ_* exponentially fast if the regressor signal $\phi(t)$ is persistently exciting (PE), which is true if the system input $u(t)$ contains at least $n_P + n_Z + 1 = 2$ frequencies [59]. For example, this condition can be met by choosing $u(t)$ as a single sinusoid. The above convergence properties hold true even for nonzero initial conditions [59].

Computer Simulations

According to a previous step response calibration, $\omega_c = 78.5$ rad/s and according to a previous power spectrum calibration, $\omega_c \approx 75$ rad/s [36]. For simulation purposes, we assumed that the actual characteristic frequency is $\omega_c = 78$ rad/s, but that a previous (off-line) calibration has given us the impression that it is 65 rad/s. The NG algorithm described by Equations (8.91), (8.92), and (8.93) was simulated using $\lambda = 10$, $\Gamma = \begin{bmatrix} 10000 & 0 \\ 0 & 10000 \end{bmatrix}$, $\kappa = 1$, and an initial characteristic frequency estimate of 65 rad/s, which corresponds to $\theta_0 = [65 \quad -55]^T$. The input signal $u(t)$ is a square wave with amplitude 0.2 μm and frequency 2 Hz. For reasons that will become clear in the next section, the initial position of the trapped particle is chosen as $x(0) = -0.2$ μm. Since the NG algorithm is implemented using position voltages, the position amplitudes can be scaled (within practical limits) to improve convergence times. For this section, the NG algorithm has been implemented for position signals that have been scaled by a gain of 5 V/μm. Computer simulation results are shown in Figure 8.15. Due to the heavily damped nature of the system, the input and output signals remain bounded and both parameter estimates converge to within 1% of the actual ω_c in under 9 s, but the pole parameter estimate p converges faster than the zero parameter estimate z.

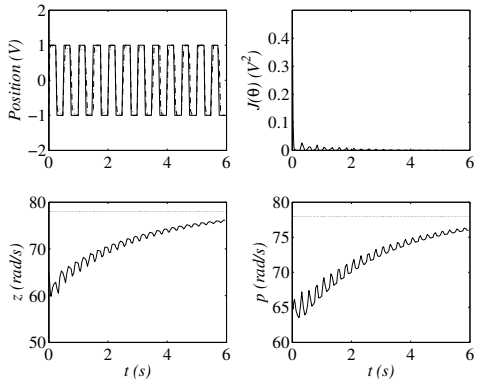

Figure 8.15: Simulation of NG Algorithm for $\omega_c = 78$ rad/s with 2 Hz input signal and no input disturbance. The estimate of system output, based on the parameter estimates, is shown as a dotted line in the top left plot. Parameter p converges to within 5% error in 4.0 s and z converges in 4.3 s.

Experimental Results

Since the NG algorithm does not require real-time feedback control, we were able to investigate its performance by collecting input and output data from our system using data acquisition hardware and then processing the data using *MATLAB*. Figure 8.16 shows the results of applying the NG algorithm using raw experimental data for a trapped 10 μm bead using the same NG algorithm parameters used in Section 8.3.1. The initial estimate was chosen as 65 rad/s. Clearly, the large position fluctuations caused by Brownian motion overwhelm the NG algorithm and the parameter estimates oscillate wildly. This is indicative of a system dominated by noise.

As used in the step response method from Section 7.3, the effects of the stochastic position disturbance can be greatly reduced by averaging a sufficiently large amount of position data. The disturbance-free computer simulations from Section 8.3.1 represent the limiting case for an infinitely large amount of data. Figure 8.17 shows the results of applying the NG algorithm for

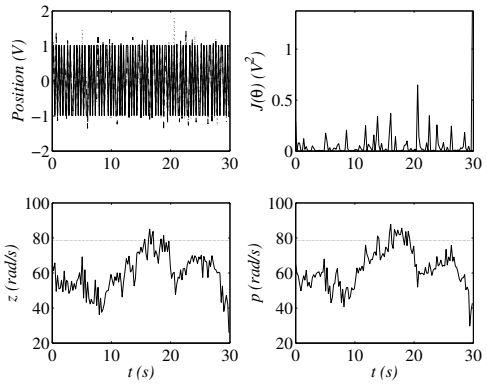

Figure 8.16: Implementation of NG Algorithm for raw data. Parameters oscillate wildly.

experimental data that has been averaged after 30 seconds (60 cycles). Parameter p converges to a final value of 79 rad/s $\pm 2\%$ and z converges to 77.5 rad/s $\pm 1.5\%$. The slight difference between the final values for z and p are almost certainly due to residual position fluctuations in the computed average. Such fluctuations can be reduced by averaging a larger quantity of data.

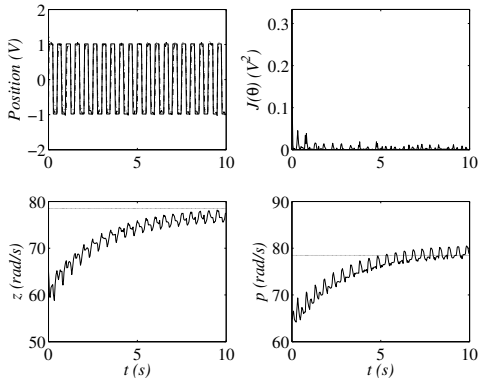

Figure 8.17: Implementation of NG Algorithm for the average of 30 s of data. Parameter p converges to within 5% ot its final value in 3.5 s and z converges in 5.4 s.

Rather than waiting to collect 30 cycles of data, computing its average, and then implementing the NG algorithm, we suggest implementing the algorithm online by computing a running average of the data once per second. Figure 8.18 shows the results of applying the NG algorithm for the running average of experimental data. Parameter p converges to a final value of 78 rad/s $\pm 2\%$ and z converges to 75.5 rad/s $\pm 2\%$, but there is a large initial estimation error (towards 0 rad/s) due to the large disturbance present in the first few cycles of the running average. If necessary, this initial offshoot can be reduced by implementing the algorithm starting with the average of a few cycles.

In practice, the NG algorithm can be implemented using both analog circuitry and using real-time data processing software. Since our experimental results suggest that some form of averaging is necessary to reduce the position disturbance to a manageable level, software control is the logical choice for online implementation of the NG algorithm described in this section.

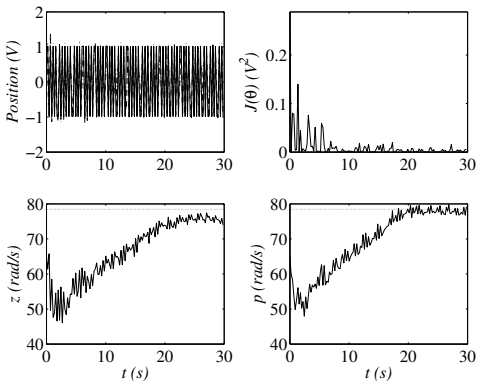

Figure 8.18: Implementation of NG Algorithm for data averaged once per second. Parameter p converges to within 5% of its final value in 17.6 s and z converges in 18.9 s.

Chapter 9

Linear Feedback Control

A well-tuned position feedback system can be used to convert the optical tweezer into either an isometric position clamp (used to keep the position of trapped particles constant) or an isotonic force clamp (used to keep the force acting on trapped particles constant) [18].

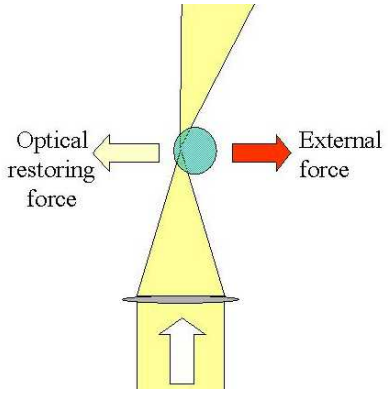

Figure 9.1: Force balance between external force and optical restoring force.

When the optical tweezer is used as a position clamp, the feedback signal that is applied by the controller provides a measure of the forces that the trapped particles undergo. According to (3.22), once the position of the trap x_T and the position of a bead x are known (from photodetector measurements), the external force F_E acting on a trapped bead in the x direction can be calculated as [10]:

$$F_E(t) = \alpha x_r + \beta \dot{x} - F_L(t) = \alpha(x - x_T) + \beta \dot{x} - F_L(t) \tag{9.1}$$

Analogous calculations can be done in the y and z directions as well. In (9.1), the Langevin force $F_L(t)$ is not known, so it acts as a statistical uncertainty of the force calculation. In the case of a repeatable experiment (which is not always the case), the Langevin force contribution can be reduced by averaging.

The position of a trapped bead can be controlled using feedback as shown in Figure 9.2. The *regulator problem* is to design u to counteract the effects of the disturbances d, whereas the *servo problem* is to design u to make the output y track some reference signal r [60]. In both cases, we want the actual *position (tracking) error*,

$$e_* := x - r, \tag{9.2}$$

to be small. Note that, since y is the measured output, not the actual state x (position), we distinguish between the actual position error $e_* := x - r$ and the the measured position error $e := y - r$.

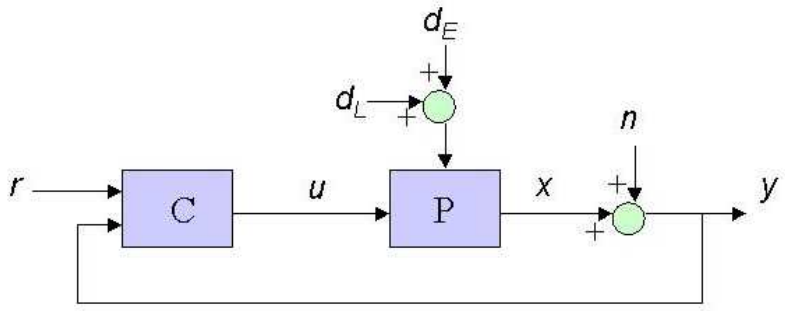

Figure 9.2: Two degrees-of-freedom feedback loop for position control of plant P using controller C. Measured output y is bead position x plus measurement noise n; control signal u is trap position x_T; r is the reference input; d_L is the Langevin disturbance; and d_E is the external disturbance.

Although *LabVIEW* software has built-in routines for PID control, it is also compatible with C-based compilers and *MATLAB*, so more sophisticated control techniques can be implemented if necessary. Due to delays in the Windows NT operating system, standard *LabVIEW*-based feedback control algorithms will have a bandwidth of less than 1 kHz, but for applications which require control at a rate greater than 1 kHz, analog circuitry (operational amplifiers) can be used to achieve faster control. For fast, deterministic control using a PC, *LabVIEW* Real-Time (RT) software, *d-space* software, or a programmable Digital Signal Processing (DSP) board could be used, but these are not currently available in our laboratory. Therefore, the control algorithms presented in this chapter have been studied using computer simulations. A comprehensive experimental verification of controller performance would require sophisticated real-time image processing and video feedback, which is currently unavailable in our laboratory.

Furthermore, single-axis feedback can cause instability [10]. This can be understood by referring to Figure 3.4. For feedback along a single (fixed) axis, large gains will drive the trapped particle to regions with reduced stiffness in the orthogonal direction. As a result, the particle will escape the trap. Hence, for feedback with high gains, feedback control must be implemented using two AOD's. However, this does not change our analysis method, which assumes the position coordinate x denotes radial displacement. In practice, identical controllers should be used in both lateral directions.

As an example of performance improvements due to feedback control, Molloy et al. were able to clamp a bead into position within 1 nm or so, a significant reduction from the 40-50 nm peak-to-peak deflections associated with Brownian motion [61]. Simmons et al. used feedback control to increase the effective stiffness of their optical traps by a factor of ~ 400 [10].

9.1 PI Control

For a first order plant, PI control is one of the most straightforward and commonly used control strategies. In this section, we will describe the design of PI control with pure error feedback, which is the simplest configuration. We use the one degree-of-freedom control configuration with pure error feedback (i.e., without feedforward gain), shown in Figure 9.3, in which measured

error $e := r - y$.

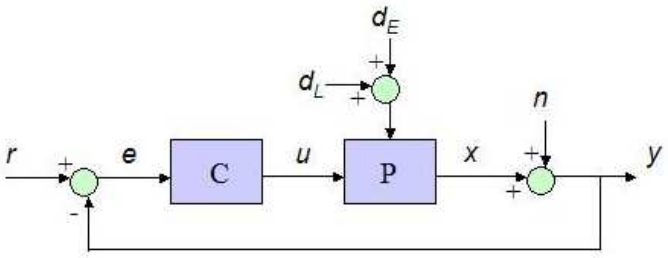

Figure 9.3: One degree-of-freedom feedback loop for position control of plant P using controller C.

According to the linear analysis from Section 3.2.2, if we denote the Laplace transforms of x, y, u, d, n, r by X, Y, U, D, N, R, respectively, we can use simple algebraic relations to express the transfer functions between inputs ond outputs as follows:

$$X = \frac{P}{1+PC}\frac{1}{\alpha}D - \frac{PC}{1+PC}N + \frac{PC}{1+PC}R \tag{9.3}$$

$$Y = \frac{P}{1+PC}\frac{1}{\alpha}D + \frac{1}{1+PC}N + \frac{PC}{1+PC}R \tag{9.4}$$

$$U = -\frac{PC}{1+PC}\frac{1}{\alpha}D - \frac{C}{1+PC}N + \frac{C}{1+PC}R, \tag{9.5}$$

in which P denotes the plant transfer function from u to y and C denotes the controller transfer function from e to u. For convenience, we have omitted the Laplace frequency index s in the above expressions.

The system is completely characterized by four transfer functions, known as the "Gang of Four" [62]. The Gang of Four is comprised of the complementary sensitivity function $T = \frac{PC}{1+PC}$, the sensitivity function $S = \frac{1}{1+PC}$, the load disturbance (input) sensitivity function $\frac{P}{1+PC}$, and the noise (output) sensitivity function $\frac{C}{1+PC}$ [62]. Since we are interested in regulating the position to zero, we set $r = 0$, and we can ignore the sensitivity function. For PI control of a first order plant (noninertial plant), we can write the plant and controller transfer functions as:

$$P = \frac{\frac{\alpha}{\beta}}{s + \frac{\alpha}{\beta}} \tag{9.6}$$

$$C = k_p + \frac{k_i}{s}, \tag{9.7}$$

which yield the following expressions for the transfer functions of interest:

$$\frac{PC}{1+PC} = \frac{\frac{\alpha}{\beta}s + \frac{\alpha}{\beta}k_i}{s^2 + \frac{\alpha}{\beta}(k_p+1)s + \frac{\alpha}{\beta}k_i} \tag{9.8}$$

$$\frac{P}{1+PC} = \frac{\frac{\alpha}{\beta}s}{s^2 + \frac{\alpha}{\beta}(k_p+1)s + \frac{\alpha}{\beta}k_i} \tag{9.9}$$

$$\frac{C}{1+PC} = \frac{k_p s^2 + (\frac{\alpha}{\beta}k_p + k_i)s + \frac{\alpha}{\beta}k_i}{s^2 + \frac{\alpha}{\beta}(k_p+1)s + \frac{\alpha}{\beta}k_i}. \tag{9.10}$$

If we ignore external forces and assume the fluid is stationary, both the Langevin disturbance $d = d_L$ and the measurement noise n can be modeled as white noise. In particular, we can denote $d = N(0, \sigma_d^2)$ and $n = N(0, \sigma_n^2)$. In this case, the expected value of the output signals can be computed from the transfer function coefficients using a contour integration technique described in [34]. The only requirement for this method is that the corresponding transfer function of the form

$$G(s) = \frac{B(s)}{A(s)} = \frac{b_1 s + b_2}{a_0 s^2 + a_1 s + a_2} \tag{9.11}$$

is strictly stable. That is, the poles must all be in the open left-half plane and the numerator polynomial $B(s)$ must be at least one degree less than the denominator polynomial $A(s)$ [34]. Substituting (9.9) and (9.8) into (9.3) for $r = 0$, we can write

$$X = \frac{\frac{1}{\beta}\sigma_d s}{s^2 + \frac{\alpha}{\beta}(k_p + 1)s + \frac{\alpha}{\beta}k_i} E_d - \frac{\frac{\alpha}{\beta}\sigma_n s + \frac{\alpha}{\beta}k_i\sigma_n}{s^2 + \frac{\alpha}{\beta}(k_p + 1)s + \frac{\alpha}{\beta}k_i} E_n. \tag{9.12}$$

For our second order ($n = 2$) closed loop transfer function (9.11), we use the prescription from [34] to form the following array:

$$\begin{array}{ccccc} a_0^{(2)} & a_1^{(2)} & a_2^{(2)} & b_1^{(2)} & b_2^{(2)} \\ a_1^{(2)} & 0 & 0 & a_1^{(2)} & 0 \\ & a_0^{(1)} & a_1^{(1)} & & b_1^{(1)} \\ & a_1^{(1)} & 0 & & \\ & & a_0^{(0)} & & \end{array} \tag{9.13}$$

in which the values of the entries[1] are given by

$$\begin{array}{ll} a_0^{(2)} = 1 & b_1^{(2)} = b_1 \\ a_1^{(2)} = a_1 & b_2^{(2)} = b_2 \\ a_2^{(2)} = a_2 & b_1^{(1)} = b_2 \\ a_0^{(1)} = a_1 & \\ a_1^{(1)} = a_2 & \\ a_0^{(0)} = a_2 & \end{array} \tag{9.14}$$

and the recursive pivot values are given by

$$\begin{array}{ll} \alpha_2 = \frac{1}{a_1} & \beta_2 = \frac{b_1}{a_1} \\ \alpha_1 = \frac{a_1}{a_2} & \beta_1 = \frac{b_2}{a_2}. \end{array} \tag{9.15}$$

For a given transfer function, the output variance for input white noise with unit variance is given by the integral:

$$I = \sum_{k=1}^{2} \frac{\beta_k^2}{2\alpha_k} = \frac{1}{2a_1 a_2}(b_2^2 + b_1^2 a_2), \tag{9.16}$$

[34]. Comparing coefficients in (9.12) and (9.11) and substituting into (9.16), we can show that

$$Ex^2 = I_x = \frac{\sigma_d^2 + \alpha(\alpha k_p^2 + \beta k_i)\sigma_n^2}{2\alpha\beta(1 + k_p)}, \tag{9.17}$$

[1]The formula for calculating $b_i^{(k-1)}$ in [34] contains a typographical error on page 138: the formulas for i odd and i even should be interchanged.

in which we require $k_p > -1$ and $k_i \geq 0$ for stability. The partial derivatives with respect to the controller gains are:

$$\frac{\partial I}{\partial k_i} = \frac{\sigma_n^2}{2(1+k_p)} > 0 \tag{9.18}$$

$$\frac{\partial I}{\partial k_p} = \frac{\alpha^2\sigma_n^2 k_p^2 + 2\alpha^2\sigma_n^2 k_p - (\sigma_d^2 + \alpha\beta k_i \sigma_n^2)}{2\alpha\beta}. \tag{9.19}$$

The partial derivative (9.18) is always positive, so position variance is minimized with respect to integral gain by choosing $k_i = 0$, which implies pure proportional control. Setting the partial derivative (9.19) equal to zero, we can show that I_x has a minimum at

$$(k_p)_{\text{opt}} := \arg\min_{k_p} \; I_x = \sqrt{1 + \frac{\sigma_d^2}{\alpha^2\sigma_n^2} + \frac{\beta}{\alpha}k_i} - 1. \tag{9.20}$$

Similarly, Substituting (9.9) and (9.8) into (9.3) for $r = 0$, we can write

$$U = \frac{\frac{1}{\beta}k_p\sigma_d s - \frac{1}{\beta}k_i\sigma_n}{s^2 + \frac{\alpha}{\beta}(k_p+1)s + \frac{\alpha}{\beta}k_i}E_d + \left[-k_p\sigma_n + \frac{(k_p^2\frac{\alpha}{\beta} - k_i)s + (k_p-1)k_i\frac{\alpha}{\beta}}{s^2 + \frac{\alpha}{\beta}(k_p+1)s + \frac{\alpha}{\beta}k_i}\right]E_n. \tag{9.21}$$

Comparing coefficients in (9.21) and (9.11) and substituting into (9.16), we can show that

$$Eu^2 = I_u = \frac{(k_i + k_p^2\frac{\alpha}{\beta})\sigma_d^2 + \left[(k_p-1)^2 k_i\alpha^2 + (k_p^2\frac{\alpha}{\beta} - k_i)\alpha\beta\right]\sigma_n^2}{2\alpha^2(1+k_p)} + k_p^2\sigma_n^2. \tag{9.22}$$

Figure 9.4 shows the theoretical position and control variance using PI Control for a linear trapping force assuming $\alpha = 10$ pN/μm and $\beta = 0.01$ pNs/μm. Assuming the Langevin force and measurement noise are modeled as band-limited white noise with power spectra $S_L^+ = 1.6\times10^{-4}$ pN^2/Hz and $S_n^+ = 2\times10^{-10}\mu$m^2/Hz, respectively, we obtain $\sigma_d^2 = 8\times10^{-5}$ pN^2 and $\sigma_n^2 = 1\times10^{-10}$ μm^2, according to (4.11). According to (9.20), the optimal proportional gain is $k_p = 88.4$, which results in a variance of $\sigma_x^2 = 8.84\times10^{-6}$ μm^2, which corresponds to a standard deviation of $\sigma_x = 0.003$ μm. The (open loop) variance of 4×10^{-4} μm^2 has been decreased by a factor of 45.2. However, the standard deviation of the control is just under $\sigma_u = 0.3$ μm, which is outside of the linear trapping region. The right plots show that both position and control variances increase with k_i, which confirms that integral control is counter-productive for the white noise inputs under consideration. However, the top right figure shows that σ_x is relatively insensitive to k_i, whereas the bottom right figure shows that σ_u increases considerably with k_i for small k_p.

Substituting $\sigma_d^2 = 2\beta k_B T$ from (4.11), we can express (9.17), (9.22), and (9.20) in terms of α, β, T and σ_n^2:

$$Ex^2 = \frac{2\beta k_B T + \alpha(\alpha k_p^2 + \beta k_i)\sigma_n^2}{2\alpha\beta(1+k_p)} \tag{9.23}$$

$$Eu^2 = \frac{(k_i\beta + k_p^2\alpha)2k_B T + \left[(k_p-1)^2 k_i\alpha^2 + (k_p^2\frac{\alpha}{\beta} - k_i)\alpha\beta\right]\sigma_n^2}{2\alpha^2(1+k_p)} + k_p^2\sigma_n^2 \tag{9.24}$$

$$(k_p)_{\text{opt}} = \sqrt{1 + \frac{\beta}{\alpha}\left(\frac{2k_B T}{\alpha\sigma_n^2} + k_i\right)} - 1. \tag{9.25}$$

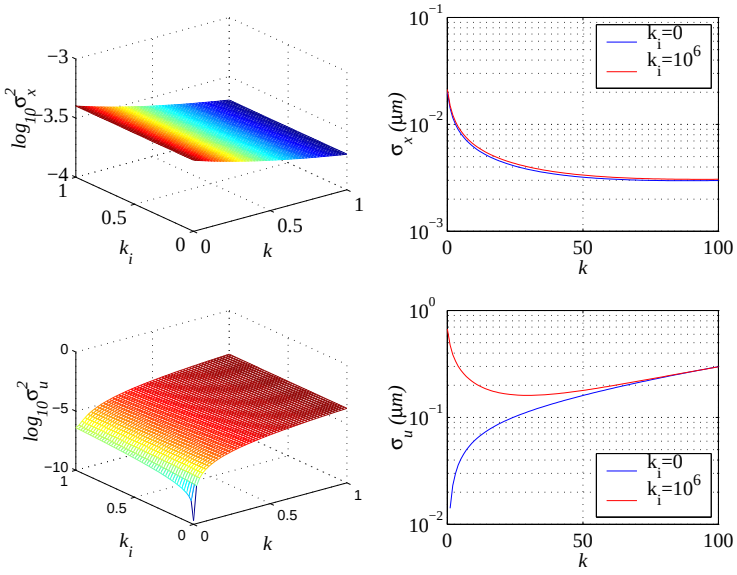

Figure 9.4: Theoretical variance using PI Control for linear trapping force assuming $\alpha = 10$ pN/μm, $\beta = 0.01$ pNs/μm ($\sigma_d^2 = 8 \times 10^{-5}$ pN^2), and $\sigma_n^2 = 1 \times 10^{-10}$ μm^2. Top plots correspond to position x; bottom plots correspond to control $u := x_T$. Left plots show variance; right plots show standard deviation.

The practical tradeoffs that can be expected for different proportional control gains are shown in Figure 9.5 [2]. The left figure shows position standard deviation and the right figure shows maximum absolute position (infinite norm). Results are shown for both the linear force and for the cubic force. In the nonlinear case, position variance decreases until about $k_p = 35$, gradually increases between $35 < k_p < 40$, and dramatically increases for $k_p \geq 40$. Up to $k_p \approx 40$, the net effect of the controller is to increase the effective stiffness of the trap. For $k_p = 35$, the variance is 1.36×10^{-5} μm^2, which is approximately 29 times smaller than the open loop variance of 4×10^{-4} μm^2. For the minimum variance near $k_p = 35$, the particle has a maximum excursion that is slightly beyond the trapping radius, according to the right figure. For values of k_p greater than approximately 30, the particle has excursions outside of the trapping radius of 0.675 μm, which results in an occasional absence of trapping force and a corresponding increase in variance. As k_p is further increased, the relative position develops larger excursions outside of the trapping radius until it eventually escapes from the trap, resulting in very large position variance. Such excursions are a result of the proportional controller being too aggressive because it is not designed to handle the nonlinear trapping force. For the linear trapping force, both variance and maximum absolute position display minima near $k_p \approx 100$, which agrees with our theoretical analysis. The drop in variance and absolute position for very high gains is due to the limited bandwidth of the nonlinear system. As the gain is increased, the controller attempts to move the particle at very high velocities (frequencies), which are beyond the system's capabilities. The system behaves like a lowpass filter for high gains.

Figure 9.6 shows the performance of the proportional controller for only a linear force model. Clearly, both variance and position have minima near $k_p = 100$. Due to the measurement noise, both variance and position increase for very large gains. For $k_p = 100$, the variance is 7.61×10^{-6} μm^2, which is approximately 49 times smaller than the open loop variance of

[2] All variance values from the simulations have been normalized to conform with the Equipartition theorem.

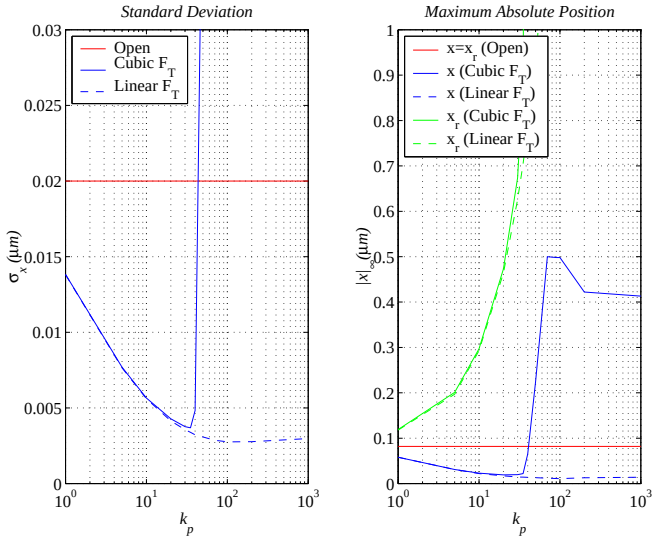

Figure 9.5: Comparison of proportional controller performance using computer simulations. Left figure shows position standard deviation; right figure shows maximum absolute position. Solid lines correspond to cubic trapping force; dashed lines correspond to linear trapping force. Simulations assume $\alpha_1 = 10$ pN/μm; $\alpha_3 = 22$ pN/μm^3 (nonlinear case) and $\alpha_3 = 0$ (linear case); $\beta = 0.01$ pNs/μm; and sampling time 0.01 ms. For the cubic trapping force, variance has a minimum near $k_p = 35$, at which the particle has a maximum excursion that is slightly beyond the trapping radius.

4×10^{-4} μm^2. The maximum position tends toward $|x|_\infty = 0.011$ μm, which is about 7.5 times smaller than the corresponding open loop value of $|x|_\infty = 0.082$ μm.

We can use the stochastic analysis of Chapter 3 to quantify the first mean exit time of a trapped particle within the linear region. From the equipartition theorem, in the absence of feedback control, , for $\alpha = 10$ pN/μm, particle position has a standard deviation of 20 nm. By setting $u = -k_p x$ in (4.13), and neglecting measurement noise, we can re-write the equation of motion as a stochastic differential equation in which

$$f(x) = \rho \frac{\psi(x)}{\beta}\big[-\alpha x(1+k_p)\big] \tag{9.26}$$

$$\sigma^2 = \frac{2k_B T}{\beta}. \tag{9.27}$$

Using the same procedure from Section 4.4.2, we can use (9.26) and (9.27) to solve for the mean first exit times from the $\pm$ 20 nm region. The results are shown in Figure 9.7. Clearly, increasing proportional gain increases the exit times, but it should be remembered that these results do not account for measurement noise.

9.2 LQG Control

Defining ω_d and ω_n as disturbance noise and measurement noise respectively, we can re-express (3.23) in state space form as

$$\begin{aligned} \dot{x} &= Ax + Bu + \omega_d \\ y &= Cx + \omega_n, \end{aligned} \tag{9.28}$$

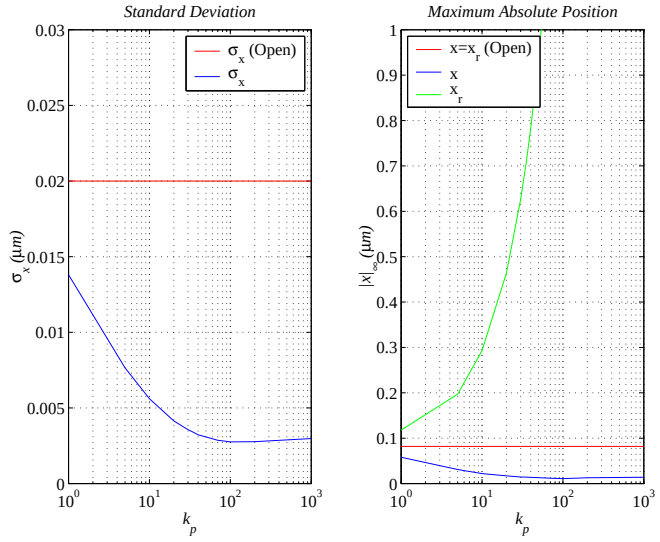

Figure 9.6: Simulation of proportional controller performance for linear trapping force. Simulations assume $\alpha_1 = 10$ pN/μm, $\alpha_3 = 0$, $\beta = 0.01$ pNs/μm, and sampling time 0.01 ms. Both variance and maximum absolute position have minima near $k_p = 100$.

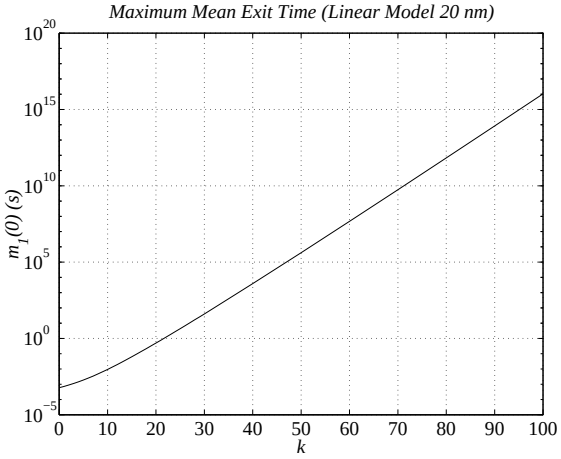

Figure 9.7: Maximum mean exit time from $\pm$ 20 nm as a function of proportional gain k_p. Trapping force is linear; laser power factor is $\rho = 1$ (100 mW at the focus).

where $A := -\frac{\alpha}{\beta} = -\omega_c$, $B := \frac{\alpha}{\beta} = \omega_c$, $C := 1$, and input disturbance noise $\omega_d := \frac{F_L}{\beta}$.

As shown in Figure 9.8, this system is suitable for the implementa

$$\begin{aligned} E\{\omega_d(t)\omega_d(\tau)\} &= W\delta(t-\tau) \\ E\{\omega_n(t)\omega_n(\tau)\} &= V\delta(t-\tau) \\ E\{\omega_d(t)\omega_n(\tau)\} &= 0 \\ E\{\omega_n(t)\omega_d(\tau)\} &= 0. \end{aligned}$$

The LQG control problem is to find the optimal control $u(t)$ which minimizes the integral cost

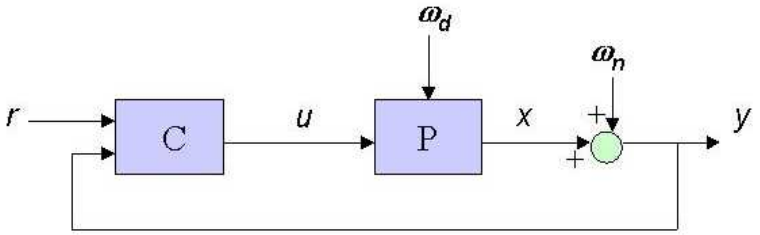

Figure 9.8: Feedback loop for LQG control. For stabilization about the origin, we set $r = 0$.

function

$$J = E\left\{\lim_{T\to\infty}\frac{1}{T}\int_0^T [x^T Q x + u^T R u]dt,\right\} \tag{9.29}$$

in which $Q = Q^T \geq 0$ and $R = R^T > 0$ are design parameters [60]. According to the Separation Theorem, the solution to the LQG problem is given by first solving the deterministic linear quadratic regulator (LQR) problem and then using a Kalman filter to obtain the optimal estimate $\widehat{x}$ of the state x such that $E\{[x-\widehat{x}]^T[x-\widehat{x}]\}$ is minimized [60]. The LQR problem is equivalent to solving the above LQG problem with no noise ($\omega_d = \omega_n = 0$). The LQR problem has a simple solution given by

$$u(t) = -K_r x(t), \tag{9.30}$$

where

$$K_r = R^{-1}B^T X, \tag{9.31}$$

in which $X = X^T \geq 0$ is the unique positive-semidefinite solution of the algebraic Riccati equation

$$A^T X + XA - XBR^{-1}B^T X + Q = 0. \tag{9.32}$$

The optimal estimate $\widehat{x}$ is obtained using a Kalman filter that is independent of Q and R. The solution to the LQG problem is then obtained by replacing x with $\widehat{x}$. The Kalman filter has the structure of an ordinary state-observer:

$$\begin{aligned}\dot{\widehat{x}} &= A\widehat{x} + Bu + K_f(y - C\widehat{x})\\ y &= \widehat{x},\end{aligned}$$

where the optimal choice of K_f is given by

$$K_f = YC^T V^{-1}, \tag{9.33}$$

in which $Y = Y^T \geq 0$ is the unique positive-semidefinite solution of the algebraic Riccati equation

$$YA^T + AY - YC^T V^{-1} CY + W = 0. \tag{9.34}$$

By solving (9.31) and (9.32) for a first-order system and substituting the system parameters from (9.28), we can show that

$$\begin{aligned}K_r &= \frac{A}{B}\left[1 - \sqrt{1 + \frac{B^2 Q}{A^2 R}}\right]\\ &= \sqrt{1 + \frac{Q}{R}} - 1.\end{aligned} \tag{9.35}$$

Similarly, by solving (9.33) and (9.34) for a first-order system, we can show that

$$\begin{aligned} K_f &= \frac{A}{C}\left[1-\sqrt{1+\frac{C^2W}{A^2V}}\right] \\ &= \sqrt{\omega_c^2+\frac{W}{V}}-\omega_c. \end{aligned} \tag{9.36}$$

From (4.11) and (4.17), $W = \frac{2k_BT}{\beta}$, which, for a 1-μm bead is equal to $W = 0.8$ μm^2. According to Simmons et al., typical measurement noise is 3 nm peak-to-peak, or under 1 nm RMS for 5 kHz detector bandwidth [10]. This corresponds to $S_n^+ < 2\times10^{-10}$ μm^2/Hz, or $V < 1\times10^{-10}$ μm^2/Hz.

Figure 9.9 shows the results of applying LQG control for $\alpha_1 = 10$ pN/μm, $\alpha_3 = 22$ pN/μm^3 and $\beta = 0.01$ pNs/μm, where the nonlinear spring constants are from (3.2). Simulation sampling time is 0.01 ms and initial position is $x(0) = 0$. For the computer simulation, the Langevin force and measurement noise are modeled as band-limited white noise with power spectra $S_L^+ = 4\beta k_BT = 1.6\times10^{-4}$ pN^2/Hz and $S_n^+ = 2\times10^{-10}$ μm^2/Hz, respectively. Correspondingly, by setting $V = 1\times10^{-10}$ and $W = 0.8$ in (9.36), we obtain Kalman filter gain $K_f = 8.84\times10^4$. By setting $Q = 3000$ and $R = 1$ in (9.35), we obtain LQR gain $K_r = 53.8$.

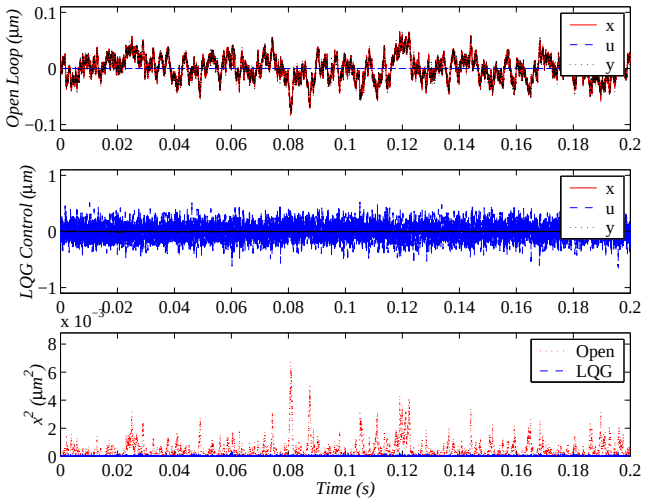

Figure 9.9: Simulation of LQG control for system parameters $\alpha_1 = 10$ pN/μm, $\alpha_3 = 22$ pN/μm^3, $\beta = 0.01$ pNs/μm and LQG weights $Q = 3000$ and $R = 1$, and sampling time 0.01 ms. The controller reduces position variance by a factor of ~ 27.

Clearly, the LQG controller significantly reduces position fluctuations due to thermal noise. The (open loop) variance of 4×10^{-4} μm^2 is decreased by a factor of approximately 27. Note that the optimal LQR gain $K_r \approx 54$ is greater than the optimal proportional control gain $k_p \approx 35$ because the Kalman filter is an optimal estimator. Figure 9.10 shows the results of applying LQG control for the same parameters used in Figure 9.9, but with a higher weight of $Q = 10000$, which increases the LQR gain to $K_r = 99$. The controller is too aggressive because it assumes a linear trap model. As a result, the particle is driven outside the trapping radius.

The tradeoffs associated with different cost function weights are shown in Figure 9.11 [3]. The left figure shows the position standard deviation and the right figure shows maximum absolute

[3] All variance values from the simulations have been normalized to conform with the Equipartition theorem.

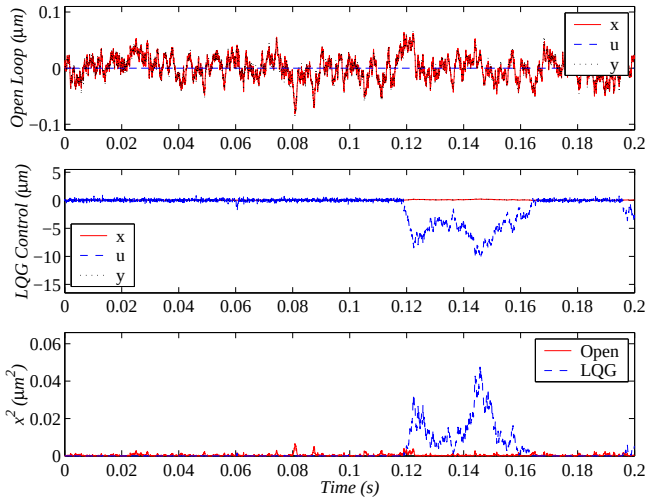

Figure 9.10: Simulation of LQG control for system parameters $\alpha_1 = 10$ pN/μm, $\alpha_3 = 22$ pN/μm^3, $\beta = 0.01$ pNs/μm and LQG weights $Q = 10000$ and $R = 1$, and sampling time 0.01 ms. The controller is too aggressive and drives the particle outside the trapping radius.

position (infinite norm). Results are shown for both the linear force model and for the cubic force model. In the nonlinear case, position variance decreases until about $\frac{Q}{R} = 3000$, gradually increases between $3000 < \frac{Q}{R} < 5000$, and dramatically increases for $\frac{Q}{R} > 5000$. The minimum variance near $\frac{Q}{R} = 3000$ is no coincidence as $|x_r|_\infty = 0.679$ μm, according to the right figure. For values of $\frac{Q}{R}$ greater than approximately 3000, the particle has significant excursions outside of the trapping radius of 0.675 μm, which results in frequent loss of trapping force and a corresponding increase in variance. As $\frac{Q}{R}$ is further increased, the relative position develops larger excursions outside of the trapping radius until it eventually escapes from the trap, resulting in very large position variance. Such excursions are a result of the LQG controller being too aggressive because it is not designed to handle the nonlinear trapping force. For the linear trapping force, both variance and maximum position decrease with $\frac{Q}{R}$, as expected.

Figure 9.12 shows the performance of the LQG controller for only a linear force model. Clearly, both variance and position decrease with $\frac{Q}{R}$ towards nonzero asymptotic values. Due to the non-zero measurement noise, neither the variance nor position tends to zero, even with very large gains. For $\frac{Q}{R} = 10^7$, the variance is 6.71×10^{-6} μm^2, which is approximately 60 times smaller than the open loop variance. The maximum position tends towards $|x|_\infty = 0.0114$ μm, which is about 7 times smaller than the corresponding open loop value of $|x|_\infty = 0.082$ μm.

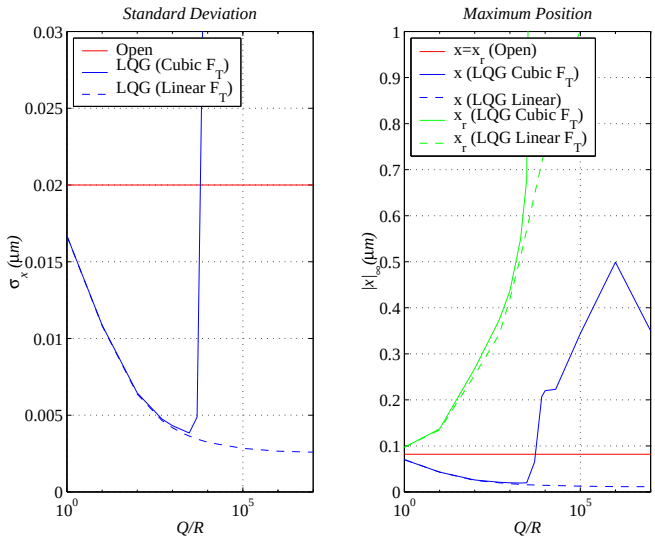

Figure 9.11: Comparison of LQG controller performance using computer simulations. Left figure shows position standard deviation; right figure shows maximum absolute position. Simulations assume $\alpha_1 = 10$ pN/μm, $\alpha_3 = 22$ pN/μm^3 (nonlinear case) and $\alpha_3 = 0$ (linear case), $\beta = 0.01$ pNs/μm, and sampling time 0.01 ms. For the nonlinear trapping force, variance has a minimum near $\frac{Q}{R} = 3000$, at which the particle displays slight excursions outside of the trapping radius.

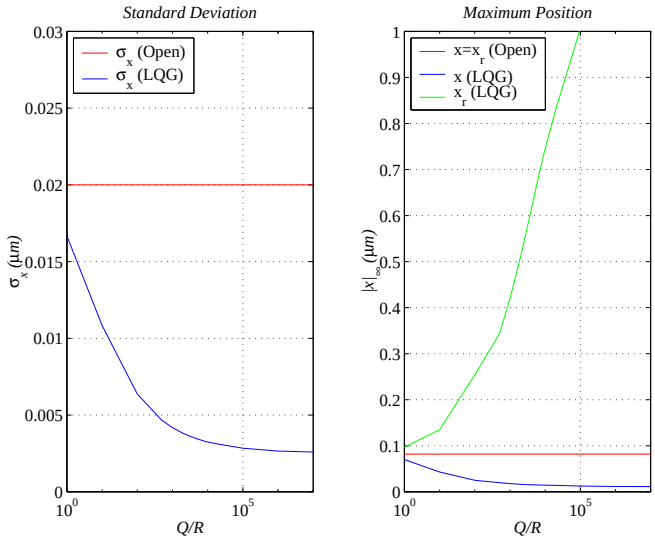

Figure 9.12: Simulation of LQG controller performance for linear trapping force. Simulations assume $\alpha_1 = 10$ pN/μm, $\alpha_3 = 0$, $\beta = 0.01$ pNs/μm, and sampling time 0.01 ms. Both variance and maximum absolute position decrease with $\frac{Q}{R}$ towards nonzero asymptotic lower bounds.

Chapter 10

Nonlinear Feedback Control

For small displacements from the center of the trap, a linear trapping force model is widely used to quantify forces acting on a trapped particle. As shown in Figure 3.3, the nonlinear trapping region of an optical tweezer is much larger than the linear trapping region. In this chapter, we develop nonlinear control algorithms that recognize and utilize our knowledge that the trapping force is, in fact, nonlinear for large relative displacements.

10.1 Stabilization using Hyperbolic Tangent[1]

In this section, we describe both linear control laws for asymptotic stabilization (AS) of the origin and nonlinear control laws for global asymptotic stabilization (GAS) of the origin. In Section 3.2.1, we showed that by defining the trap position as the control input, $u := x_T$, we can express our noninertial system in state space form as (3.16), which is reproduced below:

$$\begin{aligned} \dot{x} &= \frac{\psi(x-u)}{\beta}\left[\alpha_3(x-u)^3 - \alpha_1(x-u)\right] + \frac{1}{\beta}\left(F_L + F_E\right) \\ y &= x. \end{aligned} \tag{10.1}$$

In the remainder of this section, we will derive feedback control laws to stabilize the origin of the first order system described by (10.1) under the assumption of zero disturbance, $F_L(t) = F_E(t) = 0$. We will later include the Langevin disturbance and interpret it as a varying initial condition that requires asymptotic stabilization.

Asymptotic Stability

From (10.1), as long as the particle is not outside of the trapping radius R, the scalar system $\dot{x} = \frac{1}{\beta}F_T(x_r)$ will be stabilized by the trapping force $F_T(x_r)$. We will exploit the nature of this trapping force to stabilize the particle, even when it is initially outside of the trapping radius R. As shown in Figure 10.1, for an appropriate choice of $\mu > 0$ and $\lambda > 0$, the cubic trapping force, $F_T(x_r) = \alpha_3 x_r^3 - \alpha_1 x_r$ (from Figure 3.3), can be approximated by a hyperbolic tangent function $f_t(\cdot)$:

$$F_T(x_r) \approx f_t(x_r) = \mu \tanh(-\lambda x_r).$$

Although $F_T(x_r)$ behaves "like" $f_t(x_r)$ only within the maximum trapping force region, $|x_r| < R_F < R$, what is important for our derivation is that both functions exert a restoring

[1] Most of this section is excerpted from [63].

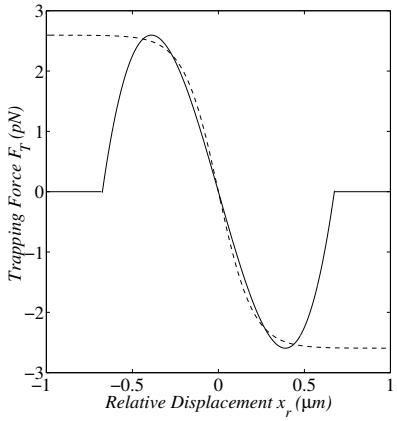

Figure 10.1: Approximation of cubic trapping force $F_T(x_r)$ (solid line) from Figure 3.3 using a hyperbolic tangent function $f_t(x_r)$ (dashed line) for $\mu = 2.595$ pN and $\lambda = 5$.

force within the trapping radius R. Therefore, we can apply a simplified version of the saturation analysis from [64]. Specifically, for any $p > 0$, we can choose a Lyapunov function $V(x) = px^2$ and set

$$\begin{aligned} -\lambda x_r &= -bpx, \\ x_r &= \frac{1}{\lambda} bpx, \end{aligned} \tag{10.2}$$

in which the control gain $b := \frac{1}{\beta} > 0$, according to (10.1). Then,

$$\begin{aligned} \dot{V}(x) &= \frac{dV}{dx}\frac{dx}{dt} \\ &= 2\mu bpx \tanh(-bpx) \\ &= -2\mu y \tanh(y) \leq 0, \end{aligned}$$

which shows that the origin of the x system is asymptotically stable in the domain $|x_r| < R$ [65]. Note that the proof only requires that μ be positive, so it is not necessary for the tanh function $f_t(x_r)$ to exactly match the force profile $F_T(x_r)$. What matters is that the restoring force for both functions is of the same sign, which is true within the trapping radius R. From (3.1) and (10.2), the asymptotically stabilizing linear feedback control law is given by

$$u = \left(1 - \frac{p}{\lambda\beta}\right) x. \tag{10.3}$$

The linear control algorithm given by (10.3) was simulated for system parameters $\beta = 0.01$ pNs/μm, $\alpha_3 = 22$ pN/μm^3, $\alpha_1 = 10$ pN/μm, $\lambda = 5$, and control parameter $p = 0.1$, as shown in the left columns of Figures 10.2, 10.3, and 10.4. According to (10.2), when $|x(0)| \geq \frac{\lambda\beta}{p}R$, $|x_r| \geq R = 0.675$ μm. The particle remains motionless ($\dot{x} = 0$), but away from the origin ($x \neq 0$) and out of the controller's reach (Figures 10.3 and 10.4). It follows that, for the chosen value of $p = 0.1$, the AS controller is asymptotically stable for $|x(0)| < \frac{\lambda\beta}{p}R = 0.3375$ μm. The basin of attraction can be increased by decreasing p, but this will result in a slower rate of convergence.

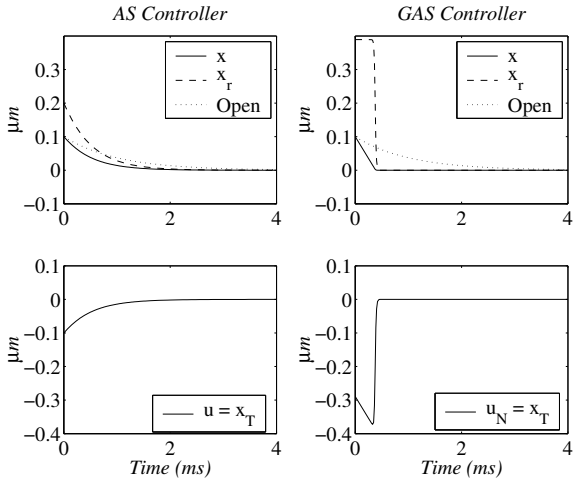

Figure 10.2: Simulation of non-inertial controllers with initial position within the linear region, $x(0) = 0.1$ μm. For comparison, the open loop position is shown as a dotted line. Left plots show linear AS controller; right plots show nonlinear GAS controller. The GAS controller ($p = 10$) achieves faster settling time than both the AS controller ($p = 0.1$) and the open loop system.

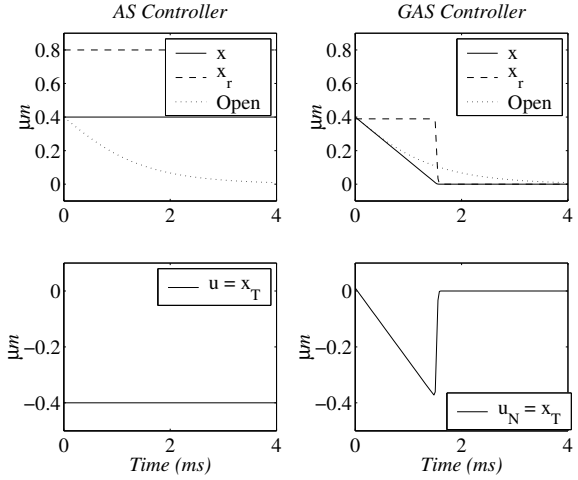

Figure 10.3: Simulation of non-inertial controllers with initial position within the nonlinear trapping region, $x(0) = 0.4$ μm. The AS controller ($p = 0.1$) does not achieve asymptotic stability because the control law drives the relative position outside of the trapping radius. The GAS controller ($p = 10$) achieves faster settling time than the open loop system.

Global Asymptotic Stability

To achieve global asymptotic stability (GAS), we suggest setting the relative position equal to a hyperbolic tangent function:

$$x_r = \omega \tanh\left(\frac{1}{\lambda} bpx\right), \tag{10.4}$$

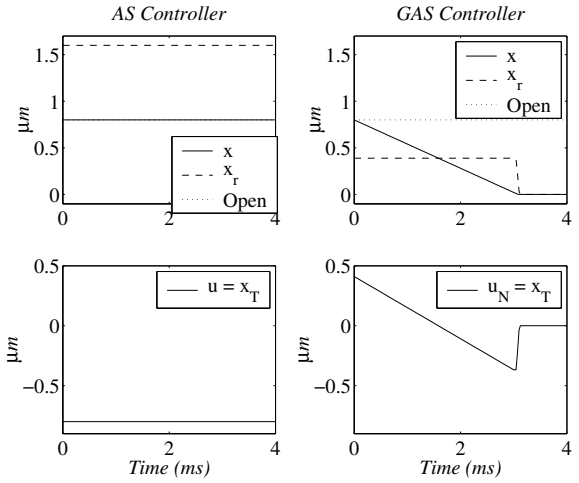

Figure 10.4: Simulation of non-inertial controllers with initial position outside of the trapping radius, $x(0) = 0.8$ μm. Only the GAS controller ($p = 10$) achieves asymptotic stability.

in which, $0 < \omega < R = 0.675$ μm. By choosing ω within this range, GAS is guaranteed because x_r will always exist within the region in which the nonlinear restoring force $F_T(x_r)$ is not zero (except at the origin). Furthermore, by picking $\omega = R_F = 0.3893$ μm, in addition to achieving GAS, the particle will also be driven into (restricted to) the region in which the nonlinear restoring force $F_T(x_r)$ is maximized. From (3.1) and (10.4), the globally asymptotically stabilizing nonlinear feedback control law u is given by

$$u = x - \omega \tanh\left(\frac{p}{\lambda\beta}x\right). \tag{10.5}$$

Using the same system parameters as in Section 10.1, the nonlinear control algorithm given by (10.5) was simulated for control parameters $p = 10$ and $\omega = 0.389$ μm, as shown in the right columns of Figures 10.2, 10.3, and 10.4. (In all three figures, the nonlinear control signal is denoted by u_N.) The figures show that the GAS controller achieves a faster settling time than both the open loop system and the AS controller. In each figure, it is clear that when the particle is far from the origin, the GAS controller drives the initial relative position to $|x_r| = R_F$, which we specified by our choice of ω. This results in the maximum possible restoring force and therefore, minimum settling time (for a given p). Once the particle has been brought closer to the origin, the relative position is driven towards zero according to the tanh function in (10.4).

As mentioned in Section 6.3, the trap position x_T is actuated using an AOD that has position resolution of better than 0.001 nm, a useful range of approximately 10 μm, and bandwidth on the order of several tens of kilohertz [36, 18]. Therefore, the control values shown in the figures lie well within the range of practically achievable trap dynamics.

The nonlinear control algorithms developed in this section can also be extended to inertial systems [63]. Details are included in Appendix C.

Effects of Disturbances and Noise

As mentioned in Section 3.2, in practice, a particle trapped in an optical tweezer is subject to an external Langevin force $F_L(t)$ with an average value of zero and a constant power spectrum given

by $S_L^+(f) = 4\beta k_B T$, which, for a 1-μm bead trapped at room temperature, is approximately 1.6×10^{-4} μm^2. Figure 10.5 shows a simulation of the performance of the non-inertial GAS controller (10.5) subject to external thermal noise. The simulation bandwidth of 100 kHz is sufficiently large that the band-limited white noise approximation approaches the behavior of ideal white noise. Clearly, the controller is very effective in reducing random position fluctuations (Brownian motion) due to thermal (Langevin) noise. The net effect of the controller is to increase the effective stiffness of the trap.

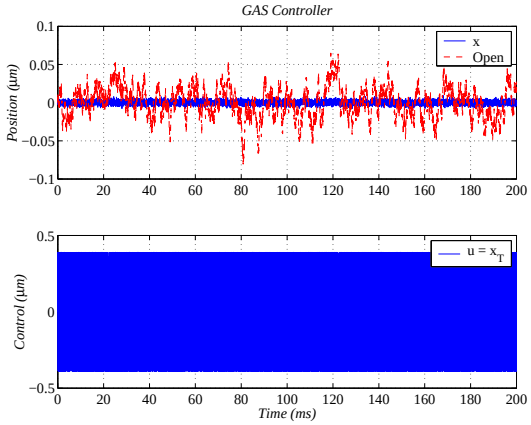

Figure 10.5: Simulation of non-inertial GAS controller subject to external thermal noise for $x(0) = 0$, $p = 10^4$, $\omega = 0.389$ and 100 kHz bandwidth. For comparison, open loop position is shown as a dotted line.

The non-inertial GAS controller is designed to provide global asymptotic stability to the origin assuming the external disturbance has an expected value of zero, as in the case of thermal noise. According to (3.15), a small constant external disturbance F_E will result in stabilization to some constant steady state value $\overline{x_r} \approx \frac{1}{\alpha_1} F_E$. Therefore, according to (10.4), the steady state position x_{ss} is given by

$$x_{ss} \approx \frac{\lambda\beta}{p} \tanh^{-1}\left(\frac{1}{\omega\alpha_1} F_E\right), \tag{10.6}$$

which can be greatly reduced by increasing p. For example, Figure 10.6 shows the performance of the non-inertial GAS controller (10.5) subject to external thermal noise and a constant external disturbance of 1 pN. Clearly, the GAS controller is very effective in stabilizing the origin, even with the constant disturbance. According to (10.6), the steady state position error is 0.0013 nm. In theory, the maximum constant disturbance that the controller can reject is slightly less than the maximum restoring force, which is 2.595 pN for this system, according to Figure 3.3. A more thorough treatment of constant disturbance rejection would require integral feedback, but we will not investigate that in this dissertation.

In practice, position sensors have measurement noise, which imposes a finite upper limit on the gain p. As mentioned in the previous chapter, a typical noise value is $S_n^+ = 2 \times 10^{-10}$ μm^2/Hz. The tradeoffs associated with different nonlinear control gains p are shown in Figure 10.7 [2]. The left figure shows position standard deviation and the right figure shows maximum absolute position (infinite norm). Results are shown for both the linear force and for the cubic force. For the cubic trapping force, position variance decreases until about $p = 10^5$

[2] All variance values from the simulations have been normalized to conform with the Equipartition theorem.

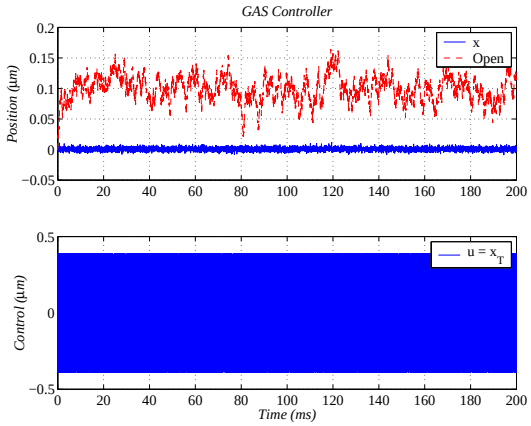

Figure 10.6: Simulation of non-inertial GAS controller subject to external thermal noise and a constant disturbance of 1 pN for $x(0) = 0$, $p = 10^4$, $\omega = 0.389$ and 100 kHz bandwidth.

and gradually increases for larger p. For $p = 10^5$, the variance is 6.18×10^{-6} μm^2, which is over 64 times smaller than the open loop variance of 4×10^{-4} μm^2. It is clear from Figure 10.7 that the hyperbolic tangent controller has superior performance for the linear trapping force (compared to the cubic trapping force) up to about $p = 10^4$. This is because the magnitude of the linear restoring force is always greater than the cubic force (except at the origin, where they are equal), as shown in Figure 3.5. After $p \approx 10^4$, the maximum relative position for the linear trapping force hits the maximum force radius of $R_F = 0.3893$ μm. Thereafter, the marginal benefits of increasing p begin to diminish because the particle is prevented from moving beyond R_F.

10.2 Discussion

In this chapter, we described the global asymptotic stabilization of a spherical particle trapped in an optical tweezer. For the non-inertial system model, which is well-suited for practical implementation, we have obtained a nonlinear control law that achieves not only GAS, but also a faster settling time than the open loop system. Global asymptotic stabilization is important in biological or micro-mixing experiments in which a located particle needs to be moved to a very specific location. We have also shown that the non-inertial GAS controller is very effective in reducing random position fluctuations due to thermal noise.

We have not implemented the control algorithms described in this chapter. Since the photodetectors used to detect particle position in our experimental setup cannot efficiently detect relative displacements of greater than approximately 1 μm, we will not be able to investigate global stability of the controllers. However, the local asymptotic stabilization properties of the controllers can be investigated within a range of ± 0.5 μm of the origin. A comprehensive experimental verification of GAS would require sophisticated real-time image processing and video feedback, which is currently unavailable in our laboratory.

For a practical optical tweezer system, the inertial controllers derived in Appendix C are unnecessarily complicated because the trappable mass is tiny. However, these controllers will prove useful in the future when the laser technology behind optical tweezers evolves such that larger masses can be trapped. The inertial analysis outlines a general method to obtain a GAS controller for any system that has the inertial equation of motion given by (3.11). We have also derived asymptotically stabilizing linear controllers for both the inertial system model and

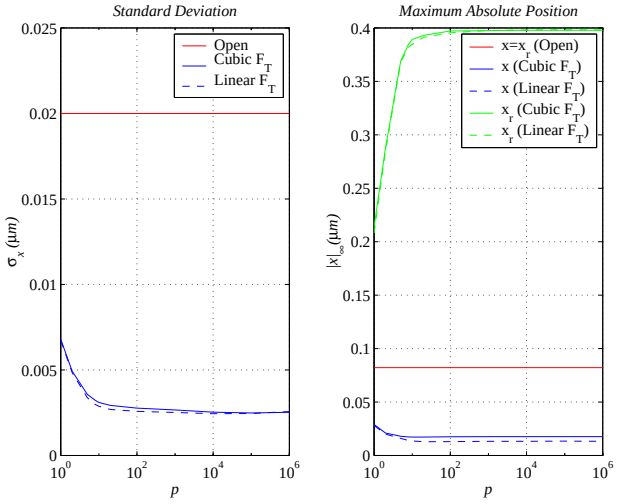

Figure 10.7: Comparison of nonlinear hyperbolic tangent controller performance according to computer simulations. Left figure shows position standard deviation; right figure shows maximum absolute position. Solid lines correspond to cubic trapping force; dashed lines correspond to linear trapping force. Simulations assume $\alpha_1 = 10$ pN/μm, $\alpha_3 = 22$ pN/μm^3 (nonlinear case) and $\alpha_3 = 0$ (linear case), $\beta = 0.01$ pNs/μm, and sampling time 0.01 ms. For the nonlinear trapping force, variance has a minimum near $p = 10^5$.

the noninertial system model. Although these linear AS controllers have a limited basin of attraction, they are easier to implement than the nonlinear GAS controllers.

Although our system can also be controlled by feedback linearization, such a feedback method would not be effective beyond the maximum trapping force region [65]. Furthermore, the feedback control would require an extremely accurate model of the trapping force, which implies that it would not be robust with respect to parameter variations or changes in the trapping force. Therefore, feedback linearization is not a useful control option for this system.

For almost a decade, the linear trapping behavior of optical tweezers has been used to quantify forces acting on a trapped particle for small displacements from the center of the trap. For the most part, the nonlinear trapping region has not been used quantitatively, except to obtain a rough estimate of the maximum trapping force [18]. The control laws presented in this chapter represent an attempt to quantitatively exploit the entire nonlinear profile of the restoring force of an optical tweezer. As shown in Figure 3.3, the nonlinear trapping region for a 1-μm polystyrene bead is approximately three times as large as the linear region. Therefore, it is our hope that the algorithms described in this chapter will be of value to the many users of optical tweezers.

Chapter 11

Conclusion

As mentioned in the Introduction, the main purpose of this dissertation is to analyze the properties of an optical tweezer from a control engineering point of view. In this final chapter, I summarize my main results and contributions.

Modeling

In Chapters 2 and 3, I provided a basic introduction to the dynamic behavior of optical traps. By characterizing their properties using terminology from control engineering, I have provided mathematical descriptions that should be accessible to anyone interested in studying optical traps in greater depth. In particular, the use of a cubic trapping force model enables the derivation of analytic expressions.

Stochastic Analysis

In Chapter 4, I developed stochastic differential equations that enable computation of probability density functions and exit times. For a given optical tweezer configuration, the first exit time is an extremely useful measure of trapping capability because it quantifies the time horizon during which experiments can be conducted before trapped particles are lost. It is especially important to use lower power levels when studying biological samples to avoid damaging them with heat; furthermore, in applications in which a single laser beam is time-shared to trap many particles, it is important to quantify low power trapping capabilities. Published information about minimum power levels are based on experimental observations; for example, Smith et al. observes that "polystyrene spheres could be trapped with powers at the back of the objective as small as 5 mW" [12]. The theoretical framework I have developed can be used to verify such statements and also quantify the trapping capabilities for various power levels.

We show that the first mean exit time for a given trapping force model can be computed numerically. We calculated values for a 1-μm diameter polystyrene bead trapped in water at biological temperature; in particular, for laser powers of greater than approximately 5 mW at the focus, the mean first escape time is extremely large, and unbounded for most practical purposes. We show that the maximum mean exit time increases exponentially with laser power. Using experimental data for a trapped, 9.61-μm bead, we calculated the mean first passage time and its standard deviation within the linear trapping region. The experimental value shows close agreement with theoretical calculations. Since the mean passage time is very sensitive to parameter values, it can (potentially) be used to verify the results of other calibration methods.

Construction

In Chapters 5 and 6, I described construction of the research-grade optical tweezer system in our laboratory. The system consists of a home-built microscope that is equipped with both video imaging and digital imaging. Incoming laser light is focused to a diffraction-limited spot using a 100×, 1.3 NA microscope objective. By splitting a single continuous-wave Nd:YAG laser beam according to polarization, I have created two independently steerable optical traps. One trap can be steered using a gimbal-mounted mirror with micrometers or DC motors and the other trap can be steered using an AOD driven by a 32-bit digital frequency synthesizer. The system is equipped with photodetectors that have been aligned to measure the lateral position of trapped beads relative to the laser focus (trap location). The optical tweezer system can be used for any number of scientific purposes. Additional modifications needed to customize or improve its capabilities are described in Appendix B and D.1.

Identification

In Chapter 7, I described off-line (batch) calibration methods that are in wide use in the biophysics community. In Chapter 8, I propose the use of on-line calibration to achieve faster and more up-to-date calibrations. By describing the sampled-data system using an ARX model, I was able to implement recursive least squares (RLS) estimation to calibrate the characteristic frequency of an optical tweezer. The parameter convergence values for different calibration methods are summarized in Table 11.1. All calibration results are for 30 seconds of data. The average of the estimates for the RLS method and step response method can be compared with the single estimate for the power spectrum. The off-line calibration methods suggest a value of $\omega_c = 120 \pm 1$ rad/s, while the RLS method suggests a value of 112.5 rad/s for the larger input amplitude. Clearly, the RLS estimation converges to a value that is between the low and high calibration values from the step response method. The average value of the RLS calibration underestimates the (average) off-line calibrations by almost 7%. Intuitively, this discrepancy between the average value of the estimates should not be surprising because we have not proved that each method will average the two (actual) characteristic frequency values in the same manner. All we can expect is that the average value is between the two actual values.

Calibration Method	Input	$\widehat{a}$	$\widehat{b}$	$\widehat{\omega}_c$	Time to Steady-state
RLS	Square (A = 0.15 μm)	112	113	112.5	9 s
RLS	Square (A = 0.05 μm)	105	114	110	19 s
Power Spectrum	None	N/A	N/A	119	N/A
Step Response	Square (A = 0.15 μm)	104	136	120	N/A
Step Response	Square (A = 0.10 μm)	107	135	121	N/A

Table 11.1: Comparison of estimates of characteristic frequency ω_c (rad/s) for experimental data for a trapped 9.61-μm polystyrene bead. Square wave inputs have frequency $f = 10$ Hz. For the step response method, parameter estimates $\widehat{a}$ and $\widehat{b}$ correspond to low data and high data respectively.

Calibration inconsistencies can arise due to other factors. Even slight misalignments in the position detection system and fluctuations in the dynamic laser pointing system (the AOD) can cause systematic errors that distort the RLS calibration results. The power spectrum method, in particular, is robust with respect to such factors [26, 18]. Additional sources of measurement noise, such as low-frequency drift and other types of electronic bias, high frequency amplifier noise, mechanical vibrations, and extraneous background light can also contribute to erroneous

estimates. Such problems are inherent in any practical position detection system. Soderstrom and Stoica make the following statement regarding system identification in practice:

> "It is sometimes claimed that system identification is more art than science. There are no foolproof methods that always and directly lead to a correct result. Instead, there are a number of theoretical results which are useful from a practical point of view. Even so, the user must combine the application of such a theory with common sense and intuition to get the most appropriate result." [54]

There are obvious tradeoffs associated with each calibration method. The power spectrum method is easiest to apply because it does not require an accurately calibrated position detector or input signal. Also, this method can reveal the existence of extraneous sources of noise within the laboratory environment. The step response method requires a calibrated position detector and an accurate square wave input. Furthermore, as demonstrated in Chapter 7, this method can be used to quantify both the high and low stiffnesses of an asymmetric trap. The step response method, is however, very sensitive to noise and measurement errors. The recursive least squares method has the potential to obtain much faster calibrations than the off-line methods. Computer simulation show that a well-aligned system can be calibrated within 2% in under 1 second using an RLS approach. Computer simulations shows that further improvements can be achieved by identification in closed loop. However, in practice, the RLS method requires a very well-calibrated position detector and an input signal. Slight offsets in the position detection system can cause significant calibration errors. For this reason, calibration using a PRBS was not successful for our system; for a square wave input, the alignment offset can be subtracted quite accurately. For practical implementation of the RLS method, an automatic tracking system is suggested for the position detector. This will minimize laser misalignments due to human error. Alternatively, a second laser beam can be used purely for position detection [18]. Like the power spectrum method, the RLS method cannot be used to obtain the different stiffnesses of an asymmetric trap. It should be mentioned that this dissertation mainly considers calibration of the characteristic frequency of an optical tweezer. If specific information about stiffness and drag are sought, the power spectrum method is unrivalled in many aspects [26]. As future work, we will investigate the possibility of using mean passage time data to roughly calibrate α and β and also verify the accuracy of position detector calibration.

Control

In Chapter 9 and 10, I discussed the performance of feedback controllers. In Chapter 9, I obtained analytic expressions for both PI controllers and LQG controllers that are designed to achieve linear position regulation. In Chapter 10, I derived a nonlinear controller that uses a hyperbolic tangent function to achieve global asymptotic stabilization (GAS) of the origin. The linear controllers are designed for a linear trapping force and the nonlinear controller is designed for a cubic trapping force. Computer simulations show that the linear controllers are effective for low gains because the particle does not leave the trapping radius. However, for high gains, the linear controllers are counter-productive because they drive the particle beyond the trapping radius. The nonlinear controller is effective for all gains because it is specifically designed to prevent the particle from leaving the trapping radius. In fact, we can choose the nonlinear controller parameters in such a way as to maximize the restoring force at all times. The performance of each controller is summarized in Table 11.2

For the cubic trapping model, the best performance of different controllers is illustrated and compared in Figures 11.1 and 11.2. For comparison, a proportional controller with saturation is also shown. The saturation function limits the over-reaction of the linear controllers; for analog control, saturation can be implemented quite easily using a Ziener diode. In the figure, the

Controller	Variance reduction factor	Maximum position reduction factor
Open loop	1	1
Proportional	29 (52)	4.3 (7.5)
LQG	27 (60)	4.2 (7.2)
Hyperbolic tangent	65 (67)	4.8 (6.3)

Table 11.2: Summary of controller performance according to computer simulations, assuming a cubic trapping force. Values in parenthesis correspond to a linear trapping force model. Listed properties are best performance values.

saturation level is set to $u = x_T = 0.389$ μm, which roughly limits the relative position to the maximum force radius R_F.

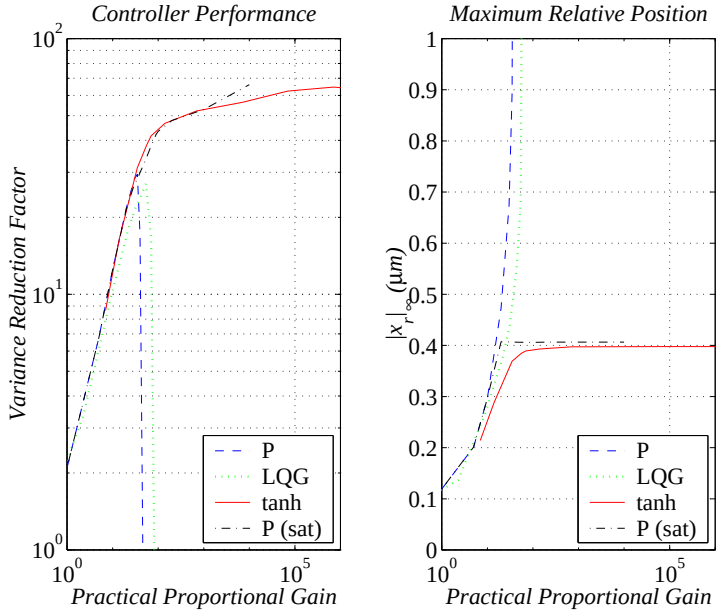

Figure 11.1: Comparison of controller performance according to computer simulations. Left figure shows position variance reduction compared to open loop; right figure shows maximum absolute relative position. Simulations assume $\alpha_1 = 10$ pN/μm, $\alpha_3 = 22$ pN/μm^3, $\beta = 0.01$ pNs/μm, and sampling time 0.01 ms.

All three controllers are capable of reducing the position variance significantly. The nonlinear hyperbolic tangent controller is superior to both the proportional controller and the LQG controller. For a linear trapping force, we expect the LQG controller to provide position variance properties that are superior to the proportional controller because the former uses a Kalman filter to obtain position estimates that are optimal according to a variance criterion; however, for the cubic trapping force model, the Kalman filter is no longer optimal and the controller performance is degraded. Although the nonlinear controller provides exceptional performance, the proportional controller with saturation provides equally effective, if not better, performance. In practice, if PI control works well-enough, there is usually no need to replace it because it is easiest to implement. At the 2004 American Control Conference, Peter Schmidt of Rockwell Au-

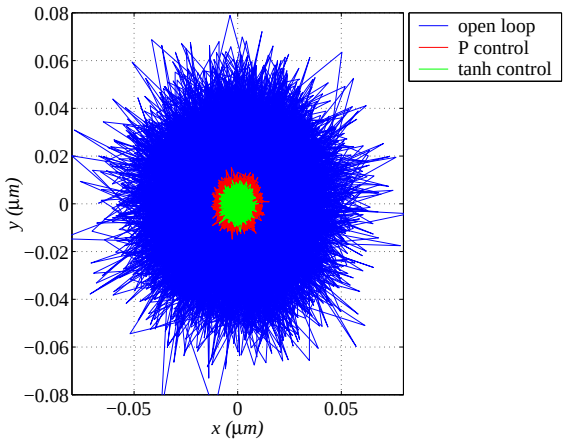

Figure 11.2: Plot of particle position for different controllers according to computer simulations. Position fluctuations correspond to the optimal gain for each controller. Simulations assume $\alpha_1 = 10$ pN/μm, $\alpha_3 = 22$ pN/μm^3, $\beta = 0.01$ pNs/μm, and sampling time 0.01 ms.

tomation made the following statement during an invited tutorial session titled "Theory versus Practice Forum":

> "Industry is slow to replace a solution that works 90-95% of the time. In general, there has to be an order of magnitude improvement in some area before it is considered for replacement." [66]

Although the variance reduction factor for the nonlinear controller is impressive (factor of ~ 65) compared to the open loop case, the variance reduction factor is only about ~ 2.2 compared to the optimal proportional controller. In practice, the most likely control option is proportional control with a saturation. However, implementation of the saturation block requires knowledge of the maximum force radius R_F.

This dissertation provides an introduction to optical tweezers, including information about dynamics, construction, identification, and control. Within that framework, a wide range of topics have been covered. In fact, there are many other topics related to optical tweezers that have not been discussed. For example, the fast detection of external force discontinuities is an issue that deserved more attention. I hope the material in this dissertation will enhance the arsenal of tools available to users of optical tweezers (especially in biophysics and microfluidics) and also encourage future contributions from the control engineering community.

Appendix A

LabVIEW Virtual Instruments

The following Virtual Instruments (VI's) were used for data acquisition using *LabVIEW* software version 6.0.

A.1 Power Spectrum Data Acquisition

Figures A.1 and A.2 show the VI used to collect Brownian motion data for power spectrum (and mean passage time) computations. This is a de-bugged and modified (improved) version of *synchaiwithdio(ai is master).vi* from the National Instruments webpage (*www.ni.com*). In this example, 30.0 seconds of data is collected at a sampling rate of $2^{11} = 2048$ kS/s. Three analog voltage channels are sampled, corresponding to x-position, y-position and total laser power. Data is saved to a text file.

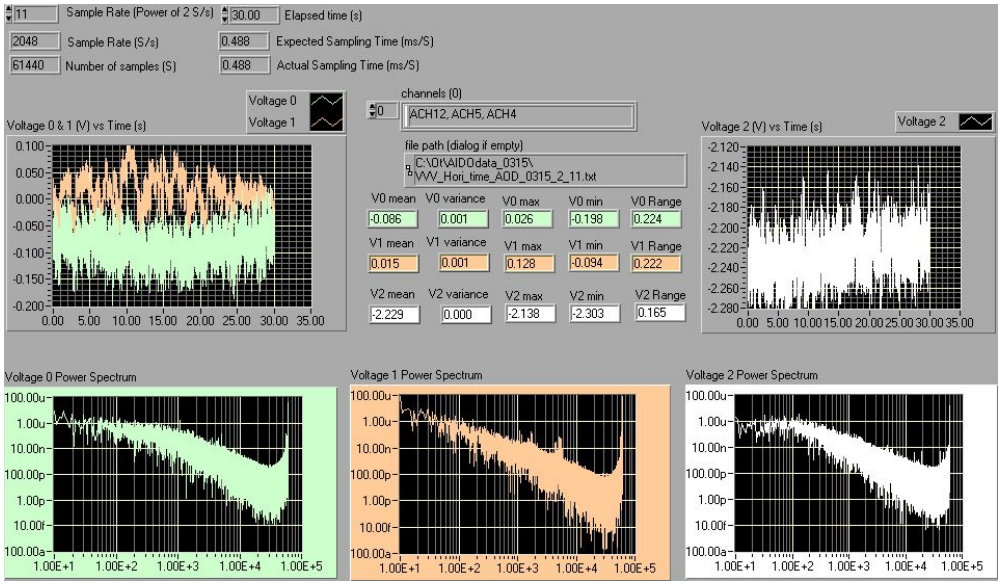

Figure A.1: Front panel for power spectrum data acquisition

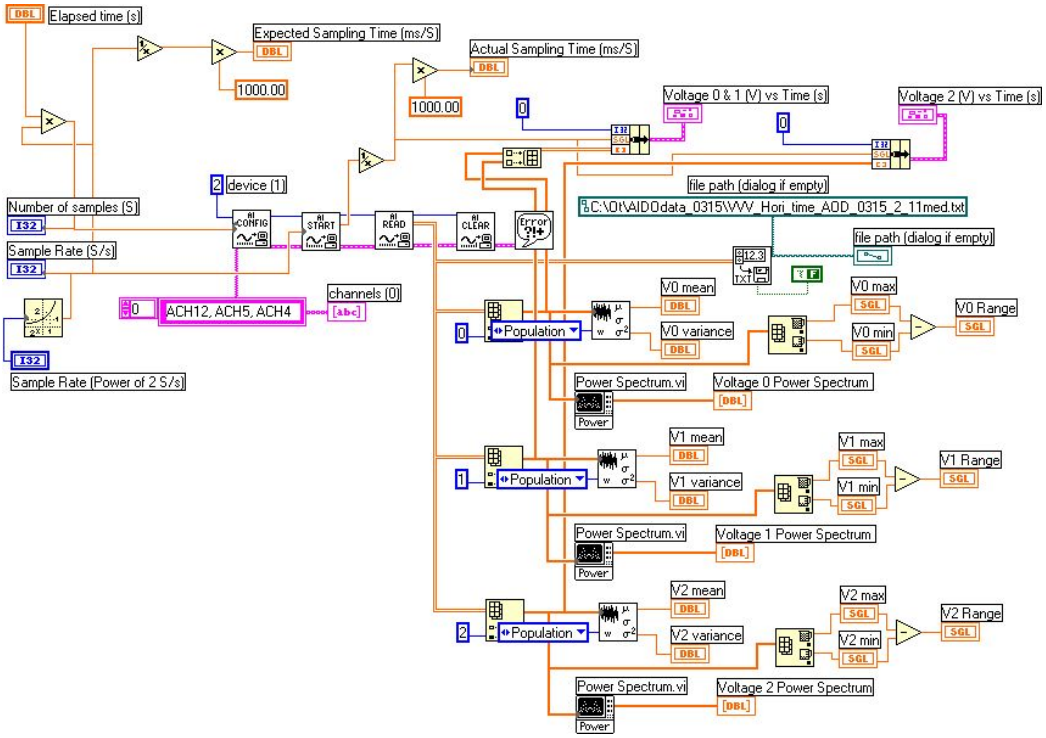

Figure A.2: Block diagram for power spectrum data acquisition

A.2 Square Wave Data Acquisition

Figures A.3 and A.4 show the VI used to generate a square wave using the AOD and measure relative bead position using the position sensing detectors. In this example, a buffer of size $2^{16} = 65536$ samples is used and data acquisition is done at a clock frequency of 2 kHz, the output digital square waveform has a frequency of 1 Hz. Three analog voltage channels are sampled, corresponding to x-position, y-position and total laser power. Input and output data is saved to text files.

A.3 PRBS Data Acquisition

Figures A.5 and A.6 show the VI used to generate any specified input signal, such as a PRBS, using the AOD and measure relative bead position using the position sensing detectors. In this example, a buffer of size $2^{17} = 32768$ samples is used and data acquisition is done at a clock frequency of 1 kHz. The output digital waveform is loaded from a text file generated using *MATLAB*. Three analog voltage channels are sampled, corresponding to x-position, y-position and total laser power. Input and output data is saved to text files.

A.4 AOD Calibration

Figures A.7 and A.8 show the VI used to calibrate the AOD. In this example, the AOD drive frequency is set to the center frequency of 35 MHz, which is converted to a 32-bit binary signal

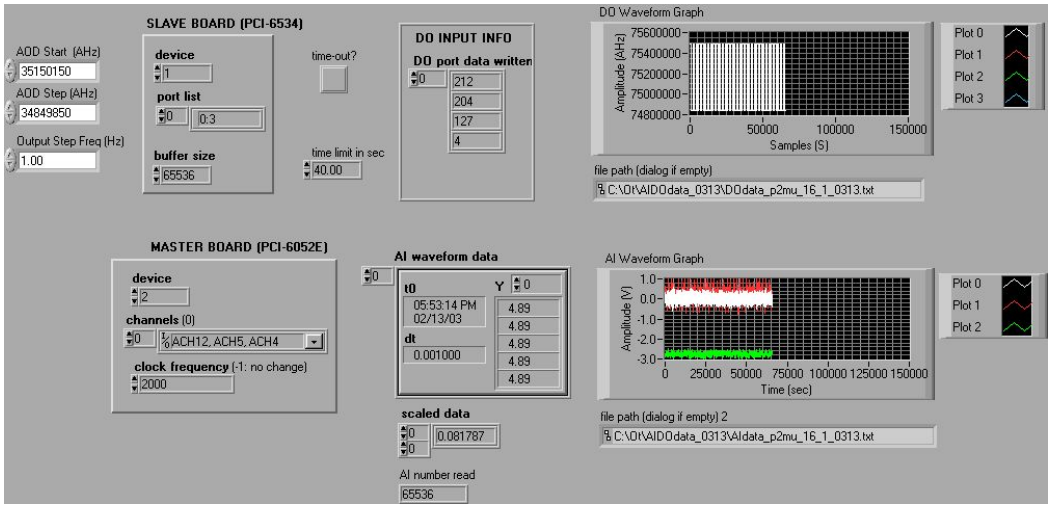

Figure A.3: Front panel for square wave data acquisition

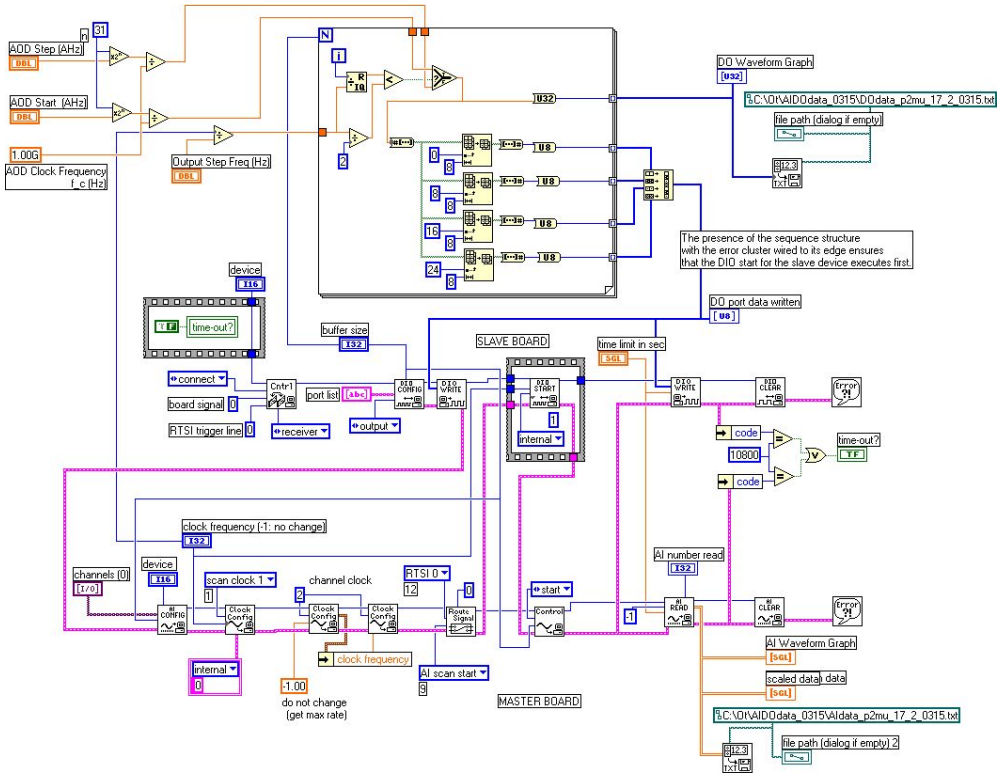

Figure A.4: Block diagram for square wave data acquisition

for the digital frequency synthesizer.

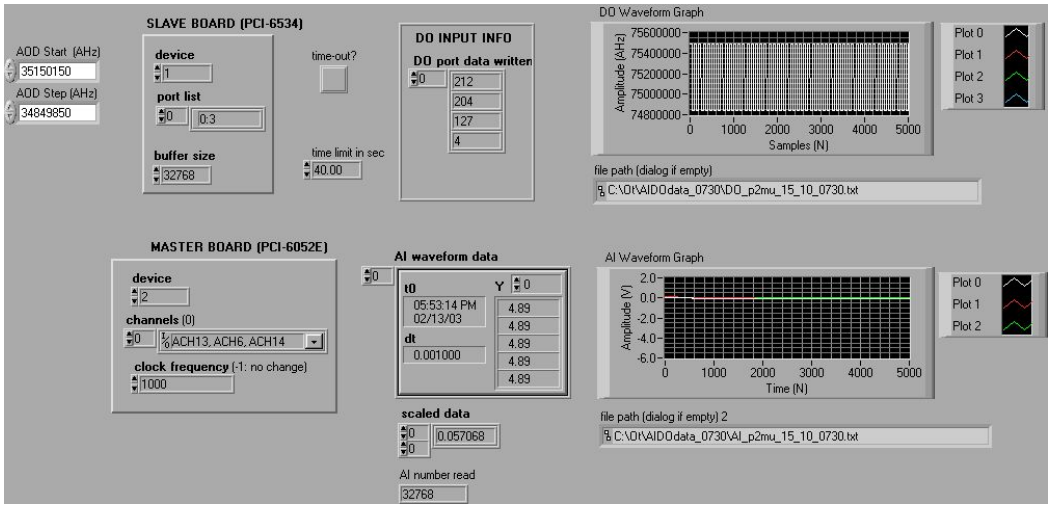

Figure A.5: Front panel for PRBS data acquisition

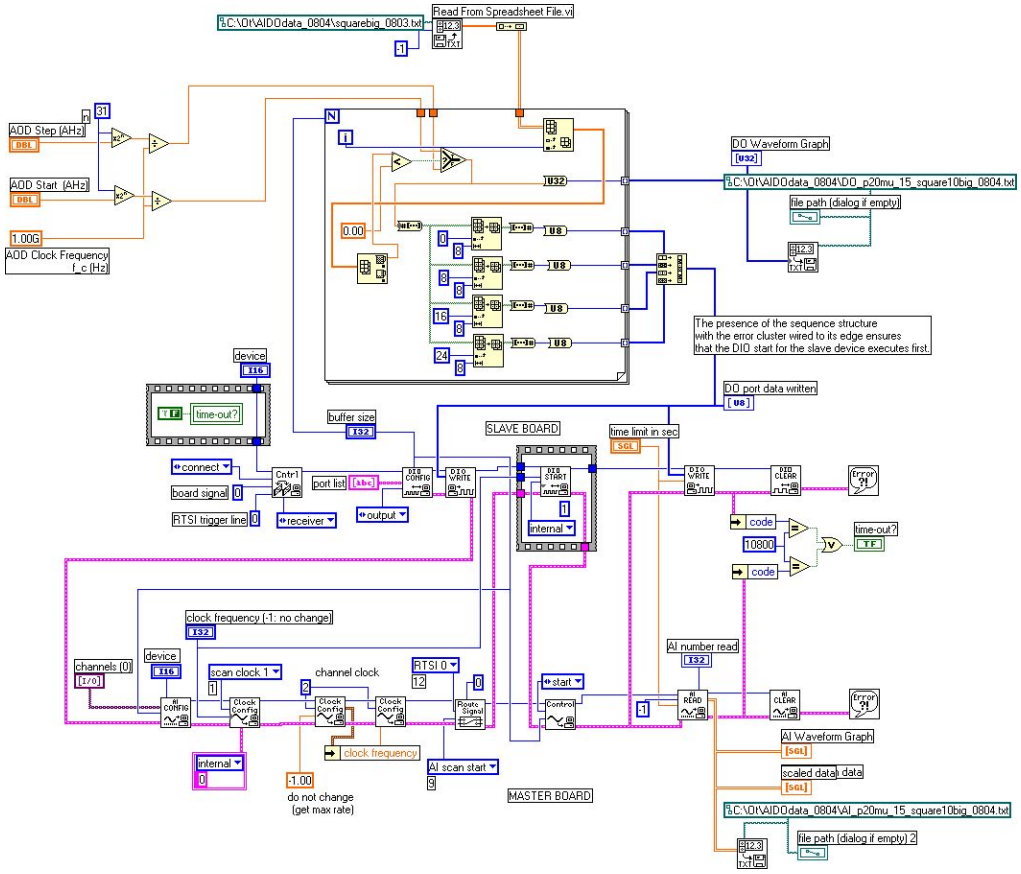

Figure A.6: Block diagram for PRBS data acquisition

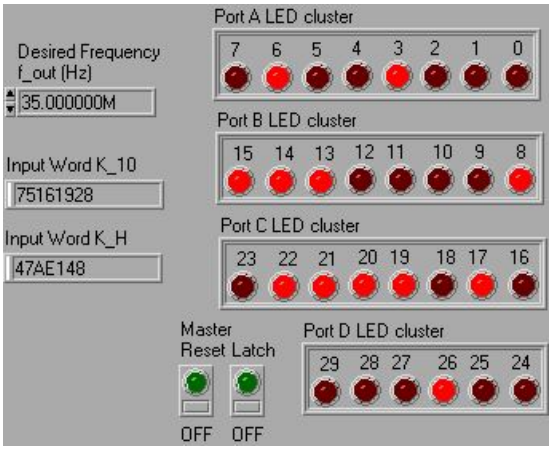

Figure A.7: Front panel for AOD Calibration.

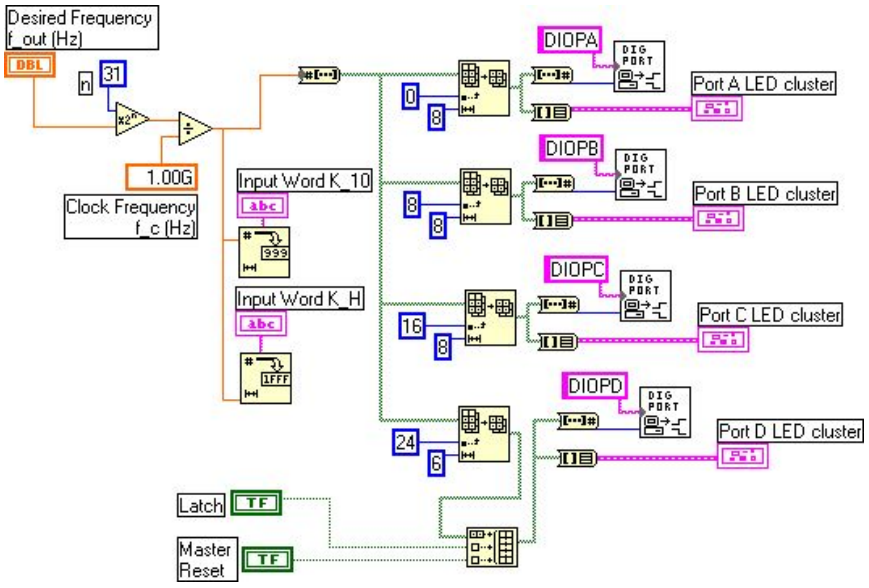

Figure A.8: Block diagram for AOD Calibration.

A.5 PSD Calibration

Figures A.9 and A.10 and sow the VI used to center the laser beam on the position sensing detector (PSD). In this example, three analog voltage signals from the PSD circuit are continuously sampled and displayed. The plots correspond to x position, y position, and total incident laser power. The mean of each signal can also be calculated and displayed.

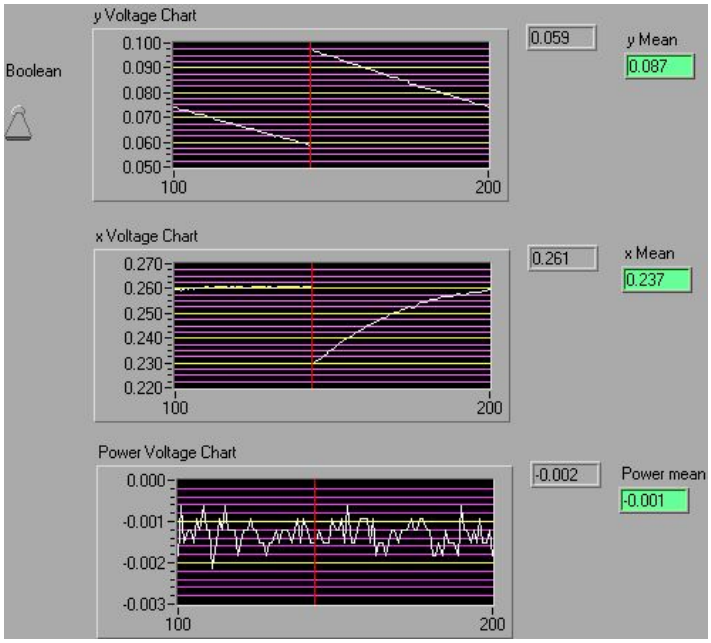

Figure A.9: Front panel for PSD alignment.

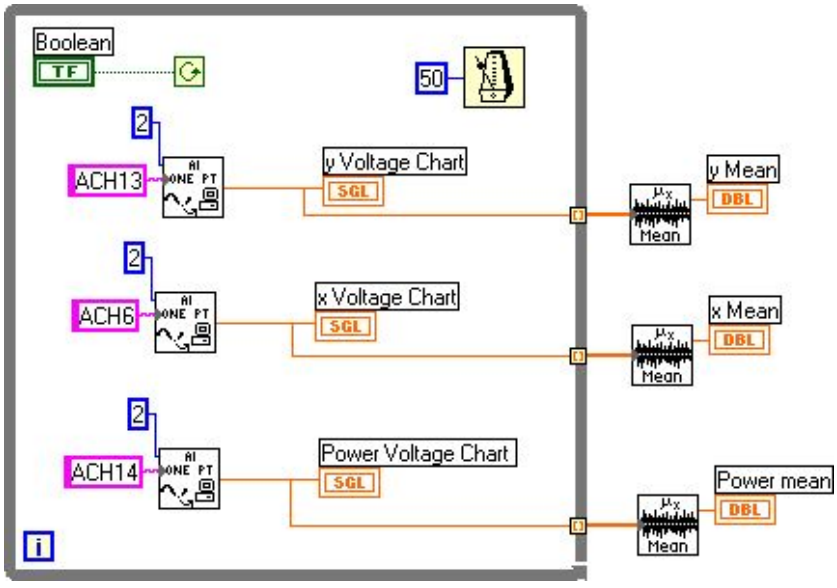

Figure A.10: Block diagram for PSD alignment.

Appendix B

Construction Details

B.1 Trapping System

B.1.1 Laser

Four main characteristics were considered when choosing the trapping laser: output beam shape, beam astigmatism, laser wavelength, and power [12].

For stable trapping, the laser should be a continuous-wave (CW) beam with low noise. For symmetric trapping, the beam itself must have a symmetric cross-section. If the beam is asymmetric, it can be corrected using cylindrical lenses, but this requires additional effort and will result in unnecessary power losses. To focus the laser beam to a diffraction limited spot, the laser should have a single Gaussian peak with minimal side bands, known as single mode or TEM_{00} [9].

Since the optical tweezers are intended to be used for biophysical studies, the trapping laser had to be carefully chosen. A trapping wavelength of $\lambda = 1064$ nm was chosen primarily because biological specimens absorb light most weakly for wavelengths in the range of 800-1100nm [18]. Furthermore, a wide selection of commercial optical components is designed for operation at $\lambda = 1064$ nm.

Laser power was chosen based on discussions with Steven Quake and Chris Meiners at Caltech. Although "polystyrene spheres could be trapped with powers at the back of the objective as small as 5 mW" [12], the actual output power of the laser must be much higher than this because, by the time the laser beam reaches the specimen plane, it will have lost a large fraction of its original power. Smith et al. state that a "laser power of between 20 and 100 mW at the microscope is sufficient for many basic trapping experiments" [12].

The laser power and diameter should be matched such that the power density of the laser does not exceed the laser damage threshold of the optics used. Of the optical components that form the optical tweezer, the lenses had the lowest laser damage threshold, 100 W/cm^2.

We purchased a horizontally polarized continuous wave (CW) diode-pumped infrared Nd:YAG laser (Model IRCL-700-1064, CrystaLaser) that satisfies all of the criteria discussed above. It has a manually adjustable power rage of approximately 370–760 mW, as measured using a laser power meter. The manufacturer specified an output beam diameter of 1.2 mm, according to the standard $1/e^2$ definition of Gaussian beam diameter. (See Appendix E).

B.1.2 Microscope Objective

A 100×/1.3 NA oil immersion microscope objective (Plan Neofluar, Zeiss) was used to create the trap. The immersion oil (Immersol 518F, Zeiss) is designed for fluorescence microscopy. A Zeiss

objective was chosen to ensure compatibility between the tweezer optics and an existing Zeiss microscope (that is used in our laboratory for atomic force experiments). This particular lens was chosen because it has an infinite conjugate and because it has a relatively large working distance of 0.2 mm. Microscope objectives with higher numerical apertures (1.4 NA) are available, but their lower working distances make them difficult to use. Although the damage threshold of these objectives with respect to IR light is not specified, Sterba and Sheetz mention that objectives have been damaged at laser powers exceeding 1 W [9], but it is unclear whether this is at the source or at the OEA.

As shown in (5.2), for a trap arising due to a normally incident, collimated laser beam, if the microscope objective is moved axially (vertically) by some distance, the the laser focus (trap location) is moved by a factor of $\frac{n_f}{n_o}$ within the fluid cell, where $\frac{n_f}{n_o}$ is the ratio of the refractive index of the suspension medium (water) to the refraction index of the immersion oil. Ghislain et al. suggest using a water immersion microscope objective to eliminate the depth dependence [67], but such objectives have numerical apertures of less than 1, which is insufficient for most practical trapping applications.

The microscope objective is attached to a microscope objective kinematic mount (Model KM-RMS, Thorlabs) using *SM*-series lens tubes and adapters (Thorlabs). The lens tubes were required to raise the microscope objective within the specimen stage aperture. The kinematic mount was attached to a low profile precision ball bearing translation stage (Model 423, Newport) that was mounted vertically to a mounting post (Model C8, Thorlabs). The translation stage, and hence the microscope objective, are moved vertically using a manual vernier micrometer (Model SM-13, Newport). This translation stage can be locked in position and it is compatible with many types of motorized actuators.

B.1.3 Fluid Cell

The fluid cell used to hold the specimens consists of a square cover glass stuck to a standard microscope cover slip using double stick tape. The cover glass is of thickness #1 (0.13–0.17 mm) and dimensions of 22 mm×22 mm. The microscope slide is approximately 1.3 mm thick and has dimensions of 3"×1". The double stick tape has a thickness of 3 milli-inches ($\sim$ 75 μm).

If the immersion oil ($n_o = 1.518$ at 23°C) is optically matched with the cover glass (i.e., if they both have roughly the same index of refraction), there will be no refraction at the oil-glass interface. The cover glass is usually assumed to have a refraction index of $n_g = 1.51$. "For immersion objectives, the object is expected to be focused under immersion oil of a specified refraction index and a coverslip of 170-mm thickness ... For nonstandard coverslips and increasing layers of embedding medium between the coverslip and the object, spherical aberration is induced" [15]. Cover glasses of thickness #0 (0.08–0.13mm) were also purchased, but their performance was not investigated.

Although double stick tape provides a very convenient spacer between the microscope slide and the glass cover slip, other spacers can also be used. Kuo and Sheetz used high-vacuum silicon grease [29], while Quake et al. used epoxy [68].

The axial trapping force decreases with increased trap distance from the cover glass [15]. In fact, particles tend to escape from the trap when the trap is more than 20 μm from the surface of the cover glass [9]. This is due to spherical aberrations caused by the high NA objectives not being designed for IR wavelengths. In fact, Felgner et al. found multiple trapping positions (three for polystyrene and five for glass) along the trapping axis, but they blame this anomaly on spherical aberration [15].

B.1.4 Trapped Particles

D'Helon et al. state that "the size range of the particles that can be trapped is determined by the power of the trapping beam. At a given trapping power, as the particle size decreases, thermal forces [e.g., Brownian motion] become comparable to the optical force, rendering the trap inefficient. Conversely, as the particle size increases, the particle weight becomes comparable to the optical force, causing the particle to fall out of the trap [19]. Hence, at lower trapping powers, the use of particles of specific gravity close to one (i.e., same as water) is necessary.

For initial testing and calibration of the optical tweezer, polystyrene spheres of diameters 10.06 μm (PS04N/001013, Bangs Laboratories) and 1.05 μm (PS07N/001394, Bangs Laboratories) were used. Since polystyrene balls suspended in distilled water have a tendency to clump together, they need to be suspended in a phosphate-buffered saline (PBS) solution. A 0.01M PBS solution (Number P-3813, Sigma) added to the aqueous polystyrene beads. In case a PBS solution is not available, Smith et al. provide instructions for preparing a PBS solution, including guidelines for the addition of antistick additives such as polyethylene glycol and bovine serum albumin (BSA) [12]. By increasing the viscosity of the fluid, the effective time resolution of the experiment can be increased. Quake et al. increased the viscosity "from 0.01 to 0.2 poise with the addition of 71% glycerol (w/v) [68], whereas Felgner et al. used water and 60% glycerol (n = 1.41) as their solution [15]. Arai et al. used sucrose to suppress Brownian motion [69].

B.2 Viewing System

The specimens were imaged using a CCD color video camera module (Model XC-999, Sony). To magnify and focus the images onto the CCD array, a video zoom lens (manufacturer unknown) was attached to the front of the camera. For rapid positioning and repositioning, a standard magnetic base (Model 07 BMS 001, Melles Griot) was used to mount the CCD camera. The CCD camera must have this repositioning capability because the position of the optical focus (and hence the z-position of the trap) can change with adjustment of the microscope objective [10]. The signals from the CCD camera were sent to a videocassette recorder (Model HR-VP48U, JVC) for recording and to a 13-inch color video monitor (Model PVM-1390 Trinitron, Sony) for viewing. The various adapters needed to connect the video equipment were purchased from RadioShack.

The digital CCD camera was borrowed from the bioscope (AFM) system in our laboratory. Viewing light is focused on to the CCD array using a telecentric lens (Model KS2271, Edmund Industrial Optics).

B.3 Lateral Steering System

B.3.1 Optics and Optical Mounts

The laser beam was deflected vertically towards the OEA using a broadband silver mirror (Model 20D20ER.2, Newport) mounted on a 45^o mirror holder (Model H45-3, Thorlabs). A 1-mm thick, 36 mm $\times$ 26 mm dichroic mirror (Model 850 dcsp, Chroma) was used to deflect the laser beam towards the silver mirror because it provides high reflection at $\lambda = 1064$ nm and high transmission of visible light. The dichroic mirror was mounted on a kinematic mount.

Laser line dielectric mirrors (Model 10Z40DM.10, Newport) were used to deflect the beam because of their high surface quality and moderate cost. These mirrors are mounted on compact gimbal mirror mounts (Model GM-1B, Newport), that have a manual adjustment range of 12^o and an adjustment sensitivity of 10 arcseconds. One of these mounts was later replaced by an *ULTIMA* gimbal mount (Model U100-G, Newport) because *ULTIMA* mounts are compatible with motorized actuators.

For our microscope objective, $d_\mu = 4.264$ mm. Hence, the laser beam must be expanded from 1.2 mm to slightly larger than 4.264 mm. As stated in Section 5.3, the beam was expanded to 4.76 mm by an appropriate choice of lenses L_1 (50.8 mm dia., 300 mm EFL[1], Model SPX055AR.33, Newport) and L_2 (25.4 mm dia., 75.6 mm EFL, Model SPX019AR.33, Newport). To minimize aberrations, Smith et al. suggest that lenses with focal lengths in the range 5 cm $\leq f \leq$ 40 cm should be used [12], but the lens manufacturer (Newport) does not mention such a strict criterion. UV fused silica precision plano-convex lenses were used because they have a high damage threshold (100 W/cm^2) and moderate cost. The lenses were purchased with an antireflection coating that has a maximum reflectance of less than 0.25% at 1064 nm. As stated in the Newport catalog, "the asymmetry of these lenses minimizes spherical aberration in situations where the object and image are at unequal distances from the lens. The optimum case is where the object is placed at infinity (parallel rays entering the lens) and the image is the final focused point" [50].

Laser line polarizing beamsplitter cubes (Model 10BC16PC.9, Newport) with an extinction ratio of greater than 1000:1 were used to split (and later recombine) the laser beam into two orthogonally polarized components. The PBSC's were mounted on kinematic platform mounts (Model KM1-B, Thorlabs). A multiple order quartz waveplate (Model 05RP12-34, Newport) was inserted just after the laser output aperture. By rotating the waveplate, the direction of laser polarization could be rotated (continuously) as desired. The waveplate was mounted on a polarizer mount (Model LM-1R, Newport) that allowed the rotation of the waveplate to be read in 2^o increments.

B.3.2 Alignment Tools

At a wavelength of $\lambda = 1064$ nm, the laser beam is in the near-infrared regime; it is invisible. To detect its position, infrared sensor cards (Model F-IRC1, Newport) with a wavelength range of 750-1350 nm were used, but these provide only a rough indication of the beam position. For more accurate centering tasks, an infrared viewer (Model NOCX3, Night Owl) with a focusing range of 5 feet to infinity was used. Mounted iris diaphragms (Model ID12, Thorlabs) were used to facilitate the alignment procedure, while 0^o hot mirrors (Model 35-6865, Coherent) were used as both beam reflectors and power attenuators. A hand-held laser power meter (LaserCheck, Coherent) with a built-in attenuator was used to measure the laser power at various locations on the beam path. This power meter could be used to measure powers in the range 10 mW–1 W with an accuracy of $\pm$5%.

The trapping laser is of class IV, the most hazardous class. Appropriate precautions had to be taken to avoid eye injuries. DVO (diffuse viewing only) laser protective goggles (Model LPG-YAG, Uvex Safety) with an optical density (OD) of 7 were worn whenever the laser was in use.

B.4 Position Detectors

A four-element segmented photodiode (Model SPOT-9DMI, UDT) is used as a Position Sensing Detector (PSD) to detect the laser beam with a specified position resolution of better than 0.1 μm [70]. The photodiode has a spectral range of 350–1100 nm and a rise time of 3 ns. Each segment of the photodiode has an active area of 19.6 mm^2, with a gap of 10 μm between each segment. The total diameter of the photodiode (all four quadrants) is 10 mm. For the photodiode to function correctly, the incident beam must overlap all four quadrants (i.e., the beam must be larger than the spacing between the segments). When light hits each segment, a current proportional to the incident light power is generated. The maximum recommended power

[1]Effective focal length.

density is 10 mW/cm^2 and the typical uniformity of response for a 1-mm diameter spot is $\pm 2\%$ [71]. The current output from each segment of the photodiode is converted to a voltage using four low-noise precision operation amplifiers (Model OPA124P-ND, Burr-Brown). These voltages are then appropriately summed using two dual high-speed precision difference amplifiers[2] (Model INA2133U-ND, Burr-Brown) and one high speed difference amplifier (Model AMP03) to obtain three separate voltage channels that indicate the x position, y position, and total power of the incident beam. The x and y position voltages are normalized by the total power level using precision analog multipliers (Model MPY534KD-ND, Burr-Brown). Since the responsivity (0.4 A/W) of the photodiode to light at $\lambda = 1064$ nm is less than the responsivity (0.4–0.65 A/W) of the photodiode for light at $\lambda = 650$–1000 nm, a narrow bandpass interference filter (model 43153, Edmund Industrial Optics) was inserted to reduce noise from ambient light. For a further overview of circuit construction, consult [14]. Practical information about shielding can be found in [72].

Figure B.1 shows the detector response for a trapped 10-μm bead and a fixed 10-μm bead. The trapped bead has a measured variance of $\mathrm{Var}(x) = 0.0021$ μm^2 and the fixed bead has $\mathrm{Var}(x) = 4.52 \times 10^{-5}$ μm^2. The variance for the fixed bead is assumed to be the result of measurement noise, while the variance of the trapped bead is due to both measurement noise and Langevin disturbance.

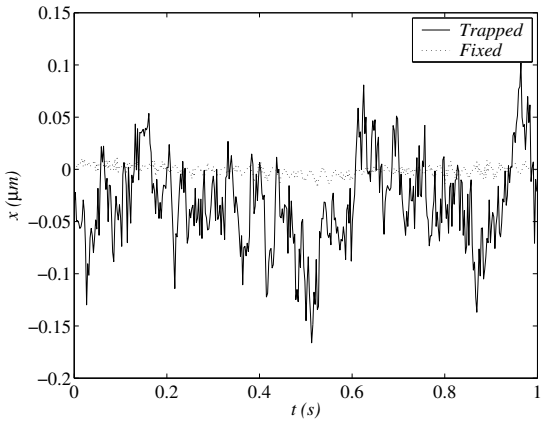

Figure B.1: Comparison between thermal and measurement noise for a 10-μm bead.

Figure B.2 shows both the position fluctuations of a trapped 10-μm bead due to Brownian (random thermal) motion and the computed average of 30 power spectra. A direct calculation of position variance yielded $\sigma_x^2 = 0.0021$ μm^2 and small noise peaks can be seen at just under 200 Hz. The slight slope in the power spectrum at low frequencies is caused by mechanical vibrations and drift in the position detection circuitry [26].

Figure B.3 shows both the position fluctuations of a 10 μm bead that has been fixed to the coverglass and the computed average of 30 power spectra. A direct calculation of position variance yielded $\mathrm{Var}(x) = 4.52 \times 10^{-5}$ μm^2 and several noise peaks can be seen at various frequencies. This indicates the existence of several sources of noise within the laboratory environment. Clearly, the measurement noise is not white, but its power spectrum can be roughly approximated by the constant value of $S_n^+ = 4.52 \times 10^{-8}$ μm^2/Hz for a bandwidth of 1 kHz. The vertical scales in Figure B.3 require verification since the detector calibration may have been altered by the fixed bead position.

[2]Later versions of this circuit use two audio differential line receivers (Model INA2134PA-ND, Digi-Key) and a high speed difference amplifier (Model INA105KP, Sager Electronics).

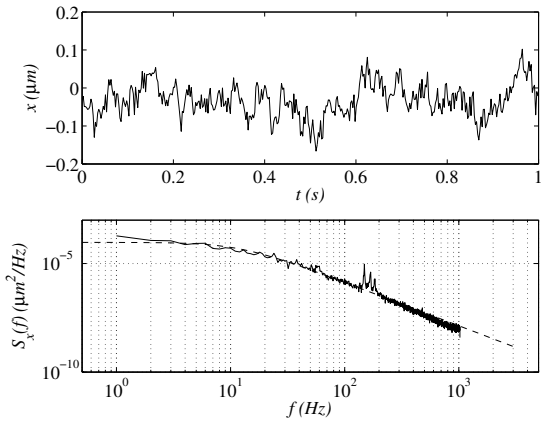

Figure B.2: Top figure shows position fluctuations of a trapped 10-μm bead. Bottom figure shows the average of 30 power spectra and its Lorentzian fit (dashed line). Data was sampled at 2.048 kHz with a lowpass filter at the Nyquist frequency.

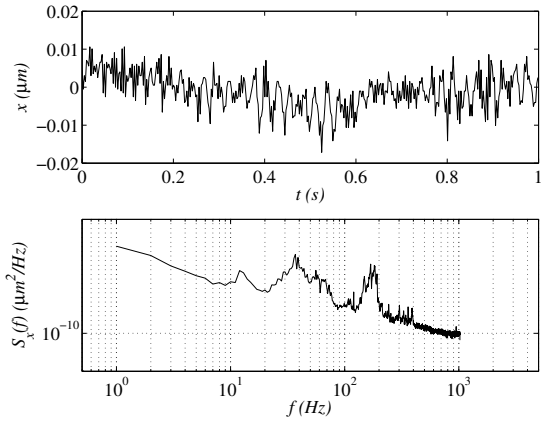

Figure B.3: Top figure shows position fluctuations of a fixed 10-μm bead. Bottom figure shows the power spectrum. Data was sampled at 2.048 kHz with a lowpass filter at the Nyquist frequency.

B.5 Acousto-Optic Deflector

Visscher et al.state that "analog voltage-controlled oscillators typically used to drive the AOD's are not usually stable enough to achieve the desired beam-pointing stability: for applications requiring nanometer-level stability and repeatability, 24- or 32-b digital frequency synthesizers are needed" [18]. Although the response time τ_a of an AOD is intrinsically limited such that typically, $\tau_a \sim 1.6$ ms/mm of laser beam diameter, this limit cannot be achieved in practice because of speed limitations in the computer interface [18]. Despite these limitations, the AOD is a superior choice to other time-sharing devices. The EOD is more efficient than the AOD, but it provides an insufficient full-angle of deflection (~ 2 mrad); scanning galvanometer mirror cost much less than an AOD, but they have insufficient bandwidth ($\sim 200 - 300$ Hz) [18].

Appendix C

Nonlinear Feedback Control for Inertial System

In Section 10.1, we derived feedback control laws to stabilize the origin of the noninertial system described by (3.15). In this section, we derive stabilizing control laws assuming the mass is large enough that it cannot be ignored, in which case the inertial equation of motion (3.11) must be used. Our hope is that these derivations will prove useful in the future when the technology behind optical tweezers evolves such that larger masses can be trapped. As shown in Section 3.2.1, by setting $u := x_T$ and $x_1 := x$, we can express the inertial system in state space form as (3.15), which is reproduced below:

$$\begin{aligned} \dot{x}_1 &= x_2 \\ \dot{x}_2 &= \frac{\psi(x_1 - u)}{m}\left[\alpha_3(x_1 - u)^3 - \alpha_1(x_1 - u)\right] - \frac{\beta}{m}x_2 + \frac{1}{m}\left(F_L + F_E\right) \\ y &= x_1. \end{aligned} \tag{C.1}$$

As in the noninertial case, we will derive control laws under the assumption of zero disturbance, $F_L(t) = F_E(t) = 0$.

Asymptotic Stability

As before, we can use the restoring force $F_T(x_r)$ to stabilize the system, $\dot{\eta} = A\eta + BF_T(x_r)$, in which $\eta := [x_1\ x_2]^T$, and

$$A = \begin{bmatrix} 0 & 1 \\ 0 & \frac{-\beta}{m} \end{bmatrix}, \quad B = \begin{bmatrix} 0 \\ \frac{1}{m} \end{bmatrix}. \tag{C.2}$$

Notice that A is stable, but not Hurwitz and (A,B) is reachable, and therefore stabilizable. Therefore, we can apply the saturation analysis from [64]. Specifically, if we can find $P = P^T > 0$, such that

$$A^T P + PA = -Q \leq 0, \tag{C.3}$$

we can choose a Lyapunov function $V(\eta) = \eta^T P \eta$ and set:

$$\begin{aligned} -\lambda x_r &= -B^T P \eta \\ x_r &= \frac{1}{\lambda} B^T P \eta. \end{aligned} \tag{C.4}$$

Then,

$$\begin{aligned}\dot{V}(\eta) &= -\eta^T Q\eta + 2\mu B^T P\eta \tanh(-B^T P\eta) \\ &= -\eta^T Q\eta - 2\mu y \tanh(y) \leq 0,\end{aligned} \tag{C.5}$$

which shows that the origin of the η system is asymptotically stable in the domain $|x_r| < R$ [65]. The general version of the proof of stability given in [64] uses further analysis (employing tools such as LaSalle's invariance principle) to prove AS, but the simple structure of the matrix Q in (C.5) makes such analysis unnecessary in this case. In particular, substituting (C.2) into (C.3), it can be shown that the positive semidefinite matrix Q must take the form $Q = \begin{bmatrix} 0 & 0 \\ 0 & q \end{bmatrix}$, in which $q > 0$. This implies that the positive definite matrix P must take the form $P = \begin{bmatrix} \frac{\beta}{m}p & p \\ p & \frac{m}{\beta}(\frac{1}{2}q + p) \end{bmatrix}$, in which $p > 0$. Therefore, from (C.2),

$$\frac{1}{\lambda}B^T P\eta = \frac{1}{\lambda}\left[\frac{p}{m}x_1 + \frac{1}{\beta}\left(\frac{1}{2}q + p\right)x_2\right]. \tag{C.6}$$

The expression given by (C.6) is difficult to apply in practice because m is typically many orders of magnitude smaller than β. However, by choosing $p = k_1 m$ and $q = 2(\beta k_2 - p)$, we can re-parametrize (C.6) in a more convenient form as:

$$\frac{1}{\lambda}B^T P\eta = \frac{1}{\lambda}(k_1 x_1 + k_2 x_2), \tag{C.7}$$

in which,

$$\begin{aligned} k_1 &> 0 \\ k_2 &> \frac{m}{\beta}k_1, \end{aligned}$$

to preserve $p, q > 0$. From (3.1), (C.4), and (C.7), the asymptotically stabilizing linear feedback control law is given by:

$$u = \left(1 - \frac{k_1}{\lambda}\right)x_1 - \frac{k_2}{\lambda}x_2. \tag{C.8}$$

According to (C.7), for a particle starting at rest, that is, $x_2(0) = 0$, when absolute position $|x_1(0)| \geq \frac{\lambda}{k_1}R$, we find $|x_r| \geq R$ for all time and therefore the particle will remain motionless ($x_2 = 0$), but away from the origin ($x_1 \neq 0$) and out of the controller's reach.

Global Asymptotic Stability

As in the noninertial case, to achieve global asymptotic stability (GAS), we suggest setting the relative position equal to a hyperbolic tangent function:

$$x_r = \omega \tanh\left(\frac{1}{\lambda}B^T P\eta\right), \tag{C.9}$$

in which, $0 < \omega < R$. From (3.1), (C.7), and (C.9), the globally asymptotically stabilizing nonlinear feedback control law u is given by

$$\begin{aligned} u &= x_1 - \omega \tanh\left(\frac{1}{\lambda}B^T P\eta\right) \\ &= x_1 - \omega \tanh\left[\frac{1}{\lambda}(k_1 x_1 + k_2 x_2)\right]. \end{aligned} \tag{C.10}$$

The nonlinear control algorithm given by (C.10) was simulated for system parameters $m = 5.5 \times 10^{-10}$ mg, $\beta = 0.01$ pNs/μm, $\alpha_3 = 22$ pN/μm^3, $\alpha_1 = 10$ pN/μm, $\lambda = 5$, and control parameters $k_1 = 1000$, $k_2 = 2\frac{m}{\beta}k_1 \approx 1.1 \times 10^{-4}$, and $\omega = 0.3893$ μm as shown in Figure C.1. Since $k_1 \gg k_2$, this corresponds to position feedback. In fact, the control gains chosen here are roughly equivalent to the GAS control gain ($p = 10$) that was used in Figure 10.4. It should be noted that since our system simulation parameters reflect values that we expect to encounter in an actual experiment, the mass is negligible compared to the drag. Therefore, the inertial system model and noninertial system model are essentially equivalent, as can be seen by the similarity between Figures 10.4 and C.1.

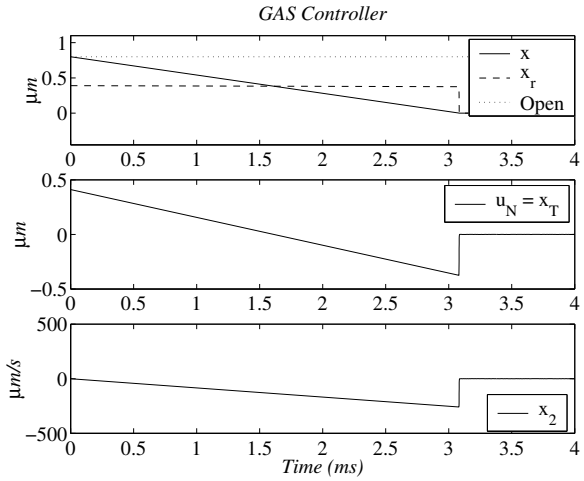

Figure C.1: Simulation of global asymptotic stabilization of the origin of the inertial system model for $x_1(0) = 0.8$ μm and start from rest $x_2(0) = 0$.

Appendix D

Future Directions

D.1 Optional Construction Work

This section describes construction options that can be added if necessary to increase the overall capabilities of our optical tweezers.

D.1.1 Axial Steering System

In addition to being able steer the trap in the lateral (xy) plane, it may prove useful to steer it in the axial (z) direction as well. The method for doing so is from Fallman and Axner [21]. As shown in Figure D.1, lens L_4 can be used to move the trap in the z direction, with both lens L_4 and lens L_3 positioned to guarantee that the stability requirements are met. These two lenses should be placed at a distance of $f_3 + f_4$ apart such that they form a telescope that expands the laser beam by the ratio $\frac{f_3}{f_4}$, which for compatibility with the steering arrangement from Section 5.3, can be chosen to be equal to one. The distance between L_3 and the gimbal-mounted mirror should be f_3.

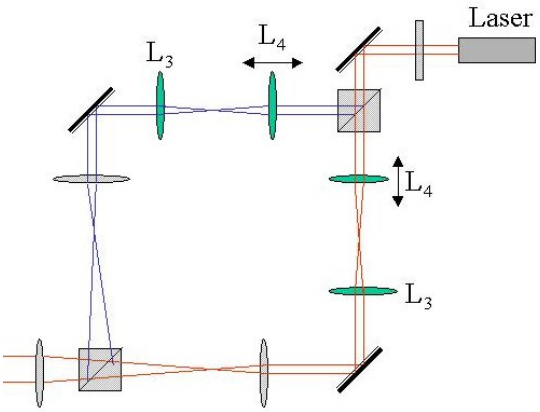

Figure D.1: Vertical steering system.

With these additions, (5.4) should be updated as follows:

$$d_{\lambda\mu} = \frac{f_1 f_3}{f_2 f_4} d_\lambda \tag{D.1}$$

Furthermore, the axial (vertical) motion of the trap in the z direction, Δz_T, will be related to the axial displacement of lens L_4, Δz_4, as follows:

$$\Delta z_T = \left(\frac{f_\mu}{f_1}\right)^2 \left(\frac{f_2}{f_3}\right)^2 \Delta z_4. \tag{D.2}$$

D.1.2 Time Sharing System

Although two independently steerable traps can be obtained using polarizing beam-splitting cubes, creating more than two traps (without increasing the number of laser sources) requires the use of a time-sharing device. Although a scanning galvanometer mirror or an electro-optic deflector (EOD) could be used for time-sharing, the most practical device is the acousto-optic deflector (AOD). Since AOD's are computer-controlled, the creation of multiple traps can be specified with great flexibility [18]. Extensive details for the implementation of a PC-based time-sharing system that uses an AOD can be found in [18, 73, 10], whereas information regarding the spot resolution of an AOD can be found in [43].

D.1.3 Fluorescence Microscopy

For the study of some types of biological interactions, fluorescence-imaging techniques provide richer information than regular viewing. If necessary, fluorescence imaging capabilities can be added to our optical tweezer system with minor modifications.

D.1.4 Combined Axial and Lateral Position Detectors

For detecting both axial and lateral displacements, Ghislain and Webb have suggested a scheme in which the photodiode is positioned such that "roughly half the optical power in the diverging cone of light illuminating it is intercepted" [67, 18]. Lateral displacements are registered by the normalized x and y outputs from the photodiode, while axial displacement are detected by the amount of total power intercepted by the photodiode.

D.2 Alternate Equipment Calibration Methods

In the main text, the AOD was calibrated before the photodetectors. In this section, we describe an alternate calibration method in which the photodetector is calibrated before the AOD.

D.2.1 Position Detector Calibration

Visscher et al. suggested the following three-step process for calibration of the position detectors [18]:

1. "The pixel size of the video system is first determined by imaging a precision, diamond-ruled grid carrying a line pattern with 10-μm spacing on the CCD camera.

2. A piezo stage is then calibrated by driving it with a triangle-wave voltage and recording on video the movement of a bead fixed to the coverglass. Due to piezo hysteresis and nonlinearity, this produces a nonlinear displacement waveform.

3. After calibration and linearization of the piezo stage, a bead fixed to the coverglass is moved through the trap with a periodic voltage computed to generate a true triangle-wave of displacement, while the detector response to this calibrated displacement is recorded. [18]"

We did not attempt this method because a suitable piezo stage is not available in our laboratory.

D.2.2 AOD Calibration

Instead of using digital images to calibrate the AOD as in Section 6.3, Simmons et al. measured trap movement by recording the movement of stage micrometers [10]. A position detector is adjusted so that its output is zero for a trapped bead. As before, the bead is moved to different lateral positions along a straight line by driving the AOD at different frequencies. The output from the photodetector will become nonzero because of the detector beam deflection. At each frequency, the micrometers that translate the sample stage are adjusted until the output from the photodetector is nulled. The lateral displacement that was made using the micrometers provides the change in trap position. Therefore, the relation between drive frequency and trap position can be obtained.

D.3 Additional Off-Line Trap Calibration Methods

This section describes off-line trap calibration methods that have not been completed for our optical tweezer system.

Lateral Escape Force Method

The lateral escape force method is the most common method used to calibrate the trap strength $(F_T)_{\max}$ in the lateral plane. Once a particle of known diameter is trapped, the fluid cell is moved laterally at an ever-increasing velocity until the particle shoots out of the trap. The process is recorded on standard VHS videotape and the velocity of the sphere relative to the fluid can be obtained by studying the video frames just prior to the sphere's escape. The drag force F_D acting on the sphere can be obtained using Stoke's equation

$$F_D = 6\pi\eta_f r_b v_{fb}, \tag{D.3}$$

where η_f is the fluid viscosity, r_b is the radius of the sphere, and v_{fb} is the velocity of the fluid medium relative to the sphere. The escape velocity v_{esc} of the sphere (relative to the fluid) is obtained by observing the position of free (untrapped) spheres that move at the same velocity as the fluid. Once v_{esc} has been determined, $(F_T)_{\max}$ can be calculated from the force balance

$$(F_T)_{\max} = 6\pi\eta_f r_b v_{\text{esc}}. \tag{D.4}$$

Prior to calibration, free spheres can be positioned (using the optical tweezer itself) so that they form a convenient linear scale. Although published literature suggest that particles stuck to the coverslip could be used as position references, particles traveling within the fluid provide a more accurate measure of actual fluid velocity. This is especially true when one considers that (D.3) is accurate only when the trapped sphere is at least several ball diameters away from the fluid cell wall. In fact, when the sphere is closer to the wall (but still not touching it), the corrected drag force $F_{D'}$ is given by the Lorentz formula

$$F_{D'} = 6\pi\eta_f r_b \left(1 + \frac{9}{16}\frac{r_b}{h_b}\right) v_{fb} \tag{D.5}$$

where h_b is the height from the sphere center to the wall surface [26].

The VCR captures video frames at a rate of 30 Hz, and each frame can be still-advanced for maximum temporal resolution (1/30 sec) during playback. Higher quality video images can be

obtained using the s-VHS recording format. Despite its crudeness, the lateral escape method can be used to calibrate $(F_T)_{\max}$ to within 10% accuracy [18]. By observing the maximum escape distance (from the center of the trap), this method can also be used to determine the maximum force region R_F [10]. The main advantage of this method is that it does not require the use of sensitive position detectors. However, since the maximum escape force occurs in the nonlinear region of the trap, this method cannot be used to calibrate the linear trap stiffness. If the method is modified such that with the fluid being moved at a fixed velocity, the laser power is reduced until the sphere escapes, "somewhat better reproducibility of measurements" can be obtained [18].

The escape force method was done by moving the specimen stage by hand, but a smoother acceleration could be obtained using a motorized actuator. For calibration with greater than 10% accuracy, the translation stage must be equipped with high-resolution piezo-electric actuators [18]. Although the xy translation stage in our system is compatible with several brands of commercially available piezo-electric actuators, the minimum incremental motion of such actators is unsufficient[1]. Therefore, the DC motors described in Section 5.3.1 can be used for this type of calibration even though their minimum incremental motion is larger than desired. Preliminary calibration results for our optical tweezer are included in [46].

Lateral Capture Method

The lateral capture method is used to calibrate the capture range velocity v_R in the lateral plane. This is similar to the lateral escape method from Section D.3, except that the particle starts in motion and is brought to rest, instead of the other way around. The experimental procedure is similar except that the fluid is moved at a constant velocity and the particle to be investigated starts from beyond the range of influence R of the trap. The experiment is repeated at increasing (constant) velocities until the tweezer can no longer trap the moving particle.

Drag Force Method

The drag force method uses the same idea as the escape force method, but it is used to calibrate the trap stiffness α within the linear Hookeian region R_l. The linear region extends 100-300 nm maximally [9]. The trap stiffness α is obtained by applying a known viscous drag force F_D (according to (D.3)) and measuring the relative displacement $x_r := x - x_T$ of a trapped sphere from the trap center.

$$\alpha = \frac{F_D}{x_r} \tag{D.6}$$

The drag force can be obtained by moving the fluid cell using a periodic displacement [18]. A triangular displacement motion (corresponding to square wave of fluid velocity v_{fb}) will produce a square force, while a sinusoidal displacement motion will produce a cosine force. This method requires both a well-calibrated motion stage and position detection system and also knowledge of the viscous drag.

Axial Escape Force Method

Since the trap is weakest in the axial direction opposite the direction of the laser beam, the maximum restoring force (strength) of the trap in this direction can be used to characterize the overall performance of the trap [19]. The axial trapping force is obtained by reducing the laser power until a spherical trapped particle falls out of the trap due to gravity. This method

[1]Most commercial piezo-electric actuators have excellent specifications under very low load conditions, but when incorporated with our large platform translation stage, their performance becomes inadequate. An alternative would be to purchase a piezo-electric translation stage, but they are expensive.

requires that the trapping particles are denser than the surrounding medium, but in practice, they also need to be sufficiently large that they sink if not held in place by the trap. To this end, Felgner et al. used large glass beads [15]. The axial force $(F_T)_{ax}$ is given by

$$(F_T)_{ax} = \frac{1}{6}(\rho - \rho_f)d^3 g, \tag{D.7}$$

where ρ and ρ_f are the densities of the bead and the suspension medium, d is the diameter of the bead, and g is gravitational acceleration [15]. For smaller glass beads and polystyrene beads that take a longer time (several minutes) to sink, Felgner et al. used a thermodynamic argument to obtain the following expression for the axial trapping force on a bead of diameter d:

$$(F_T)_{ax} = \frac{2k_B T}{d}. \tag{D.8}$$

For medium sized glass beads, they suggest that the gravitational and thermal contributions to the axial trapping force should be added [15].

D.4 Future Investigations

Following are several applications of optical tweezers that are of interest to the author. These may be investigated in the future.

D.4.1 Attempted Work

Micro-mixing

Carl Meinhart has suggested the use of optical tweezers to verify theoretical models for the mixing of fluids. Although the mixing of two fluids with a vertical interface could be attempted with our present setup, such mixing may not be feasible for fluids with different indices of refraction because spherical aberration at the fluid interface will almost certainly destroy the stability of the trap (Figure D.2). Thus far, our attempts to move a trapped sphere across a vertical interface from water to a silicon fluid have failed because the particle would not cross the fluid interface. Whether this is due to spherical aberration, surface forces at the fluid interface, or high viscosity is not clear. However, the mixing of two fluids with a horizontal interface should pose fewer aberration problems, even for fluids with different indices of refraction. Such mixing could be investigated if vertical steering and horizontal viewing capabilities are added to the optical tweezers.

To avoid spherical aberration issues, Derek Trethaway suggested mixing different colored water separated by a vertical interface. Unfortunately, the color interface was not clearly visible under the microscope because of diffusion. As a result, mixing effects could not be noticed within the microscope viewing diameter of approximately 100 μm. Trethaway suggested using a fluid micromixing device to pump colored water separated by a vertical interface. If the fluids velocity is fast enough to overcome the rate of diffusion, the color interface between the two moving fluids should be roughly visible at the vicinity of their meeting point as shown in Figure D.3.

D.4.2 Unattempted Work

Positioning Tool for Atomic Force Microscopy

Steven Chu mentions how optical tweezers can be used to spot-weld polystyrene beads on to a microscope slide. This could be used to position samples in various configurations (for example, in a stretched state) for study using atomic force microscopy and related techniques [3, 74]. Since

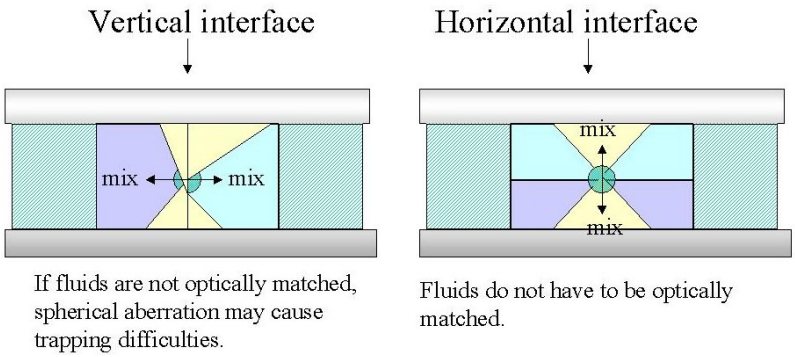

Figure D.2: Micromixing two stationary fluids with different indices of refraction.

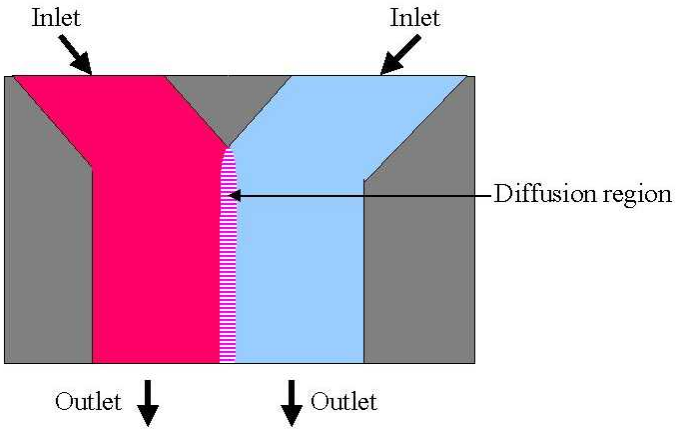

Figure D.3: Micromixing colored water in a fluid cell.

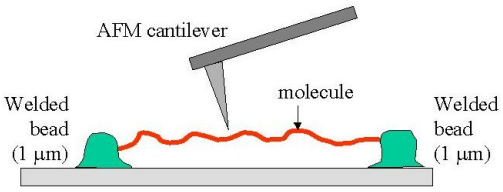

Figure D.4: Spot welding samples for AFM scanning.

many biological samples require meticulous chemical preparations before they can be stuck to a test surface, the use of optical tweezers for spot-welding could save a lot of time and effort.

Ratnesh Lal has suggested using optical tweezers to hold samples for AFM scanning without spot-welding them to the microscope slide. Although it was initially unclear whether this

approach would be feasible because of the disparity between typical optical trapping forces ($\sim$ piconewtons) and typical AFM probe forces ($\sim$ nanonewtons), researchers have demonstrated that AFM's can be used to measure forces even smaller than piconewtons. Lal has suggested that an additional trap be created using time sharing to allow the three-dimensional clamping of large cells.

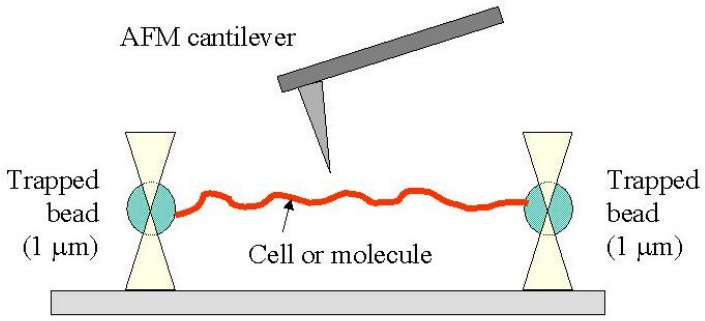

Figure D.5: Holding samples for AFM scanning without spot-welding.

Optical Force Microscopy

The optical tweezer itself can be used to obtain surface images of biological samples, using a process known as optical force microscopy (OFM) [75, 40]. Once the optical tweezer has been automated, its conversion into an OFM is straightforward. The advantage of the OFM over conventional force microscopes (such as the AFM) is that it causes significantly less damage to imaged samples. This is because the probe used by an OFM (a trapped particle), is more compliant than the probe used by an AFM (a silicon cantilever). The resolution that can be obtained using an OFM can be optimized by the use of appropriate probe geometry and by the use of feedback control.

Hydrodynamic Interactions

Meiners and Quake have demonstrated that optical tweezers can be used to investigate quantitatively the nature of hydrodynamic interactions between two colloidal particles suspended in water [41].

Trap Modeling

As mentioned in Section 2.2, accurate theoretical estimations of the trapping force exist only for particles with spherical geometry that are trapped in two separate size regimes [15]. According to Svoboda and Block, however, it is unclear whether the discrepancies between theory and experiment are due to incompleteness of the models or errors in the measurements (or both) [20]. Once the optical tweezer has been fully automated, it can be used to investigate experimentally the validity of theoretical models.

Sorting

Morishima et al. showed how optical tweezers, when combined with an electric field, can be used to transport and separate microbes such as *Escherichia coli* within a microchannel [76]. In fact, when the trapping force of optical tweezers is reduced by the use of low numerical aperture

microscope objectives, the device can be used as a cell sorter. Odde and Renn show how a similar arrangement can be used to guide and deposit 100 nm–10 μm-diameter particles onto solid surfaces with micrometer-scale accuracy using a process they called "laser-guided direct-writing" [77]. They anticipate applications in tissue engineering, hybrid electronic-biological devices, and biochip array fabrication.

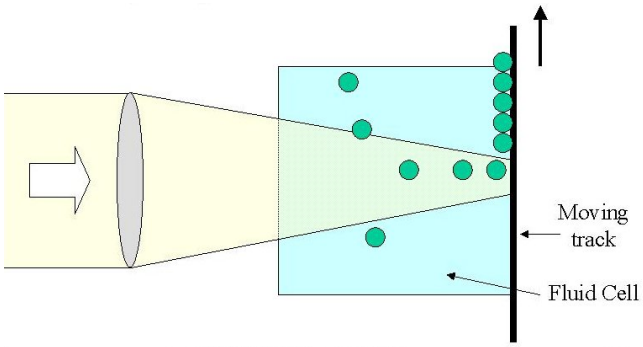

Figure D.6: Laser-guided direct-writing.

Microsurgery

Although extremely high energy densities can be generated by an optical tweezer, this occurs only in a very small volume near the focus of the laser beam [78] and the generated heat dissipates into the water within a few nanoseconds [79]. Hence, the tweezer can be used to manipulate the interior of a transparent object, such as a biological cell, without damaging its walls. Berns et al. have combined optical tweezers with an older device, laser scissors, such that they can not only hold, but also cut individual cells and organelles [80].

Micromachining

Gauthier used optical tweezers to trap not just spheres, but also cylinders, rings, and stars with dimensions in the range 1–10 μm. He suggests that such diverse trapping objects can be used for the assembly, activation, and possibly repair, of micro-machines [81]. In fact, Padgett and Allen have demonstrated that optical tweezers can be used not only to trap, but also to rotate trapped particles [4], but their method requires that the trapping laser have a Laguerre-Gaussian profile.

Appendix E

Optical Glossary

Numerical Aperture the numerical aperture (N_A) of a microscope objective is defined as

$$N_A = n_o \sin(\theta_\lambda)_{\max} \tag{E.1}$$

where n_o is the relative refractive index of the immersion medium (oil) and $(\theta_\lambda)_{\max}$ is the half-angle of the maximum cone of light that can be focused using that objective as shown in Figure E.1 [82]. The incoming light is assumed to be collimated.

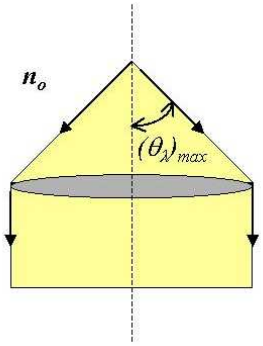

Figure E.1: Numerical aperture.

Gaussian Beam Profile A Gaussian intensity distribution is characterized by the following equation:

$$I(r) = I_o \exp\left(\frac{-2r^2}{w_T^2}\right) \tag{E.2}$$

Where $r = r(x, y)$ [50]. The parameter w_T, known as the Gaussian beam radius or beam waist, is the radius at which the intensity of the beam has dropped to $1/e^2$ of its value along the axis. The intensity will be half-maximum at $r = 0.59w_T$. The power contained within a radius r is given by

$$P_\lambda(r) = P_\lambda(\infty)\left[1 - \exp\left(\frac{-2r^2}{w_T^2}\right)\right] \tag{E.3}$$

[50]. On-axis intensity is related to the total power according to

$$I(0) = P_\lambda(\infty)\frac{2}{\pi w_T^2} \tag{E.4}$$

[50]. When cutting off the beam with a small aperture, the far-field intensity distribution can become non-Gaussian. To minimize this effect, the aperture diameter should be at least three or four w_T.

Power Density The power density PD of a continuous wave (CW) laser is its power per unit area:

$$PD = \frac{P_\lambda}{\pi r_\lambda^2}, \tag{E.5}$$

where r_λ is the beam radius and P_λ is the laser power [50]. As a safety precaution, the power density should be multiplied by 2.

Bibliography

[1] A. Ashkin, "History of optical trapping and manipulation of small-neutral particle, atoms, and molecules," *IEEE J. Select. Topics Quantum Electronics*, vol. 6, no. 6, pp. 841–856, 2000.

[2] S. M. Block, "Making light work with optical tweezers," *Nature*, vol. 360, pp. 493–495, 1992.

[3] S. Chu, "Laser manipulation of atoms and particles," *Science*, vol. 253, pp. 861–866, 1991.

[4] M. Padgett and L. Allen, "Optical tweezers and spanners," *Physics World*, pp. 35–38, September 1997.

[5] Cell Robotics, Inc., Albuquerque, NM., *Cell Robotics Workstation*, 2000. U.S. Price List.

[6] Z.-P. Luo and K.-N. An, "Development and validation of a nanometer manipulation and measurement system for biomechanical testing of single macro-molecules," *Journal of Biomechanics*, vol. 31, pp. 1075–1079, 1998.

[7] Arryx, Inc., Chicago, IL., *Arryx BioRyx 200 System*, 2002. www.arryx.com.

[8] R. Lepman, 2004. Director of Sales and Marketing, Arryx, Inc., Chicago, IL.

[9] R. E. Sterba and M. P. Sheetz, "Basic laser tweezers," in *Methods in Cell Biology* (M. P. Sheetz, ed.), vol. 55 (*Laser Tweezers in Cell Biology*), ch. 2, pp. 29–41, Academic Press, 1998.

[10] R. M. Simmons, J. T. Finer, S. Chu, and J. Spudich, "Quantitative measurements of force and displacement using an optical trap," *Biophys. J.*, vol. 70, pp. 1813–1822, 1996.

[11] A. D. Mehta, M. Rief, J. A. Spudich, D. A. Smith, and R. M. Simmons, "Single-molecule biomechanics with optical methods," *Science*, vol. 283, pp. 1689–1695, 1999.

[12] S. P. Smith, S. R. Bhalotra, A. L. Brody, B. L. Brown, E. K. Boyda, and M. Prentis, "Inexpensive optical tweezers for undergraduate laboratories," *Am. J. Physics*, vol. 67, no. 1, pp. 26–35, 1999.

[13] M. P. Sheetz, "Preface," in *Methods in Cell Biology* (M. P. Sheetz, ed.), vol. 55 (*Laser Tweezers in Cell Biology*), pp. xi–xii, Academic Press, 1998.

[14] A. D. Mehta, J. T. Finer, and J. A. Spudich, "Reflections of a lucid dreamer: optical trap design considerations," in *Methods in Cell Biology* (M. P. Sheetz, ed.), vol. 55 (*Laser Tweezers in Cell Biology*), ch. 4, pp. 47–69, Academic Press, 1998.

[15] H. Felgner, O. Muller, and M. Schliwa, "Calibration of light forces in optical tweezers," *Appl. Optics*, vol. 34, no. 6, pp. 977–982, 1995.

[16] R. Pool, "Trapping with optical tweezers," *Science*, vol. 241, no. 4869, p. 1042, 1988.

[17] A. Ashkin, "Optical trapping and manipulation of viruses and bacteria," *Science*, vol. 235, pp. 1517–1520, 1987.

[18] K. Visscher, S. P. Gross, and S. M. Block, "Construction of multiple-beam optical traps with nanometer-resolution position sensing," *IEEE J. Select. Topics Quantum Electronics*, vol. 2, no. 4, pp. 1066–1076, 1996.

[19] C. D'Helon, E. W. Dearden, H. Rubinsztein-Dunlop, and N. R. Heckenberg, "Measurement of the optical force and trapping range of a single-beam gradient optical trap for micron-sized latex spheres," *J. Mod. Optics*, vol. 41, no. 3, pp. 595–601, 1994.

[20] K. Svoboda and S. M. Block, "Biological applications of optical forces," *Annu. Rev. Biophys. Biomol. Struct.*, vol. 23, pp. 247–285, 1994.

[21] E. Fallman and O. Axner, "Design for fully-steerable dual-trap optical tweezers," *Appl. Optics*, vol. 36, no. 10, pp. 2107–2113, 1997.

[22] W. H. Wright and G. J. Sonek, "Radiation trapping forces on microspheres with optical tweezers," *Appl. Phys. Lett.*, vol. 63, no. 6, pp. 715–717, 1993.

[23] A. Ashkin, "Forces of a single-beam gradient laser trap on a dielectric sphere in the ray optics regime," in *Methods in Cell Biology* (M. P. Sheetz, ed.), vol. 55 (*Laser Tweezers in Cell Biology*), ch. 1, pp. 1–27, Academic Press, 1998.

[24] Automation Creations, Inc., Christiansburg, VA., *MatWeb: Materials Property Data*, 2004. www.matweb.com.

[25] R. W. Fox and A. T. McDonald, *Introduction to Fluid Mechanics*. Wiley, 4th ed., 1992.

[26] F. Gittes and C. H. Schmidt, "Signals and noise in micromechanical measurements," in *Methods in Cell Biology* (M. P. Sheetz, ed.), vol. 55 (*Laser Tweezers in Cell Biology*), ch. 8, pp. 129–156, Academic Press, 1998.

[27] M. Sitti, "Micro- and nano-scale robotics," in *Proceedings of the 2004 American Control Conference*, (Boston, MA), pp. 1–8, American Automatic Control Council, June 2004.

[28] D. Kleppner and R. J. Kolenkow, *An Introduction to Mechanics*. McGraw-Hill, 1973.

[29] S. R. Kuo and M. P. Sheetz, "Force of single kinesin molecules measured with optical tweezers," *Science*, vol. 260, pp. 232–234, 1993.

[30] K. Visscher and S. M. Block, "Versatile optical traps with feedback control," in *Methods in Enzymology* (R. B. Vallee, ed.), vol. 298 (*Molecular Motors and the Cytoskeleton: Part B*), ch. 38, pp. 460–489, Academic Press, 1998.

[31] S. Grego, E. Arimondo, and C. Frediani, "Optical tweezers based on near infrared diode laser," *Journal of Biomedical Optics*, vol. 2, pp. 332–339, July 1997.

[32] T. Wohland, A. Rosin, and E. H. K. Stelzer, "Theoretical determination of the influence of the polarization on forces exerted by optical tweezers," *Optik*, vol. 102, no. 4, pp. 181–190, 1996.

[33] A. Ranaweera, K. J. Astrom, and B. Bamieh, "Lateral mean exit time of a spherical particle trapped in an optical tweezer," in *Proceedings of the 43nd IEEE Conference on Decision and Control*, (Paradise Island, Bahamas), December 2004. To appear.

[34] K. J. Astrom, *Introduction to Stochastic Control Theory*. Academic Press, 1970.

[35] A. T. Bharucha-Reid, *Elements of the Theory of Markov Processes and Their Applications*. McGraw-Hill, 1960.

[36] A. Ranaweera and B. Bamieh, "Calibration of the characteristic frequency of an optical tweezer using an adaptive normalized gradient approach," in *Proceedings of the 2003 American Control Conference*, (Denver, CO), pp. 3738–3743, IEEE, June 2003.

[37] D. R. Cox and H. D. Miller, *The Theory of Stochastic Processes*. John Wiley, 1965.

[38] S. M. Block, "Construction of optical tweezers," in *Cells: A Laboratory Manual* (D. L. Spector, R. D. Goldman, and L. A. Leinwand, eds.), vol. 3, Cold Spring Harbor Laboratory Press, 1997. Section 11, www.stanford.edu/group/blocklab/cshl-chap.html.

[39] J. R. Geraghty, 2000. Technical Sales Representative, Carl Zeiss, Inc., Thornwood, NY.

[40] M. E. J. Friese, A. G. Truscott, H. Rubinsztein-Dunlop, and N. R. Heckenberg, "Three-dimensional imaging with optical tweezers," *Appl. Optics*, vol. 38, no. 31, pp. 6597–6603, 1999.

[41] J.-C. Meiners and S. Quake, "Direct measurement of hydrodynamic cross correlation between two particles in an external potential," *Phys. Rev. Lett.*, vol. 82, no. 10, pp. 2211–2214, 1999.

[42] Polytec PI, Germany, *Physik Instrumente*, 1998. Catalog, www.physikinstrumente.com.

[43] Isomet Corporation, Springfield, VA., *Acousto-Optic Deflectors*, June 2001. Technical documentation.

[44] NEOS Technologies, Inc., Melbourne, FL., *Acousto-Optic Modulator*, July 2001. Acceptance Test Procedure, Model Number N45035-3-6.5DEG-1.06, Document Number 52A11839.

[45] M. W. Allersma, F. Gittes, M. J. DeCasto, R. J. Stewart, and C. F. Schmidt, "Two-dimensional tracking of ncd motility by back focal plane interferometry," *Biophys. J.*, vol. 74, pp. 1074–1085, 1998.

[46] P. Swift, "Design and setup of optical tweezers," Master's thesis, Department of Mechanical and Environmental Engineering, University of California, Santa Barbara, June 2000. Unpublished.

[47] UDT Sensors, Inc., Hawthorne, CA, *Photodiode Characteristics*. www.udt.com.

[48] Burr-Brown Corp., Tucson, AZ., *Designing Photodiode Amplifier circuits with OPA128*, 1994. Application Bulletin.

[49] National Instruments, Austin, TX., *Measurement and Automation*, 2003. Catalog.

[50] Newport Corporation, Irvine, CA., *Optics and Mechanics*, 1999-2000. Catalog.

[51] M. D. Greenberg, *Advanced Engineering Mathematics*. Prentice Hall, 2nd ed., 1998.

[52] L. Ljung, *System Identification*. Prentice Hall PTR, 2nd ed., 1999.

[53] D. G. Alciatore and M. B. Histand, *Introduction to Mechatronics and Measurement Systems*. WCB/McGraw-Hill, 2nd ed., 2003.

[54] T. Soderstrom and P. Stoica, *System Identification*. Prentice Hall, 1989.

[55] K. J. Astrom and B. Wittenmark, *Computer-Controlled Systems*. Prentice Hall, 3rd ed., 1997.

[56] G. F. Franklin, J. D. Powell, and A. Emami-Naeini, *Feedback Control of Dynamic Systems*. Addison-Wesley, 3rd ed., 1994.

[57] K. J. Astrom, "Maximum likelihood and prediction error methods," *Automatica*, vol. 16, pp. 551–574, 1980.

[58] A. Ranaweera and B. Bamieh, "Calibration of the characteristic frequency of an optical tweezer using a recursive least squares approach," in *Proceedings of the 2004 American Control Conference*, (Boston, MA), pp. 1836–1841, American Automatic Control Council, June 2004.

[59] P. A. Ioannou and J. Sun, *Robust Adaptive Control*. Prentice Hall PTR, 1996.

[60] S. Skogestad and I. Postlethwaite, *Multivariable Feedback Control*. Wiley, 1996.

[61] J. E. Molloy, J. E. Burns, J. Kendrick-Jones, R. T. Tregear, and D. C. S. White, "Movement and force produced by a single myosin head," *Nature*, vol. 378, pp. 209–212, 1995.

[62] K. J. Astrom, "Control systems design lecture notes for ME 155A." Department of Mechanical and Environmental Engineering, University of California, Santa Barbara. Unpublished, 2002.

[63] A. Ranaweera, A. R. Teel, and B. Bamieh, "Nonlinear stabilization of a spherical particle trapped in an optical tweezer," in *Proceedings of the 42nd IEEE Conference on Decision and Control*, (Maui, HI), pp. 3431–3436., December 2003.

[64] E. Liu, Y. Chitour, and E. Sontag, "On finite gain stabilizability of linear systems subject to input saturation," *SIAM Journal on Control and Optimization*, vol. 34, pp. 1190–1219, July 1996.

[65] H. K. Khalil, *Nonlinear Systems*. Prentice Hall, 2nd ed., 1996.

[66] Z. Gao and R. R. Rhinehart, "Theory vs. practice: The challenges from industry," in *Proceedings of the 2004 American Control Conference*, (Boston, MA), pp. 1341–1349, American Automatic Control Council, June 2004.

[67] L. P. Ghislain, N. A. Switz, and W. W. Webb, "Measurement of small forces using an optical trap," *Methods Cell Bio.*, vol. 65, no. 9, pp. 2762–2767, 1994.

[68] S. R. Quake, H. Babcock, and S. Chu, "The dynamics of partially extended single molecules of DNA," *Nature*, vol. 388, pp. 151–154, 1997.

[69] Y. Arai, R. Yasuda, K. ichirou Akashi, Y. Harada, H. Miyata, K. K. Jr, and H. Itoh, "Tying a molecular knot with optical tweezers," *Nature*, vol. 399, pp. 446–448, 1999.

[70] UDT Sensors, Inc., Hawthorne, CA., *Segmented Photodiodes (SPOT Series): Position Sensing Detectors*, 2000. www.udt.com.

[71] UDT Sensors, Inc., Hawthorne, CA, *Segmented Photodiodes (SPOT Series): Position Sensing Detectors (PSD)*. www.udt.com.

[72] P. Horowitz and W. Hill, *The Art of Electronics*. Cambridge, 2nd ed., 1999.

[73] J. E. Molloy, "Optical chopsticks: digital synthesis of multiple optical traps," in *Methods in Cell Biology* (M. P. Sheetz, ed.), vol. 55 (*Laser Tweezers in Cell Biology*), ch. 12, pp. 205–216, Academic Press, 1998.

[74] G. V. Shivashankar and A. Libchaber, "Single DNA molecule grafting and manipulation using a combined atomic force microscope and an optical tweezer," *Appl. Phys. Lett.*, vol. 71, no. 25, pp. 3727–3729, 1997.

[75] A. L. Stout and W. W. Webb, "Optical force microscope," in *Methods in Cell Biology* (M. P. Sheetz, ed.), vol. 55 (*Laser Tweezers in Cell Biology*), ch. 6, pp. 99–116, Academic Press, 1998.

[76] K. Morishima, F. Arai, T. Fukuda, H. Matsuura, and K. Yoshikawa, "Screening of single escherichia coli in a microchannel system by electric field and laser tweezers," *Analytica Chimica Acta*, vol. 365, pp. 273–278, 1998.

[77] D. J. Odde and M. J. Renn, "Laser-guided direct writing of living cells," *Biotechnology and Bioengineering*, vol. 67, pp. 312–318, 2000.

[78] K. Schutze and A. Clement-Sengewald, "Catch and move–cut or fuse," *Nature*, vol. 368, pp. 667–669, 1994.

[79] K. O. Greulich and S. Monajembashi, "Laser microbeams and optical tweezers: how they work and why they work," *SPIE*, vol. 2628, pp. 116–127, 1996.

[80] M. W. Berns, Y. Tadir, H. Liang, and B. Tromberg, "Laser scissors and tweezers," in *Methods in Cell Biology* (M. P. Sheetz, ed.), vol. 55 (*Laser Tweezers in Cell Biology*), ch. 5, pp. 71–98, Academic Press, 1998.

[81] R. C. Gauthier, "Optical trapping: a tool to assist optical machining," *Optics Laser Tech.*, vol. 29, no. 7, pp. 389–399, 1997.

[82] E. Hecht, *Optics*. Addison-Wesley, 3rd ed., 1998.